

Quantum field thermal machines

M. Gluza*,¹ J. Sabino*,^{2,3,4} N. H. Y. Ng*,¹ G. Vitagliano*,⁵ M. Pezzutto,³
Y. Omar,^{2,3} I. Mazets,^{4,6} M. Huber,^{5,*} J. Schmiedmayer,^{4,†} and J. Eisert^{1,‡}

¹*Dahlem Center for Complex Quantum Systems, Freie Universität Berlin, 14195 Berlin, Germany*

²*Instituto Superior Técnico, Universidade de Lisboa, Portugal*

³*Instituto de Telecomunicações, Physics of Information and Quantum Technologies Group, Lisbon, Portugal*

⁴*Vienna Center for Quantum Science and Technology, Atominsitut, TU Wien, 1020 Vienna, Austria*

⁵*Institute for Quantum Optics and Quantum Information (IQOQI), Austrian Academy of Sciences, 1090 Vienna, Austria*

⁶*Wolfgang Pauli Institute c/o Fakultät für Mathematik,
Universität Wien, Oskar-Morgenstern-Platz 1, 1090 Vienna, Austria*

(Dated: June 6, 2022)

Recent years have enjoyed an overwhelming interest in quantum thermodynamics, a field of research aimed at understanding thermodynamic tasks performed in the quantum regime. Further progress, however, seems to be obstructed by the lack of experimental implementations of thermal machines in which quantum effects play a decisive role. In this work, we introduce a blueprint of quantum field machines, which - once experimentally realized - would fill this gap. We provide a detailed proposal how to realize a quantum machine in one-dimensional ultra-cold atomic gases using a set of modular operations giving rise to a piston that can be coupled sequentially to thermal baths with the innovation that a quantum field takes up the role of the working fluid. We study the operational primitives numerically in the Tomonaga-Luttinger liquid framework proposing how to model the compression of the system during strokes of a piston and the coupling to a bath giving rise to a valve controlling phononic heat flow. By composing the numerically modeled operational primitives we design complete quantum thermodynamic cycles that are shown to enable cooling and hence giving rise to a quantum field refrigerator. The active cooling achieved in this way can operate in regimes where existing cooling methods become ineffective. We describe the consequences of operating the machine at the quantum level and give an outlook of how this work serves as a road map to explore open questions in quantum information, quantum thermodynamics and the study of non-Markovian quantum dynamics.

I. INTRODUCTION

As elevated and set in stone as the basic principles of thermodynamics may appear, there is a development emerging that could not have been anticipated when this theory was being conceived. Indeed, the basic laws were formulated in an effort to understand the functioning of macroscopic machines that can be described by classical physics. However, due to advances in quantum technologies the question that currently begs for an answer is what happens if we consider heat engines for which *quantum laws* and *effects* are expected to play an important role. Indeed, there has been a significantly increased recent interest in exploring *thermodynamic notions* in the *quantum regime* [1–7].

One of the most notable insights that has been achieved in this context is, on the one hand, the increased role of knowledge and control giving rise to potentially superior performance of quantum machines. On the other hand, inevitable fluctuations of energy pose novel conceptual challenges in defining thermodynamic quantities at the quantum scale. Additionally, in the quantum regime thermal and quantum correlations may range over substantial portions of the elements of the machine, possibly influencing its dynamics. These fundamental questions have stimulated interesting experimental developments, e.g. fully controlling a quantum system such

as a trapped ion [8, 9] or an electronic circuit [10] to engineer behavior reminiscent of thermal machines.

There is a caveat, however, constituting a serious road block in this avenue of research. It arguably turns out to be excessively difficult to experimentally realize *genuinely quantum* thermal machines: This would be a physical system for which (i) quantum mechanics is *required* to derive an appropriate effective physical model describing its dynamics, (ii) its operation includes certain regularities (e.g., cycles in a broader sense) going against the natural direction of entropy increase and (iii) it is *infeasible* to control its every single degree of freedom. As a longer term goal, such a machine would be one in which quantum mechanics is necessary to grasp their very functioning, and which cannot be entirely captured by classical mechanics. At the present stage, such a machine has yet to be devised, but could potentially play a similar role for the development of quantum thermodynamics as the steam engine did for the classical theory of thermodynamics. This state of affairs seems a grave omission in particular in the light of the observation that it was the study of the performance of machines that led to the development of classical thermodynamics in the first place.

In this work, we propose a blueprint for *quantum field machines* (QFMs) first conceived in Ref. [11] that would, once experimentally realized, qualify as being genuine quantum thermal machines in this sense. One of the central challenges here is a trade-off between a sufficient size of the machine to meaningfully allow for thermodynamic considerations – after all, one has to make reference to thermal baths – and sufficient control of the dynamics. Only if suitable levels of control can

* marcus.huber@univie.ac.at

† schmiedmayerjoerg@me.com

‡ jense@zedat.fu-berlin.de

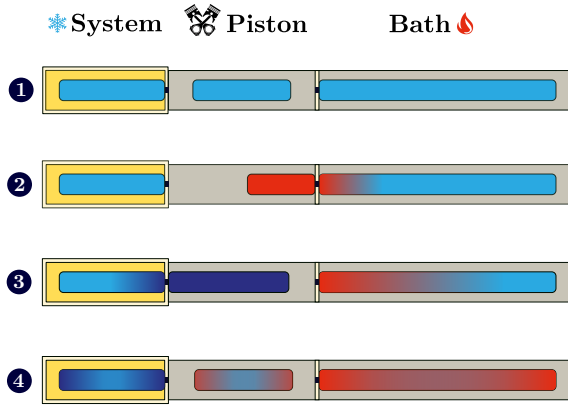


FIG. 1. **Quantum field refrigerator:** Similar to canonical ideas employed in ordinary thermal machines, we consider for a quantum many-body system a cycle consisting of a small set of control operations on quantum working fluids, concatenated in order to cool down a part of the machine (referred here as the “system”). This is achieved through a protocol consisting of four steps: 1) Initialization of the system, the piston and the bath at equal temperatures. 2) Compression of the piston and coupling to the bath which receives energy, and decoupling after the heat transfer. 3) Decompression of the piston, therefore decreasing its energy, then coupling to the system thus enabling heat transfer from the system to the piston. 4) Decoupling of the piston from the system and compression to initial size. Through steps 1-4), we expect to achieve a decrease in the system’s energy, while the energy of the piston and bath should increase. This increase in energy happens in such a way that the piston and bath can be reused for multiple cycles before they saturate. As we will discuss, all these operations can be implemented experimentally in an ultra-cold atomic gas by shaping light fields that control the atoms.

be reached, one can hope to transcend features of classical statistical mechanics and reveal genuine quantum behavior of machines. Furthermore, elucidating quantum thermodynamic behavior will only be important if the envisioned machines actually manage to perform a task that would otherwise be impossible to achieve by other means. The QFMs that we propose here intend to address all of the aforementioned challenges posed when building genuine quantum machines:

(i) They are genuine complex quantum many-body systems admitting a description in terms of emergent degrees of freedom captured by an effective quantum field theory. In this work we will focus on a QFM tuned to the Tomonaga-Luttinger liquid [12, 13] regime which is efficiently simulable numerically, but the QFM can also enter a strongly correlated regime where this may no longer be possible.

(ii) They offer potential new tools for quantum liquids and gases, e.g., by providing a new additional stage of cooling which does not involve diluting the system and can be applied after the use of other techniques.

(iii) The available degree of controllability makes it possible to exploit strong correlations and coherences for probing quantum effects but this is achieved by understanding and steering the physics of the system and not controlling its individual degrees of freedom.

This anticipated device derives from ultra-cold atoms that in a tuneable fashion realize the full range from non-interacting to strongly correlated quantum fields [11], as can be implemented on an Atom Chip [14–16]. The feature that renders it a machine is the presence of programmable time-dependent potentials allowing to manipulate the quantum fields. Such time-dependent potentials have been implemented in a 1D experiment on an Atom Chip by means of a *digital micro-mirror device (DMD)* [17]. That is to say, the DMD devices take the role of “control knobs” of the machine. At the same time this machine, involving phononic quantum fields [12, 13, 18, 19], will operate at finite temperatures, thus all these features come together when considering a quantum field thermal machine.

We shall start our investigation by laying out in Section II the concept of a quantum field machine and describing its building blocks. In Section III we give a detailed introduction on how to implement a quantum field machine using one-dimensional quasi-condensates manipulated on an Atom Chip with optical fields. In Section IV, we present a numerical study of each primitive operation described in the introduction and in Section V show how to compose them together to make a quantum field refrigerator. Finally, in Section VI we discuss the obtained results and complete the roadmap towards building a quantum field thermal machine by highlighting some possible future directions of research that will have to be explored.

II. THE QUANTUM FIELD MACHINE (QFM)

Thermodynamics is a versatile framework allowing to describe a large variety of machines. Any of these ordinary thermal machines can be explored in the quantum regime if one considers operating it under conditions where quantum effects prominently play a role. This is the pathway we take in this work, by considering the working fluid to be a *Bose-Einstein condensate (BEC)* and in the one-dimensional regime more precisely we will consider quasi-condensates [20]. In order to investigate the influence of quantum effects on the machine, it is a necessity to consider an appropriate quantum model that describes the system. At the same time, to grasp the potential of quantum machines it is crucial to be able to view the quantum evolution as implementing certain abstract operations, i.e. well defined thermodynamic transformations, general enough to be independent on whether quantum effects are significantly involved or not.

A quantum thermal machine can be constructed by choosing few suitable building blocks and applying some operations on them in a cyclic fashion, forming a thermodynamic cycle. For instance, as illustrated in Fig. 1 it is instructive to consider a quantum thermal machine consisting of three elements, of which two are thermal baths, while the third is a piston shuttling between them. With these ingredients it is, e.g., possible to run a *heat engine*, by allowing heat to be transferred from the hot bath to the cold one, while work can be extracted from the piston. If quantum fluctuations play a significant role, the process of work extraction would have to be investigated in

a framework compatible with quantum mechanics. In case that the individual objects are small and they feature large energy fluctuations, the systems may exhibit complex out-of-equilibrium dynamics during the operation of the cycle. As another example, if instead work is performed from outside, one can construct a *heat pump* and use the piston to extract heat from one part of the machine and dispose it into another part: in other words, the machine can operate as a *refrigerator*.

In order to implement such quantum field machines, we identify a set of general operations which we call *quantum thermodynamic primitives* (QTPs). These are the basic ingredients of our thermodynamic protocols, which can be concatenated in a modular fashion to build up the complex range of potential applications that our machine might have. A variety of operations can be conceived, corresponding to different tasks such as activating or deactivating heat flow, injecting or extracting heat from a system, performing or extracting work from a system, moving or shuttling a system around, or suitably adding catalyzing systems.

In what follows, we will put particular emphasis on providing details about the functioning of a quantum field refrigerator as illustrated in Fig. 1. For this, we will stress the significance of two building blocks giving rise to two crucial QTPs. The first is a valve and allows to control the *energy flow* between elements of the machine. The second is the piston which allows to *control thermodynamic parameters* during a stroke when the volume changes and hence via the equation of state also the pressure or temperature will change. Below we briefly outline these two QTPs which are central to our blueprint.

Coupling and decoupling two quasi-condensates: A valve

As depicted in Fig. 1, one of the essential ingredients for operating a QFM is coupling its elements. This will be in general realized by allowing excitations to tunnel through a barrier which allows to control the flow of energy between two parts of a QFM, like in a valve. When considering a valve of a QFM, we expect to find some differences compared to a similar type of operations in an ordinary thermal machine.

(i) Specifically, in classical physics, merging of systems with identical density would be largely featureless. Two quasi-condensates, in sharp contrast, if initially uncorrelated, will have a random phase, and coupling will lead to a random phase gradient which results in creation of additional *excitations*. In a quantum system, if we do not align the relative phases of the quantum fields, merging adds excitations and entropy. Such quantum *phase diffusion* [21–24] can, however, be countered by enabling yet another quantum effect which is coherent tunneling through a barrier which leads to *phase-locking* in an out-of-equilibrium situation [25–30].

(ii) Conversely, splitting the elements of the QFM – once they have established phase coherence – may introduce quantum noise [31, 32] related to the *dynamical Casimir effect* [33, 34]. The production of excitations in this process may in a finite and well-controlled system add an amount of energy which is not negligible.

(iii) The individual elements are systems which feature *correlations* extending over sizable lengths and time unlike in ordinary thermal machines. Notably, even at thermal equilibrium a single quasi-condensate has a finite thermal coherence length $\lambda_T \neq 0$ [26, 35] which would not be true if one were to simply set the reduced Planck constant to zero $\hbar \rightarrow 0$ entirely disregarding quantum effects.

(iv) Whenever the elements of the QFM have coherent dynamics then *recurrences* of evolution may occur as observed in Ref. [25]. This, among others, is one of the signatures of the presence of *non-Markovian effects* in the system. Due to this, concatenation of cycles in the QFM may depend on the precise timing.

Notice that these effects are particularly relevant because we cannot consider the thermodynamic limit for the elements of the QFM as in state-of-the-art experiments it is not possible to create thermodynamically large ultra-cold gases. E.g., while the amount of energy injected in a local operation should be intensive, its effect may be substantial for the experiment.

Compressing and decompressing: A piston

The defining feature of a piston is that its size can be changed which, via the equation of state [18], leads to a change of internal energy. Additionally, if the piston gets smaller it may get separated from the other parts so it may need to be shuttled in order to be coupled to other elements of the QFM. The main role of the piston is that even if all the parts of the QFM are in thermal equilibrium, we can introduce temperature differences by performing work upon the piston. This then in combination with the valve QTP allows to enable heat flow in the desired direction. Again, if the physics of the piston involves quantum effects one can expect certain differences to ordinary thermal machines. For example,

(i) while the energy is changing due to compression or decompression the piston may go out of thermal equilibrium, e.g., due to *squeezing* of internal modes [34, 36]. If this quantum feature will influence thermodynamic transformations involved in the operation of a thermal machine, then such a machine will have richer physics compared to a standard one. Hence understanding the performance limits of such potential machines must be done by a thermodynamic framework including this non-classical effect.

(ii) Internal dynamics in our system occurs within time-scales comparable to timings of individual steps of the cycles considered. In contrast for classical thermal machines the internal and cycle time-scales are perfectly separated.

(iii) The piston can be modeled by considering a moving boundary which is also closely related to the *dynamical Casimir effect* [34].

III. IMPLEMENTING QUANTUM FIELD MACHINES IN 1D BOSE-EINSTEIN QUASI-CONDENSATES

This section discusses the experimental techniques necessary for realizing a QFM. We propose an implementation based on ultra-cold one-dimensional gases, with Sec. III A describing the microscopic model and the related *effective Hamiltonian* defining the energy of phononic fields. Sec. III B describes concisely role of the DMD in *engineering* the desired QTPs, closely matching the experimental state-of-the-art [17]. Finally, the capability of being able to *see* the implemented effects should not be understated and we discuss various diagnostic methods in Sec. III C.

A. Effective quantum field theory description of 1D cold atoms

Cold atomic gases at low temperature and with a fixed average number of atoms can be considered one dimensional if the trap anisotropies are sufficiently large to constrain the dynamics in two (transversal) dimensions such that the dynamics effectively takes place in the remaining (longitudinal) direction [13, 20]. In this regime, the system is well described by the Lieb-Liniger Hamiltonian, which reads

$$\hat{H}_{LL} = \int dz \hat{\Psi}^\dagger \left[\frac{-\hbar^2}{2m} \partial_z^2 + V(z, t) - \mu + \frac{g}{2} \hat{\Psi}^\dagger \hat{\Psi} \right] \hat{\Psi}. \quad (1)$$

Here $\hat{\Psi}(z)$ is the atomic annihilation operator at spatial position z which satisfies bosonic exchange statistics $[\hat{\Psi}(z), \hat{\Psi}^\dagger(z')] = \delta(z - z')$. The atomic mass is denoted by m and \hbar is the reduced Planck constant. The external potential $V(z, t)$ is responsible for longitudinal trapping of the gas but will be also discussed as a means of implementing the control necessary for operating the QFM. The quartic interaction has strength $g/2$ which is proportional to the scattering length of the atoms and also depends on other characteristics of the trap, specific of the experimental implementation [25]. Finally, μ is the chemical potential that can be fixed, e.g., by constraining the average number of atoms N_{atoms} .

For systems that are not homogeneous, the above Hamiltonian cannot be solved exactly due to the quartic term. However, it is well known that a quadratic approximation in the spirit of the Tomonaga-Luttinger liquid theory captures the low-energy excitations [12, 18] and works very well for certain time-scales [36]. Let us denote the variational ground state atomic density of \hat{H}_{LL} evaluated over the set of coherent states by $\rho_0(z)$. It has the interpretation of the mean-density profile that can be measured by in-situ density absorption (see Eq. (A1), appendix A) and can be calculated theoretically by solving the Gross-Pitaevskii (GP) equation, i.e., the evolution equation derived from Eq. (1) [17, 26]. The effective model is obtained by considering the the polar decomposition of the field operators $\hat{\Psi}(z) = (\rho_0(z)\hat{\mathbb{I}} + \delta\hat{\rho}(z))^{1/2} \exp(i\hat{\varphi}(z))$ and expanding the Hamiltonian up to second order in the density $\delta\hat{\rho}(z)$ and phase $\hat{\varphi}(z)$ fluctuation operators, which are again bosonic $[\delta\hat{\rho}(z), \hat{\varphi}(z')] = i\delta(z - z')\hat{\mathbb{I}}$. They represent

phononic excitations of a cold atomic gas and their energy is given by the following *effective Hamiltonian*

$$\hat{H}_{TLL}[\rho_0] = \int dz \left[\frac{\hbar^2 \rho_0(z)}{2m} (\partial_z \hat{\varphi}(z))^2 + \frac{g}{2} \delta\hat{\rho}(z)^2 \right], \quad (2)$$

which can be decoupled in normal phononic modes. An important feature of this model is that wave-packets travel with a speed of sound related to the mean density $c = \sqrt{g\rho_0/m}$.

The model in Eq. (2) provides a good effective description for experiments performed on an isolated quasi-condensate. However, in our simulations the QFM couples its initially. Then, one has to additionally model what happens with the phase zero-modes in the systems. A phase zero-mode is an eigenmode with the interpretation of total momentum frame of the excitations and for an isolated system phase fluctuations of this eigenmode do not cost energy [21–24]. When two thermal systems, each with their own zero-mode, will become coupled the two zero-modes will hybridize to form the joint zero-mode and one mode that costs energy.

However, this energy cost can be large if the original phase zero-modes were non-trivially populated, since the phase difference of two independent systems is fully random.

Nevertheless, in the physical system, the energy should change continuously because of additional terms coming from the expansion of Eq. (1) which would dynamically induce *phase-locking* between the two condensates being merged together, i.e., the hybridization of zero-modes is a dynamical process. Via the large coupling expansion of this term, or arguing phenomenologically, an effective model can be derived that reads

$$\hat{H}[\rho_0] = \hat{H}_{TLL}[\rho_0] + 2\pi\hbar \int dz J(z) \rho_0(z) \hat{\varphi}(z)^2, \quad (3)$$

where the additional term regularizes the zero-modes. Here, we make the modeling simplification $J \equiv \text{const}$, effectively gapping-out the phase zero-modes at all times. The presence of this additional term can be interpreted as the quasi-condensates being merged having been already phase-locked prior to the merging. The phase-locking term effectively induces squeezing of the modes which can be analytically seen in the homogeneous case and we used a small value $J = 20$ mHz in all plots throughout the main text, see App. C 3 for further details regarding a more generic $J(z)$.

B. Controlling the 1D quantum field simulator using a DMD

It is worth noting that the same Hamiltonian also describes many other systems from the class of *Tomonaga-Luttinger liquids (TLLs)* such as electrons in nano-wires or spin-1/2 chains [37, 38]. This observation hence serves as a basis for performing *quantum simulations* [39–42] on the level of phonons using cold-atomic one-dimensional gases. The external potential $V(z, t)$ influences the form of the GP profile ρ_0 and thus allows for experimentally controlling the TLL Hamiltonian. If the control is time-dependent then the GP profile will become time-dependent $\rho_0(z, t)$ and hence the speed of sound of prop-

agating wave-packets may become space- and time-dependent too.

To achieve the QTPs described in Section II, the longitudinal trapping potential $V(z, t)$ has to be precisely manipulated. In Ref. [17] it was demonstrated that nearly arbitrary control of the longitudinal potential can be obtained by adding dipole potentials created by light fields shaped by a DMD. By digitally tuning the mirrors of the DMD, the beam of light can be structured, allowing one to obtain various potential landscapes $V(z, t)$ which are tunable along of the quasi-condensate and in time.

It is also worth stressing that optimal control techniques can be used for the realization of the valve and piston QTPs in the experiment in a way maximizing the stability of the system. In Refs. [43, 44], it has been demonstrated that, for the case of compressing the gas in a harmonic trap, it is possible to find short-cuts to adiabaticity. In this case, a single control parameter has been suitably optimized which was the frequency of the longitudinal harmonic trapping potential. This has allowed to expand the gas without introducing longitudinal breathing of the mean density which hints that optimal control should also be important for implementing a piston using a DMD potential. Similarly, for the valve it is important to switch on the coupling between the two systems, without introducing stray excitations into the system which again can be optimized by appropriately tailored time-dependent potentials using the DMD.

C. Space and time resolved monitoring of thermodynamic transformations

In order to monitor the operation of a quantum thermal machine, observables that reveal local and global information about the state system are needed. Of special interest are for example atomic density, spectrum and occupation of excitations, or their coherences and correlations. These physical observables allow to monitor and understand the details of thermodynamic processes, such as heat or entropy flow during the operations and the global thermodynamic properties for the qualitative analysis.

There are several well established methods to probe 1D quantum systems. These range from in-situ measurements of density fluctuations [45–49] to measuring phase fluctuations in time of flight by either “density ripples” [50, 51] or interference [52, 53]. Information is extracted by analyzing the full distribution functions [54] or correlation functions [35, 55–57]. It will be crucial to use these measurement methods to extract information about local properties of the system. This will be important in order to detect the action of local control when implementing the envisioned quantum thermodynamic operations and resolving the thermodynamic transformations occurring in the elements of the QFM. Of specific interest, when probing the quantum thermodynamic processes, will be the (local) occupations of excitations in the quantum fields. Here in our example, these are phonons. We first observe that the energy of the phonons in the system is defined as the expectation value of the TLL Hamilton operator (2). This in-

volves an integral over the length of the condensate. If one considers the complete integral, then we would obtain the total energy. However, access to the local phase-phase fluctuations

$$C^{\phi\phi}(z, z') = \langle \hat{\phi}(z) \hat{\phi}(z') \rangle \quad (4)$$

and the second moments of local density fluctuations

$$C^{\rho\rho}(z, z') = \langle \delta \hat{\rho}(z) \delta \hat{\rho}(z') \rangle \quad (5)$$

directly implies the knowledge of the local energy density, which is given by

$$\frac{dE(z)}{dz} = \frac{\hbar^2 \rho_0(z)}{2m} \partial_{z_1} \partial_{z_2} C^{\phi\phi} \Big|_{z_1=z_2=z} + \frac{g}{2} C^{\rho\rho}(z, z) . \quad (6)$$

Note that the cross-correlations between the phase and density degrees of freedom

$$C^{\phi\rho}(z, z') = \langle \hat{\phi}(z) \delta \hat{\rho}(z') \rangle \quad (7)$$

do not contribute to energy and vanish in thermal equilibrium though may be non-zero during out-of-equilibrium dynamics. At this point, two comments may be in order.

(i) Firstly, the expression for local energy (6) needs to be regularized due to divergences at the point $z_1 = z_2$, and this is accounted for by considering a UV cut-off in the corresponding field theory, in order for the energy in the system to be finite.

(ii) Secondly, the experiment with its finite imaging resolution and effects of “smearing” in time of flight [53] can only measure a coarse-grained expectation value of the fields averaged over a finite length scale σ_{res} . This resolution provides a natural UV cut-off, since that higher momentum modes cannot be detected.

The gradient of the phase operator $\hat{v} = \partial_z \hat{\phi}$ can be interpreted as velocity of wave-packets traveling on top of the condensate. Thus, the first term in the Hamiltonian (2) can be thought of as the energy content related to the speed of wave-packets, while the other term to how much distortion of the local density they carry. It is important to note that both contributions must be measured in order to have the complete information about the energy in the system.

As we have mentioned, it is possible to measure experimentally by observing the quasi-condensate *in situ* transversely (from the side) which is available in the Atom Chip platform by means of density absorption [45–49]. In Appendix A, we discuss how measurements of the local density fluctuations of the atomic gas gives access to direct measurement of the GP profile ρ_0 and the second moments of the density fluctuations $\Gamma^{\rho\rho}$ which include certain correlations of phonons. Additionally, in Appendix A we describe a proposal of a tomographic reconstruction method similar to Ref. [36] that is based on out-of-equilibrium data of $\Gamma^{\rho\rho}(t)$ at different times t and allows to recover $\Gamma^{\phi\phi}$. This then provides access to the second moments of phase fluctuations and hence the energy in the phase sector can be extracted. Hence, based on direct observation of the system from the side together with a tomographic analysis we can measure quantities revealing information about the

energy distribution and dynamics in the system.

Alternatively, one can envision interfering the system under study with a local oscillator (a large 3D BEC) [58] or with an identical system [53, 55, 56] to extract the local phase correlations $C^{\phi\phi}$. From them one can tomographically reconstruct the correlations of density fluctuations $C^{\rho\rho}$ [36]. Together these two covariance matrices reveal information about the energy distribution and dynamics in the system.

If one can assume thermal equilibrium, then it is possible to extract the occupation numbers of phonons even from $C^{\phi\phi}$ alone [56]. Global parameters like temperature can then be obtained also by “density ripples” [50, 51]. The temperature is typically extracted by means of an appropriate fit to the correlations of the fluctuations of the atoms after a time-of-flight expansion.

It is important to understand which thermodynamic transformations are going to have a substantial effect so that they can be clearly detected in the experiment. The precision for measuring the (changes) in temperature or energy in the system will depend on reliability of the state preparation and the statistical sample size. We anticipate that changes of temperature or energy by about 10% should be large enough to obtain conclusive experimental results [25] ($> 5\sigma$) where one can be confident about, e.g., observing heat flow or cooling in a given system.

IV. NUMERICAL STUDIES OF QUANTUM THERMODYNAMIC PRIMITIVES (QTPS)

As sketched in Fig. 1 above, using the piston and the valve as fundamental building blocks of a QFM allows to construct a refrigeration cycle. In this section, we will present results on the numerical modeling of the individual QTPs involved. We start by presenting a simple coupling mechanism between two quasi-condensates, and then shift the focus to the functioning of the piston.

Each QTP that we propose is modeled by a TLL Hamiltonian described in the previous section, which allows us to simulate the dynamics of phonons and to calculate the corresponding energy changes in the system. As the model is a quadratic Hamiltonian, our simulations are done within the Gaussian framework and are computationally efficient even when evaluating sophisticated measures from quantum information theory such as the relative entropy. Our focus will be to introduce and define the primitives, while emphasizing their physical meaning and generality. The latter is crucial as it should be clear that all QTPs that we present are independent of our modeling – qualitatively they represent robust quantum thermodynamic operations, and the quantitative details should depend only on the specific implementation. That is to say we will describe generically what the primitives do, and propose a specific way of realizing them by engineering a system that is well described by a TLL and has the necessary control capabilities.

The TLL model allows us to derive core predictions in a framework that is known to accurately capture in the low energy limit the specific cold atoms experiments we have

in mind. Thus, in our simulations we use parameters that fit state-of-the-art experiments of 1D quasi-condensates performed on the Atom Chip platform. More generally, our proposal can be embodied within the broader framework of thermodynamics with multi-mode Gaussian states, with Gaussian operations modeling the action of external system control. Details on the numerical methods employed for simulating the individual primitives can be found in Appendices B and C.

A. Coupling and decoupling two quasi-condensates: A valve

Adjusting the DMD external potential will make it possible to split the gas in two parts or merge at will [59]. Let us begin by studying the merging process in terms of energy and correlation changes. It is clear that such a process is an essential element for creating a thermodynamic cycle giving rise to a valve which controls when the heat flows between systems.

Here, we consider a simple model, where two quasi-condensates can be coupled via a small buffer region. Specifically, we will consider a bipartite system A and B , each part being initially thermal and essentially homogeneous, the two parts being separated by a buffer region of negligible size $\ell \sim \xi_h$ so that phonons cannot tunnel.

The TLL Hamiltonian in Eq. (2) is essentially specified by the GP profile, which we choose with a shape like it is shown in Fig. 2 (a). In the field theory framework the description of the system via this effective Hamiltonian is completed by specifying the Neumann boundary conditions (NBCs) at the edges. The density profiles that we choose have precisely the scope of smoothening further the boundary conditions in our implementation via a discretized lattice model.

Denoting by ρ_0^A and ρ_0^B the GP profiles of the systems A and B , respectively, the initial Hamiltonian of the two independent systems reads

$$\hat{H}_{A|B} = \hat{H}[\rho_0^A] + \hat{H}[\rho_0^B], \quad (8)$$

where the tiny separation at the interface is modeled by the Hamiltonian $\hat{H}_{A|B}$ having in total 4 NBCs, two at the edges and two in the middle.

Next, we define the joint system to have a GP profile

$$\rho_0^{AB}(z) = \begin{cases} \rho_0^A(z) & z \in A, \\ \rho_0^B(z) & z \in B, \end{cases} \quad (9)$$

implementing the “gluing” of the profiles. Thus, in our minimal modeling approach, we neglect the precise spatial details of experimental control necessary to switch from two independent systems to the coupled case as we assume that they are close and only a microscopic change is necessary for removing the small buffer region. With that, we can take the final Hamiltonian of the merged systems to be of the form

$$\hat{H}_{AB} = \hat{H}[\rho_0^{AB}] = \hat{H}_{A|B} + \hat{H}_{\text{int}}, \quad (10)$$

which now has only 2 NBCs and there is effectively an interaction \hat{H}_{int} between the two parts A and B . Due to this

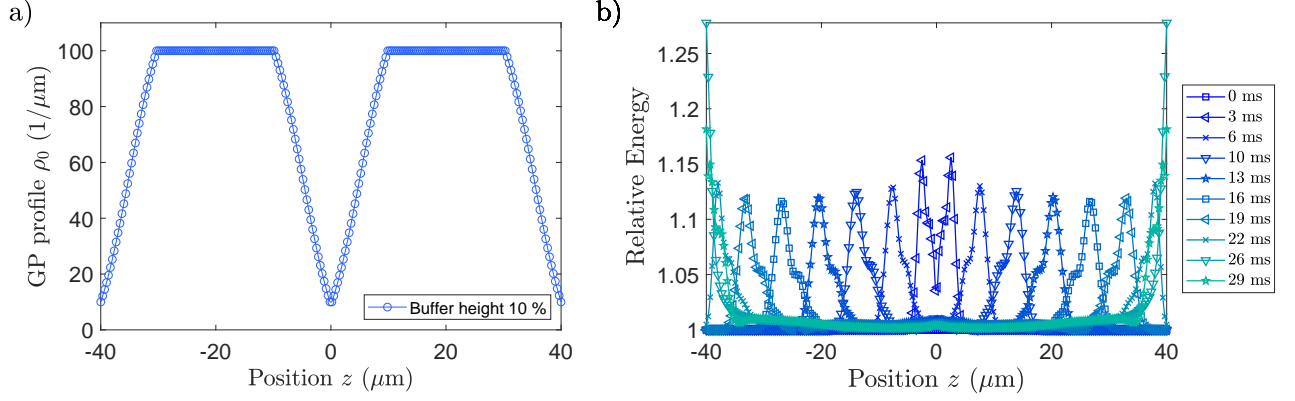


FIG. 2. **Operating a valve between two identical and independent thermal quasi-condensates.** (a): *GP profiles.* We consider two quasi-condensates which are homogeneous in the bulk but their density falls off towards zero at their edges. At position $z = 0$ there is initially the boundary condition that in our effective model at a single point implements the separation between the two systems. As the systems become coupled the energy can tunnel between the two systems through this point. Throughout on line plots of real-space quantities bullets indicate the discretization lattice used in the simulation while the continuous lines are merely a guide to the eye. (b): *Dynamics of energy density.* We plot $dE(z)/dz$ defined in Eq. (6) for different times during the coupling of two quasi-condensates. Initially, the energy density in each quasi-condensate is uniform, and we use that value to normalize the plotted values. During the coupling, localized energy is injected at the interface of the two systems and travels ballistically away in form of wave-packets, which increase the energy density by $\approx 15\%$.

coupling, the thermal state of \hat{H}_{AB} , in contrast with that of $\hat{H}_{A|B}$, contains correlations between A and B .

Note that when the two systems are separated there are in total four boundary conditions and after they become coupled in the middle only two remain. We will handle this boundary condition issue by interpolating linearly between the uncoupled Hamiltonian with 4 NBCs and the coupled Hamiltonian with 2 NBCs.

Thus, we model the time-resolved dynamics of the merging protocol by the time-dependent Hamiltonian

$$\hat{H}_{A-B}(t) = \left(1 - \frac{t}{t_{\text{merge}}}\right) \hat{H}_{A|B} + \frac{t}{t_{\text{merge}}} \hat{H}_{AB}, \quad (11)$$

within $t \in [0, t_{\text{merge}}]$. Here we model the situation that by means of the external potential control the density profiles become smoothly interpolated. As described in Appendix C, we perform a lattice discretization to compute the physical quantities of interest and in this framework mixing boundary conditions is well-defined.

In order to study the dynamics of merging two quasi-condensates, we consider initial conditions that are natural for experiments with cold atoms where evaporative cooling yields systems with a thermal distribution of phonons. For the simulation we consider at initial time $t = 0$ two independent thermal TLLs, with temperatures $T_A = T_B = 50$ nK. Thermal states are defined with respect to a given Hamiltonian \hat{H} (coupled, decoupled etc.) and the density matrix reads

$$\hat{\gamma}_T[\hat{H}] := \mathcal{Z}^{-1} e^{-\hat{H}/(k_B T)}, \quad (12)$$

where $\mathcal{Z} = \text{Tr}(e^{-\hat{H}/(k_B T)})$ is the partition function and k_B is the Boltzmann constant. We choose to use GP profiles with peak density $\rho_0^A = \rho_0^B = 100$ atoms/ μm and

smoothly falling off towards a smaller value at the edges, see Fig. 2 (a) [60].

In Fig. 2 (b) we show the numerical results for a linear ramp with merging time $t_{\text{merge}} = 40$ ms. This is a rather long time-scale and it was chosen here to show that the excitations can start returning towards the interface if the merging takes a long time. Initially, the energy is distributed homogeneously in each system so we present the energy distribution relative to that value. This relative measure, which will be employed throughout, allows to disregard the cut-off dependent shift coming from zero-point fluctuations. In fact, our effective Hamiltonian is not normal-ordered but rather regularized by the finite healing length $\xi_h = \hbar/(mc)$ in the system (note that the cutoff Δz in our numerical simulations is higher than the healing length). We find that, as anticipated, merging two systems via tunnel coupling induces excitations in form of two counter-propagating wave-packets traveling with the respective speed of sound, which in typical experiments on the Atom Chip platform is about $c \approx 2 \mu\text{m/ms}$ [25]. The simulation predicts that the presence of the wave-packets increases the local energy by quite a sizable amount of about $\sim 15\%$. This may cause system dynamics to deviate from the TLL model. Nevertheless, the higher-order terms that could become relevant in the experiment should have only the effect of dispersing the wave-packets. According to simulations the amount of injected excitations is higher if the systems are coupled at peak density, see appendix C 2. The reason for this is that in the lattice approximation we are adding an off-diagonal coupling between the two respective edges of A and B of scaling with time and density $\sim (1 - t/t_{\text{merge}})\rho_0(z = 0)$ and so the merging is “softer” if the density value is lowered at the interface. More on physical terms, it is more stable to couple two extremely sensitive systems harboring gapless excitations through two diluted regions than at the peak den-

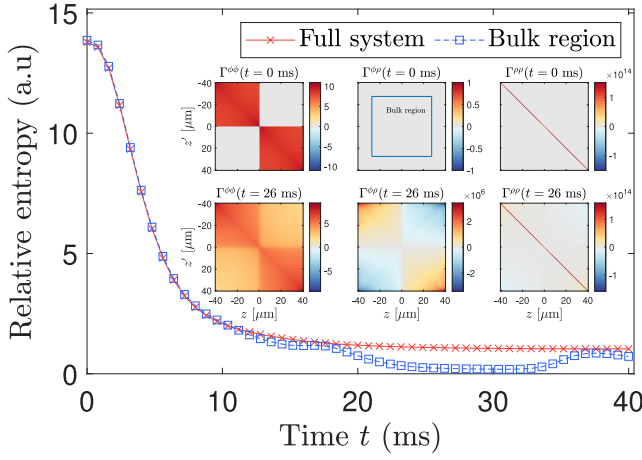


FIG. 3. **Correlations before and after merging.** The initial covariance matrix $\Gamma(t = 0 \text{ ms})$ (inset top) is characterized by phase fluctuations $\Gamma^{\phi\phi} = 2C^{\phi\phi}$ ranging only over the individual systems, no cross correlations between phase and density operators $\Gamma^{\phi\rho} \equiv 0$ and density fluctuations $\Gamma^{\rho\rho} = 2C^{\rho\rho}$ being essentially diagonal. When the heat excitations reach the edges, the covariance matrix $\Gamma(t = 26 \text{ ms})$ (inset bottom) restricted to the bulk region of the system agrees with the thermal covariance matrix of the joint Hamiltonian: phase fluctuations $\Gamma^{\phi\phi}$ become uniform over the joint system and in the bulk of the system cross correlations vanish $\Gamma^{\phi\rho} \approx 0$ while density fluctuations $\Gamma^{\rho\rho}$ are diagonal. Quantitatively, we plot the relative entropy of the time-dependent covariance matrix with respect to that of the thermal state of the coupled Hamiltonian at $T = 50 \text{ nK}$ and observe that it decreases rapidly over around 10 ms. Due to the presence of the heat wave-packets the relative entropy for the full system (red crosses) does not converge to zero over time, while for the covariance matrix restricted to the bulk region (blue squares) essentially vanishes at around $t = 26 \text{ ms}$ and then increases again.

sity, where the insertion of any excitation would have a larger impact. It is instructive to analyze the correlations of the coupled state during the merging. As shown in Fig. 3, we find that initially there are no correlations between A and B and hence we see that two independent thermal TLLs are not thermal with respect to the joint Hamiltonian. During the merging the systems become coupled and the established correlations drive the state towards being close to the joint thermal state, see appendix C 2 for more details. Interestingly, after the first traversal time, i.e., when a local excitation at the merging interface has traveled to the edges, the joint system is close to being thermal in the bulk as shown in the inset of Fig. 3.

The observation that the merged system become jointly thermal can further be quantified by evaluating the *relative entropy* given for any two states by $S(\hat{\gamma}||\hat{\sigma}) = \text{Tr}(\hat{\gamma}(\log \hat{\gamma} - \log \hat{\sigma}))$. Evaluating this functional with respect to a thermal state yields

$$S(\hat{\gamma}||\hat{\gamma}_T[\hat{H}]) := (F(\hat{\gamma}) - F(\hat{\gamma}_T[\hat{H}])) / (k_B T) \geq 0, \quad (13)$$

where $F(\hat{\sigma}) = \text{Tr}(\hat{H}\hat{\sigma}) - k_B T S(\hat{\sigma})$ is the *free energy* of the state relative to the ambient temperature T and the Hamiltonian \hat{H} and $S(\hat{\sigma}) = -\text{Tr}(\hat{\sigma} \log \hat{\sigma})$ is the von Neumann en-

tropy. Notably, the relative entropy is zero if and only if the two covariance matrices are the same (see also Appendix B for further details). This makes it into a viable measure of the deviation from thermal equilibrium and in particular $S(\hat{\gamma}||\hat{\sigma}) = 0$ implies the equality of all correlation functions for both states. Finally, this measure can be computed also for *reduced* density matrices which then captures how systems are similar *locally*.

In order to check if the merging QTP is intensive we calculate the relative entropy of the state evolving during merging with respect to the thermal state of the coupled Hamiltonian at $T = 50 \text{ nK}$. Initially, the relative entropy decreases rapidly, reflecting the ongoing thermalization around the interface of the two systems, where the correlations are being established. For the whole system the relative entropy does not reach zero and levels off to a constant value within about 10 ms. This is due to the wave-packets being always present in the system, hence the impossibility for the entire system to be in thermal equilibrium. If we consider the reduced covariance matrix describing only the bulk middle region, we see that around 20 ms the relative entropy drops essentially to zero. This means that once the excitations leave the window of observation, the system left behind agrees in that region with the (joint) thermal state. Finally, for longer times the wave-packets come back to the bulk and allow for detecting an out-of-equilibrium component of the state.

Thus, in this subsection, we have observed that two tunnel-coupled TLLs can reach an effectively joint thermal state at specific evolution times. This feature should remain true even under perturbations to the model as temperature for locally merged systems should be intensive. Additionally we observed that as long as the coupling ramp is not infinitely slow, there will be always some energy injected at the interface in form of localized wave-packets. Again, perturbations are not expected to change the character of low-energy excitations so the spectrum should remain approximately linear and a local change of the Hamiltonian should generically create a localized surplus of energy propagating through the system with the speed of sound. We conclude that the merging protocol is a thermodynamically sound QTP.

In the case presented here we showed an example where there was no net heat flow between two systems. If we would have instead coupled two systems with different temperatures, then we should observe a heat transport between condensates, which ceases only when the temperatures equalize. The next section shows how to enable heat flow between two systems, by performing work from outside, thereby creating an effective temperature difference.

B. Compressing and decompressing: A piston

In this subsection, we will see how external control by the DMD, which compresses or expands the gas, enables a region to function as a working medium that can be compressed and decompressed akin to a classical gas. The external forces from the DMD will effectively perform work on the quasi-condensate, increasing or decreasing its energy depending on

the change in volume. This is similar to thermodynamics of an ideal gas with the difference that we are considering a quantum many-body system. Operations for this QTP have been successfully implemented with use of shortcuts to adiabaticity (see Ref. [43] where the extension of the GP profile has been stably modified).

Here, we propose a model to describe what happens to phonons when the confining trap (space occupied by the gas) changes. Let the length of a uniform system change continuously over time in the sense that a homogeneous GP profile ρ_0 with support of length L changes to $\rho_0(t)$ with corresponding length $L(t)$. The operation is assumed to preserve the atom number $N_{\text{atoms}} = \rho_0 L$ so that

$$\rho_0(t) = \rho_0 \frac{L(0)}{L(t)}. \quad (14)$$

This time-dependent GP profile assumes that the change in volume is slow so that a homogeneous system remains homogeneous at all times. Under this assumption, the TLL Hamiltonian (2) parametrized by a time-dependent GP profile $\rho_0(t)$

$$\hat{H}(t) = \hat{H}[\rho_0(t)] \quad (15)$$

is the time-dependent Hamiltonian describing the phonons during the size change. Using Eq. (15), the integration in (2) should range over the time-dependent length of the system $L(t)$. Again, in the lattice approximation this can be straightforwardly implemented by discretizing the Hamiltonian at each time considered and identifying the respective cells at consecutive times as they change only infinitesimally. It is also possible to consider formulating this procedure using a fixed representation of momentum mode and time-dependent eigenmode wave-functions, see Ref. [34].

In the homogeneous case by a change of the integration variable we can write the time-dependent Hamiltonian as

$$\hat{H}(t) = \int_0^{L(0)} dz \left[\frac{\hbar^2 \lambda^2(t) \rho_0}{2m} (\partial_z \hat{\varphi})^2 + \frac{g}{2} \lambda(t) \delta \hat{\nu}^2 \right], \quad (16)$$

where we have also defined a rescaled density fluctuation field $\delta \hat{\nu} = \delta \hat{\rho} / \lambda(t)$ in order to preserve the canonical commutation relations. I.e., this way we have $[\delta \hat{\nu}(z), \hat{\varphi}(z')] = i\delta(z - z')$. Here we made the integration limits explicit and changed the frame so that the length of the system is effectively constant but the Hamiltonian density becomes time-dependent due to the dimensionless length ratio

$$\lambda(t) = \frac{L(0)}{L(t)}. \quad (17)$$

We observe that if the system stays homogeneous then for all times t the time-dependent Hamiltonians (16) share the same momentum-eigenmodes, which will become squeezed. We hence should expect that compressing will have an effect of introducing *squeezing* of phase and density quadratures in the system, see Ref. [34] for a related discussion and the appendix C 5 for an extended discussion, including the numerical implementation of the compression model.

With this model we can simulate the functioning of a piston: In Fig. 4 we show the results of a simulation of a single stroke. We consider a piston in the same initial state as either of the two systems shown in Fig. 2 before merging. We then compress the system uniformly by half in $t_{\text{comp}} = 15$ ms and then decompress it back to the initial size in the same time. We find that the energy stays essentially homogeneously distributed during the piston stroke, see Fig. 4 (a). It is moreover possible to check whether the piston stays thermal during the compression and decompression. The necessary condition is fulfilled as the energy density is uniform at all times and changes in relation to volume. As shown in Fig. 4 (b) the total energy increases and comes back the initial value during the stroke of the piston. However, a more refined check involving the relative entropy shows that the system is not at thermal equilibrium at all times. At a sequence of times during the evolution we evaluated the relative entropy of the time-dependent state to thermal states with temperatures taken from a certain range. The temperature of the thermal state with the lowest relative entropy gives the effective fit for the temperature. It is clear that if the time-dependent state remains thermal at all times, then there will be a temperature for which the relative entropy vanishes. If the piston is away from thermal equilibrium then the value will be strictly positive. We find that as the energy increases the relative entropy measure shows that the state is pushed away from thermal equilibrium, and comes back to it only when the stroke is finished. This effect can be naturally explained by the presence of squeezing in the system, but we focus here on the thermodynamic aspects of the model and refer to Ref. [34] for a discussion of the dynamical Casimir effect related to the system considered.

We now can use the compression QTP in order to enable heat flow between two systems. In Fig. 5 we show the steps (1-2) of the Otto cycle that were sketched in Fig. 1, i.e. we compress the piston, couple it to the bath and after decoupling decompress it back to its initial state. As before, the piston and bath are both thermal initially and have the same overall shape of the GP profile with the only difference that the bath is three times larger than the piston. As was shown above, coupling two systems with the same temperatures does not lead to heat flow. In order to enable it, we compress the piston using the compression QTP. After the piston is compressed its energy is higher and so is its effective temperature. The bath remains static so there is a temperature difference between the piston and bath which means heat will flow from the piston to the bath. Using the coupling QTP we effectively open the valve between the piston and bath so that heat can flow. After this is completed we split the two systems closing the heat flow valve and decompress the piston to its initial length. This means that the piston has performed a stroke but in its compressed state has released heat to the bath. After it comes back to its initial length it should therefore be colder than it was initially. In Fig. 5 (a) we show the results of this protocol plotting the full spatio-temporal dynamics of the energy density and in Fig. 5 (b) we show that the compressed piston couples to the bath with effectively squeezed modes and the two systems are not at thermal equilibrium while the valve is open. Nevertheless energy in the piston decreases as heat flows into the bath

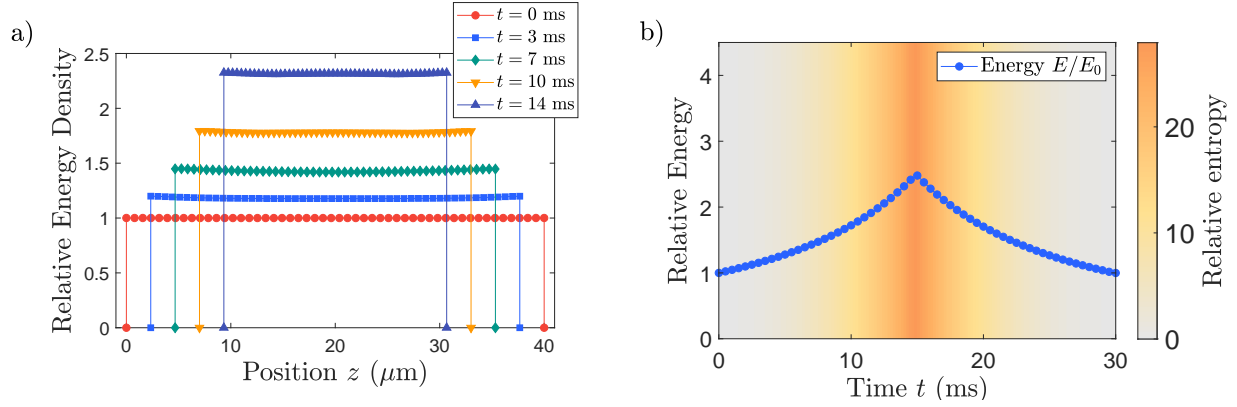


FIG. 4. **Single stroke of a piston.** A piston initially thermal and homogeneous and of length $40\text{ }\mu\text{m}$ is compressed to half size within 15 ms and then expanded back to the initial length in the same time. (a): *Energy density during compression.* The piston keeps a homogeneous energy density which, however, increases while the length is reduced. (b): *(Non-)equilibrium properties of piston during the stroke.* We plot over time the global energy relative to its initial value (blue dots) and the relative entropy to the closest thermal state as a color gradient during the whole stroke (i.e., compression and decompression). We find that the compression increases the total energy of the system due to increasing pressure of the phononic gas. Furthermore, the piston goes out of equilibrium, as the relative entropy to the closest thermal state also increases during compression. The reverse happens when the piston decompresses. In particular, the piston is again fully thermal at the initial energy and temperature at the end.

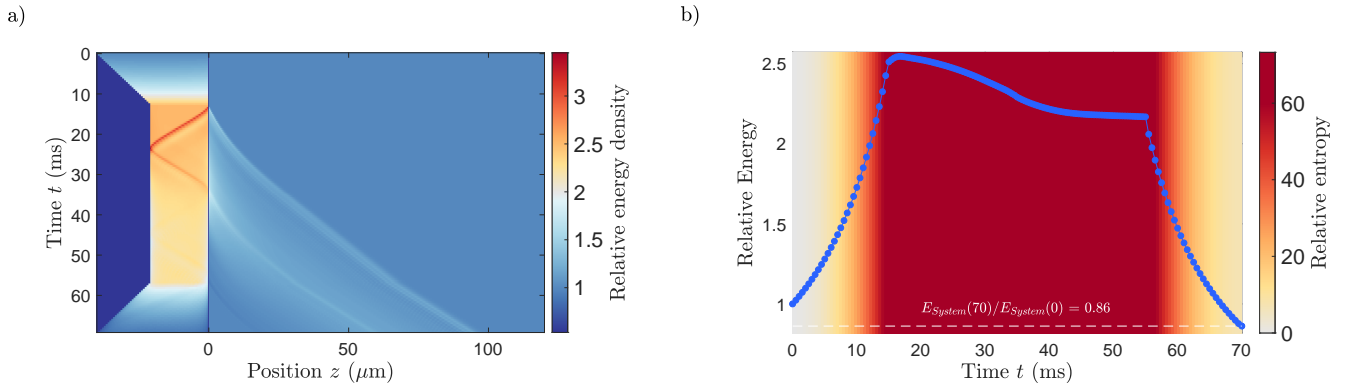


FIG. 5. **Heat flow between the piston and bath.** We consider the piston on the left, after being compressed to half of the size and the bath on the right in its initial state. We couple the piston to the bath at $t = 15$ ms and start decoupling them right after the coupling is completed. (a): *Energy density over time.* We plot the energy as a color gradient in a space-time grid. The coupling between the two parts introduces the propagation of wave-packets at the speed of sound, which is higher in the piston, due to the higher density resulting from compression. (b): *Energy dynamics in non-equilibrium.* We plot the ratio of average energy versus initial energy in the piston over time. We observe that it first increases strongly, while decreasing to a value that is less than 1, just before the piston starts coupling with our system of interest. This is what will allow us to cool the system with a full Otto cycle. We also plot the relative entropy to the best fit thermal state as a color gradient in the background and observe that during coupling the system goes strongly out of equilibrium, while returning to be close to equilibrium at the end.

which is also seen in Fig. 5 (a) in form of a light-color stripe entering the bath. Finally, we find that the total energy in the piston decreases to a lower value than initially and thus we conclude that the piston has been overall cooled down at the end of this protocol. Interestingly, at the end of the protocol the decompression undoes the squeezing of the modes and the piston essentially comes back to thermal equilibrium signified by a low relative entropy to a thermal state.

Summarizing, it should be stressed that we have performed work on the piston which allowed us to enable the heat flow and by composing the compression QTP with the open valve QTP we deposited some of the piston's energy into the bath.

This composition of QTPs is a crucial step that can be simulated numerically already now but will be an important milestone in the experiments, signifying the transition from studying the physics of the cold atomic gas to performing with the system sophisticated thermodynamical tasks at will.

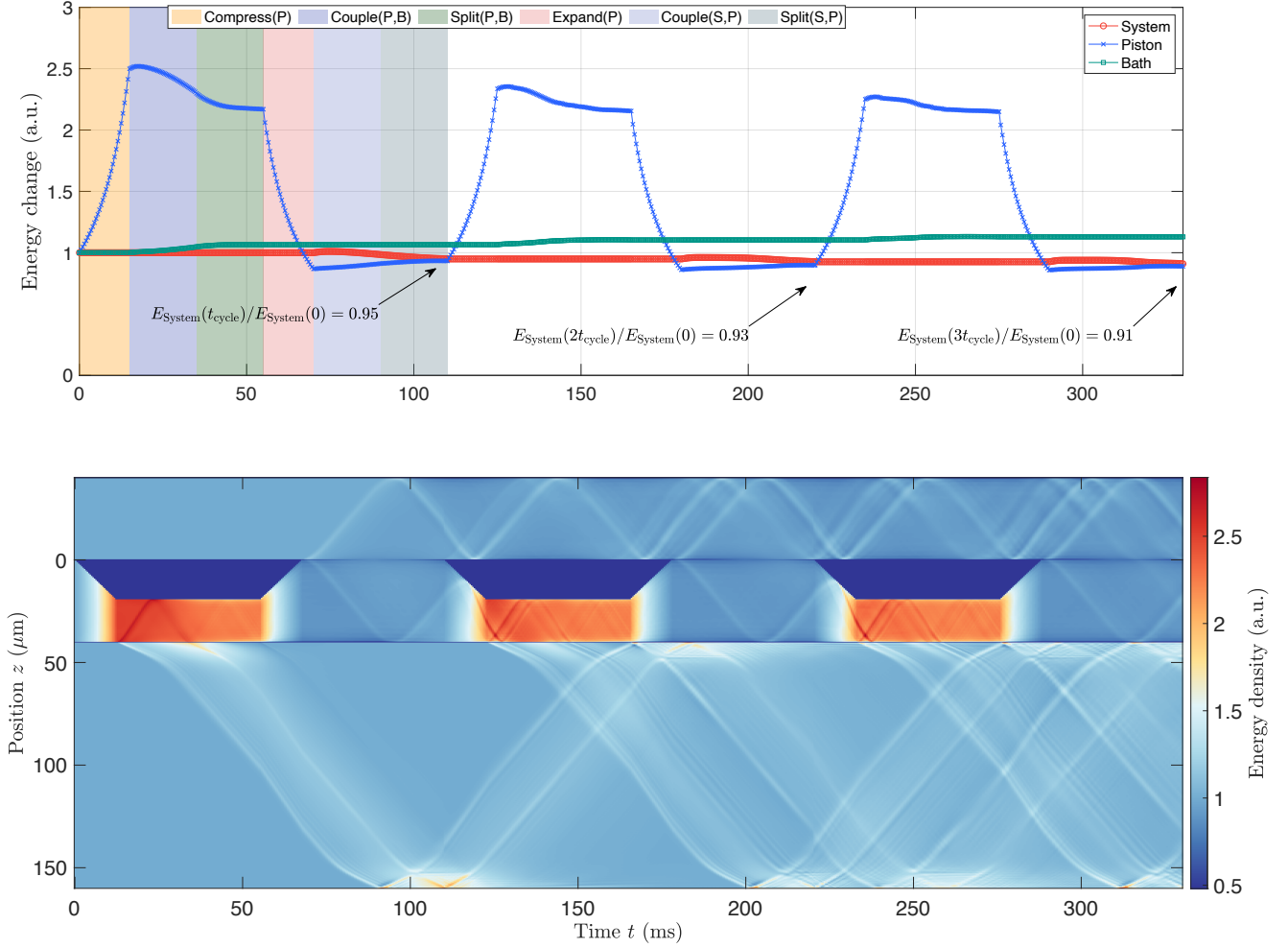


FIG. 6. **Top: Quantum field refrigerator.** The QFM is initialized in thermal equilibrium and equal density, i.e. the system, piston and bath only differ in length which is 40 , 40 , 120 μm respectively. We then run the Otto cycle by compressing the piston (15 ms), depositing heat in the bath (40 ms) and then expanding the piston again (15 ms). The cooling cycle then begins at around 70ms by coupling the initially thermal system to the piston cooled down by the initialization. The two systems exchange energy by the same physical mechanism as in the initialization. It is less desirable to expand the system, anticipating that in order to cool it down, one should in practice avoid modifying its Hamiltonian, e.g. compressing, whenever possible. After the final splitting of the system and piston we find that the system has cooled down, while the quantum field refrigerator extracted $\sim 5\%$ of the system's initial energy. This drop in energy is large enough to be detected by existing experimental read-out methods with finite measurement precision. In this plot, one observes that further cycles continue to contribute to cooling of the system, but only in very small amounts (as shown, the first and second additional cycles brought the cooling $\sim 3\%$ and 2% further, respectively). The currently used parameters are probably non-optimal, and we anticipate improvements of the refrigeration efficiency via optimal quantum control. This, however, will depend on the modeling of other details in the quantum simulation of this cycle. **Bottom: Time and space resolved energy dynamics during the operation of the TLL Otto quantum field thermal machine.** From the top we show the system, piston (which changes in size) and bath. Whenever a valve QTP is operated, wavepackets are injected and multiple reflections in each system can occur. The principal wavepacket in the bath is timed to arrive at the interface to the piston at around 160 ms when the valve is closing and the energy of the piston is not further increased. The overall amount of energy in the bath increases, which is due to the multiple wave-packets present there at late times. It is noteworthy that, depending on scheduling, the larger among two coupled systems can take up two wave-packets. Hence, considering the piston to be substantially larger than the system could allow to remove all excitations from the system. This is also the reason why the bath takes up most of the wavepackets.

V. COMPOSING QUANTUM THERMODYNAMIC PRIMITIVES TO BUILD A QUANTUM FIELD REFRIGERATOR

In this section, we demonstrate how to compose the discussed primitives to perform a useful protocol, namely cool-

ing. The challenge one faces experimentally is that all methods of cooling always reach a limit once the temperature is small enough. The last method to lose efficiency for ultra-cold gases is evaporative cooling. In Ref. [61] this method was explored in the 1d regime and at extremely cold tem-

peratures and it was demonstrated that it has a large range of applicability but also its limits were quantitatively mapped out. The conclusion was that the coldest possible temperature depends on the density $T \propto N_{\text{atoms}}/L$. Thus, temperature can be lowered by extending the evaporative cooling however this then dilutes the system. For the state-of-the-art data reached with this method [25] for $N_{\text{atoms}} \approx 5000$ atoms confined in about $L = 50 \mu\text{m}$ the estimated temperature is about $T \approx 50 \text{ nK}$ [36]. By simulating the quantum field refrigeration machine depicted in Fig. 1 at this density and temperature, we find a cooling cycle where the system has lower temperature than initially, highlighting the usefulness of such a new active cooling protocol. The cycle works as follows:

(1) The machine is initialized with a system, a piston and a bath, each at thermal equilibrium.

(2) The first non-trivial thermodynamic transformation is the compression of the piston with a subsequent interaction with the bath. The work inserted to compress the piston enables heat flow as shown above in Fig. 5.

(3) After splitting the piston from the bath, the piston is expanded back to its initial length. This aims to cool it down and when it subsequently interacts with the system it should take up some heat from it.

(4) Finally, the piston and system are split again and the cycle can be repeated.

In Fig. 6, we depict the energy changes of these three pieces of the QFM over the duration of the Otto refrigeration protocol obtained from a numerical simulation. It can be seen that the piston first increases its energy due to compression ($t_{\text{comp}} = 15 \text{ ms}$) and then lowers it during interaction with the bath and successive expansion ($t_{\text{merge}} + t_{\text{comp}} = 35 \text{ ms}$). Finally, the piston increases again its energy when interacting with the system and then resizing to its original length ($t_{\text{merge}} + t_{\text{comp}} = 35 \text{ ms}$). Overall, at the end of the first cycle ($t_{\text{cycle}} = 110 \text{ ms}$), the piston has slightly decreased in energy, while system and bath have consistently decreased and increased their energy, respectively. By performing three Otto cycles, we obtained cooling of about 10%.

We considered very conservative choices for the parameters and several relaxations can be explored in the experiment in order to obtain a higher cooling ratio. (i) As shown in the bottom panel of Fig. 6 the piston was compressed to half its length which ultimately limits the capacity of the machine to cool down. Performing more work and compressing it more would allow for further cooling. (ii) Modifying the buffer height and various other aspects of our QFM model higher cooling ratios are possible as shown in appendix C 6. These among others could be refreshed baths, coupling at higher density etc. which are features that depend on the particular implementation and hence cannot be completely anticipated theoretically ahead of performing the experiment. (iii) Let us remark that for the sake of simplicity and also for analogy with the usual thermodynamic Otto engine, the piston is the only component that changes size during the protocol. However, one can think of more general scenarios in which the bath is expanded while piston is compressed, and afterwards, the system is compressed while piston is expanded – after-all in the experiment it will be our goal to cool down the quasi-

condensate more than is possible with existing methods and an unconventional quantum thermal machine with various elements changing their size would be helpful for that. Summarizing, there are a lot of turning knobs one can consider when devising a QFM. It is clear that once QTPs are realized, their conceptual clarity will be advantageous in order to appropriately compose them to achieve maximal possible cooling in the experiment.

VI. DISCUSSIONS AND FURTHER SCOPE

While further developing the framework of QFMs and during the upcoming efforts to realize a QFM experimentally, numerous questions relating to the fundamental physics of the system and technological implementation beyond the scope of this initial manuscript will have to be further investigated. Our discussions below highlight several aspects which could invite expertise from fields such as engineering and quantum control of out-of-equilibrium quantum many-body systems to become particularly useful.

Thinking ahead, the program of devising a QFM presented in this work is also expected to stimulate a range of further theoretical investigations in the field of quantum thermodynamics [1–7]. These will range from (experimentally inspired) studies of the role of information in quantum thermodynamics to prospects for further development of the theory of quantum thermodynamics from a quantum information perspective.

A. Experimental realization of a QFM

In the present manuscript, we have deliberately focused on a simple and straightforward way of implementing a QFM in the form of a one-dimensional bosonic quantum gas which can be described with a Gaussian effective model, i.e., the TLL. Having said that, there are many interesting directions that can be explored in order to extend our proposal.

1. Non-Gaussian QFMs

We have left it open to what extent higher-order, non-Gaussian contributions will play a substantial role in the operation of the QFM in the experiment. One example where these could potentially matter is when running the QFM with a long cycle time. This is because of de-phasing or damping effects which are not present in the TLL model can occur in real experiments already around 50 ms [25, 36]. We currently take into account effects of dephasing only whenever two systems are split, which is consistent with this timescale since merge-split protocol considered in our simulation is 40 ms. A key aspect of future investigations will be to comprehensively explore *weak* non-Gaussian effects arising from such effects. We expect many-body de-phasing to primarily have the effect of thermalizing the bath, but otherwise not obstructing the heat flow which occurs faster than the on-set of any de-phasing observed so far. Nevertheless, a detailed study will provide more substantial insights into this important aspect.

The second interesting case is to notice that during the splitting and recombination, the mean density at the interface is low and there the TLL description might break down. This may lead higher-order interactions to become substantial and induce scattering of phonons around the interface. In the experimental implementation, one can extract higher-order correlations and study non-Gaussian correlations [35]. If present, they can be studied by numerical field theoretic calculations [62] or compared with predictions based on fundamental relations in quantum thermodynamics [63].

Finally, the existing Atom Chip platform allows to controllably add *sine-Gordon* interactions [30, 35] and hence also non-Gaussian QFMs can be explored experimentally. The sine-Gordon model is paradigmatic for our understanding of quantum field theory [64–67] thanks to its rich physics, e.g., excitations of finite mass and non-trivial topological properties. The experimental implementation [35] following the quantum simulation proposal from Ref. [68] was realized using two longitudinally tunnel-coupled one-dimensional quasi-condensates. In this case the system should be described by *relative* degrees of freedom, the relative phase $\hat{\varphi}_{\text{rel}}(z)$ and density $\delta\hat{\varrho}_{\text{rel}}(z)$ fluctuation fields [69]. Using interferometric measurements [25, 26, 35, 52, 53] correlation functions of the relative phase can be measured which allowed to substantiate that the physical system was correctly described by the effective sine-Gordon Hamiltonian for two adjacent quasi-condensates

$$\hat{H}_{\text{sG}} = \int dz \left[\frac{\hbar^2 \rho_0(z)}{4m} (\partial_z \hat{\varphi}_{\text{rel}}(z))^2 + g \delta\hat{\varrho}_{\text{rel}}(z)^2 \right] - \int dz 2\hbar J \rho_0 \cos(\hat{\varphi}_{\text{rel}}(z)). \quad (18)$$

The first term represents the quadratic TLL-type Hamiltonian now capturing the energy of the *relative* phonon modes. The second term represents a non-quadratic interaction between these modes. Tuning of the tunnel coupling J is possible experimentally which would allow to build QFMs in various interaction regimes, ranging from a system of non-interacting modes to a strongly correlated quantum system with topological excitations. See Ref. [11] for further details in the context of thermal machines and Ref. [35] for a detailed experimental study of the many-body aspects of the model.

Summarizing, the two coupled one-dimensional quasi-condensates will allow us to build and study strongly correlated QFMs, where the degree of correlations (that is, the degree of higher-order correlation functions that are relevant) can be experimentally tuned. It is known that the time evolution of interacting local quantum systems is computationally hard (technically speaking, it is BQP-complete in worst-case complexity), and in practice computationally demanding for classical computers for physically relevant problems. This applies as well to the equilibrium processes involved in the operation of the QFM. While numerical studies may prove inefficient, the properties of these strongly correlated QFMs can be probed experimentally in detail by measurements of (higher-order) correlation functions [35, 70].

2. Matter-wave interferometry of parallel QFMs

An intriguing idea is to run machines in parallel. This opens up the possibility to compare the operation of two identical machines by direct observation of *matter-wave interferometry* [71, 72]. On the Atom Chip it is possible to conceive of two machines positioned side by side, parallel to each other (Fig. 1 would then be the side-view of *two* machines) and they would be identical in the sense of having the same initial state preparations and subsequent control operations implementing QTPs making up the Otto cycle. This can be done using well-established protocols of manipulating the gas using a longitudinal double-well and interference has been observed in this case in various situations [25, 32, 35, 52, 70, 73, 74]. Interferometry by its nature looks at *relative* fluctuations and hence disregards classical disturbances in the operation which are identical for both systems and directly measures *quantum* fluctuations. Their appearance should be studied interferometrically for various initial states of the two systems including

- (i) two independent systems created by cooling two cold atomic clouds separately. This provides the base case to be compared to when studying more interesting initial states.
- (ii) Two systems that are de-phased in a pre-thermalized state [32]. In this case the temperature of relative degrees of freedom has been found not to be fully determined by the cooling process but rather to be related to the tunnel coupling J in Eq. (18) present during state preparation.

(iii) Two systems with (nearly) identical phonon modes with strongly suppressed quantum noise in the relative degrees of freedom. Such states have been achieved experimentally [56, 75] and can be further improved by optimal control of the splitting process [76].

Each of these approaches would prepare machines that would have distinct initial conditions and an experimental study would allow to gain insights on how these influence the operation of the QFMs. Observing features where cases (ii-iii) would differ from the simple case of independent machines (i) would then most likely require a non-classical explanation.

3. Controlling the operations of the QFM

In our present study we have involved only very simple protocols to operate the different primitives building a QFM. In a real world implementation, one would naturally like to speed up and optimize the different steps of a QFM. This should be in fact expected to be a crucial matter. This can be done by implementing optimal control methods [77–80], such as those reported for splitting a double well in Ref. [76] or for the excitation process in Ref. [81]. Notably, some of the control theory is already established for the piston QTP and has been successfully implemented [43]. There, a harmonic trapping potential was considered and the extension of the GP profile has stably been modified. This involved the fact that modifying a harmonic trapping potential acts essentially as a *lens* for the individual atoms making up the system, so not only one can compress them appropriately but also accurately decelerate them when needed.

4. Diagnostic tools for QFMs

Finally, a particularly important direction to study is the development of further diagnostic techniques for the system along the lines of recent developments [26, 35, 36, 45–53, 58, 72, 82, 83]. We have discussed in Sec. III C and App. A the current experimental read-out capabilities and have proposed how to enhance them by novel variants of tomographic data analysis [36]. Detailed *monitoring of the QFM* will be crucial and novel *hardware* solutions can aid that goal.

A particularly interesting possibility is to trap a three-dimensional condensate close to the one-dimensional QFM and use it as a sensing device. Matter-wave interference between two systems of different dimensionality seems to be interesting in its own right offering to study a wealth of various physical phenomena [53, 72]. In addition, it could be expected to provide additional read-out resources with the goal of circumventing the current imaging resolution limitations that are difficult to improve otherwise. The implementation of this scheme would have the advantage of providing a direct measurement of the phase along of a single quasi-condensate in contrast of the indirect tomographic approach. See, e.g., Ref. [58] for related work in this direction.

Finally, let us remark about the possibility of performing *non-destructive* measurements which are essential, e.g., for an analysis of a thermodynamical process using fluctuation relation theorems which involves a two-step measurement process on the same system. Currently the measurements performed in experiments using the Atom Chip are destructive, see, e.g., Ref. [53, 84] for a discussion of measurements following a time-of-flight expansion. When experimenting with 1D systems destructive measurements are experimentally easier because of the small atom number. In that case one can illuminate the complete system for read-out and every atom scatters many photons. Measuring in time of flight has the additional advantage that the atomic cloud which is initially only a few 100 nm in transverse size, can expand transversely to a size that is above the resolution limit of the imaging optics (as used in Refs. [85, 86]). For long time of flight the atoms have moved away from the Atom Chip elements that were being used for the control in the experiment, thus reducing spurious light scattering that can contaminate the pictures. Such a measurement is destructive in two ways: (1) the gas is released from the trap, (2) as the atoms are heated up so much by the light scattering that the low-energy quasi-condensate description for the atomic cloud is not valid anymore: the BEC evaporates unless the system is large [87–92]. Thus, non-destructive measurements in our system can not be performed by illuminating the atoms for read-out multiple times but rather in a less disruptive way, e.g., by *out-coupling* of atoms [88]. Here, one would like to remove selectively atoms from a portion of the system and measure these projectively away from the system. This has the advantage that the system will not be destroyed and the measurement can be repeated. Additionally, imaging *individual* out-coupled atoms allows to consider *quantum limited* measurements [93, 94]. However, the mechanical effects of even the second order Zeeman effect in the strong magnetic field gradients of the chip traps,

which are still on to keep the remaining system running, make these measurements more difficult. Still, these engineering challenges could be overcome in near-term.

For applications in quantum thermodynamics and fluctuation relation theorems, it should be noted that these measurements would be local in space (product measurements of commuting observables). This is in contrast to many protocols assuming projective measurements in the entangled and non-local *energy eigenbasis* – in general it is not clear how to achieve these experimentally demanding requirements in quantum many-body systems.

As a final outlook, let us remark that measurements using outcoupled atoms could potentially allow for implementing error mitigation for the refrigeration QFM: When merging two systems, the number of excitations will be influenced by phase diffusion of the phase zero-mode and the measurement of the relative phase between the outcoupled atoms could allow to select the experimental runs that happen to have fewer excitations than the average realization. Assessing the backaction on the system and the influence on the performance of the QFM in such a scheme is an interesting question for future study.

B. The role of information in the QFM

If we could – fictitiously – precisely measure the many-body eigenstates of our complete machine, we could in principle achieve complete control about the system. Needless to say, in a quantum many-body system as we consider here, this becomes impractical and we have to restrict ourselves to physically relevant, local, few-body observables and a finite set of their correlations. Ref. [35] provides an overview on how far one can presently experimentally go in such endeavors. These limitations will define what we can possibly know about the system and what we can hence make elaborate use of – and what we are bound not to be able to know and therefore need to ignore. When putting this mindset into the context of assessing energy contributions, the first type of energy referring to known properties can in the widest sense be related to *work*, the latter to *heat* and entropy. Ultimately, it is the amount of information one has about the energy present in the system which decides whether it should be interpreted as heat or work [1, 95–100].

Aside from the conceptual issue of separating work and heat, much progress has also been made in theoretical quantum thermodynamics, in terms of predictions of how energy exchange in finite-sized quantum systems would occur. We highlight several important aspects in this section. The manipulation of one-dimensional quasi-condensates via relatively simple yet highly controlled thermodynamic processes in the deep quantum regime seems to be an ideal test-bed for such considerations.

1. Correlations

An interesting future direction is the exploration of the question whether the *elements of the QFM are correlated*, of

how to quantify and control these correlations, and how to make use of them explicitly in the design of a QFM. The coupling and de-coupling of two interacting many-body systems, i.e., the operation of the valve QTP, is a direct way to induce correlations or even entangle the two.

The canonical example thereby is the double well, that has a physics similar to a beam-splitter in quantum optics. When the de-coupling is slower than the time scale given by the interaction energy, the two systems will build up *quantum correlations*, which persist even if they are separated [75, 101, 102]. An indication that this also works for the excitations in a many-body system described by an effective quantum field theory is the observation of number squeezing in the modes created by slow splitting [56].

In our simulations we assumed *de-phasing* to occur after we split the systems, i.e., the correlations between the elements of the QFM are modeled to be lost every time splitting is completed. However, this has to be studied alongside with experiments, in order to understand whether this de-phasing of correlations between parts of the QFM occurs.

The engineering of such correlations is an important question especially in the context of *work extraction* [103], since they may produce interesting dynamics, such as a reverse in heat flow direction – usually referred to as *anomalous heat flow* [104–108] – or even providing a way of implementing the extraction of macroscopic work probabilistically from a heat bath [109].

Refs. [32, 56] uncovered signatures of quantum noise and squeezing during longitudinal splitting of the quasi-condensates. This is an exciting indication that it can be possible to reveal (with statistical significance) the presence of entanglement under similar conditions, e.g., quantum correlations between eigen-modes reflecting the effect of various perturbations that can be applied.

Further lowering the currently accessible temperatures will allow to enter the few phonon regime in which quantum vacuum fluctuations will certainly become manifest. These features are closely connected to entanglement in real space [110, 111] because the phononic vacuum is entangled in real space as can be understood via arguments from conformal field theory [112]. In this regime, the thermal coherence length λ_T will be comparable to the system size and phase correlations will decay polynomially instead of exponentially.

2. Non-Markovian effects

A further interesting and promising feature of our system is that it can be used as a test-bed for observing the impact of non-Markovian effects [113–116] on thermodynamic operations. Such dynamics originate from the intermediate size of the bath so that a back-flow of information occurs. The presumably principal source of non-Markovianity is hinted at in Fig. 6, where we see that the wave-packets injected by operating the valve get reflected from the boundaries of the system and come back to the position of their origin in finite time, in fierce violation of any meaningful Markov approximation. Notably, this effect should be expected to hold also in presence of weak non-Gaussian perturbations as various Atom

Chip experiments have already experimentally demonstrated that these features remain intact in close to integrable situations, also in presence of non-trivial trap geometries.

In most works on quantum thermodynamics, see Refs. [117, 118] for reviews, an infinite bath is considered, but it is unclear under which conditions these modeling assumptions would be valid for the intermediate-sized baths in a QFM experiment. The studies of such local recurrences can be seen as entry points to interesting theoretical studies of the possible repercussions of wave-packets returning back to their origin in *finite* time.

Loss of information ultimately proceeds through de-phasing of collective excitations. For quasi-condensates these are phonons [32, 119, 120], the de-phased state emerges in a light-cone fashion [55], and is described by a generalized Gibbs ensemble [56], i.e., different modes can have effectively different temperatures determined by the state preparation.

The long time behavior depends on the spectrum of these collective modes. If the atoms are confined to a box shaped trap, then the phonon frequencies become commensurate, i.e. $\omega_k = \pi ck/L$, with $k = 1, 2, \dots$ being the mode index, and *recurrences* are observable at short times [25, 121]. This effect is a distinct source of non-Markovianity from the localized wave-packets returning to their origin in finite time and can occur even in a *homogeneous* system. As detailed in Ref. [36] the recurrence is a recurrence of the squeezed (momentum) modes, where each mode k is represented by an ellipse in phase space rotating around the origin with frequency ω_k and all ellipses realign their axes as soon as the slowest $k = 1$ mode rotates by a full angle. In that moment the $k = 2$ mode will have made additionally one more full turn, and similarly higher modes too. I.e., due to the linear spectrum all modes realign. This pertains to eigenmode populations and the state in real-space can be homogeneous during the dynamics. This, however, does not occur in a harmonic longitudinal confinement with trap frequency $\omega_{||}$, where the eigenfrequencies are non-linear $\omega_k = \omega_{||} \sqrt{k(k+1)/2}$ [122] and are incommensurate. Still, when the entire system is engineered to be captured by few collective commensurate modes, non-Markovian behavior and significant memory effects can dominate the system dynamics.

Let us illustrate that with an example: The role of the reservoir in a thermal machine cycle will strongly depend on the design of the mode spectrum and on when the “contacts” take place. I.e., the timing of the valve QTPs will matter. If the coupling is in between recurrences, the reservoir will appear de-phased and with seemingly no memory of what happened during the previous cycle. However, the system is coherent: By changing the timing the valve coupling can occur at the time of the recurrence and the reservoir can appear to have memory of what happened during a previous cycle, and hence be a non-Markovian bath. Designing the longitudinal confinement in each part of the thermal machine will allow us to have in principle (nearly) full control of the memory of selected states in the thermal machine at later times. This will allow us to design and probe a large variety of interesting Markovian and non-Markovian situations [123–127].

3. Work extraction

Quantifying work extraction in the quantum regime can be treated by various theoretical frameworks of quantum thermodynamics. For the refrigeration cycle that we have proposed here, the useful output of the QFM is easy to assess, as shown in Fig. 6. This, however, is not as straightforward in general for other tasks that may be implemented with the QTPs that we have presented. In that case, additional ideas for quantifying work extraction will have to be developed in accordance with our modeling involving exclusively unitary processes induced by time-dependent Hamiltonians.

Since we always initialize the quasi-condensates in a thermal state, this process is similar to the standard setting of *fluctuation relations* [128]. However, the statements of work extraction provided by fluctuation relations involve initial and final projective energy measurements on the system which is *not* directly measurable in experiments with quantum many-body systems.

QTPs can be used to perform work on systems and in the process we saw that this brings them out of equilibrium. Therefore, in the *resource-theoretic* framework of quantum thermodynamics [129, 130] they should be interpreted as being *resourceful* and hence stand in contrast to *free* operations and states which are usually studied in this formalism. This highlights the *gap* between this powerful but abstract framework with what is meaningfully achievable in experimental setups. So far, the energetic worth of non-thermal resource states has been studied in the context of distillation rates [131, 132], similar quantifications on the level of operations rather than states might be potentially useful for practical settings.

4. Finite-size effects

Individual realizations of the experiment are subjected to non-negligible thermal fluctuations. A particularly interesting question lies in observing the predictions related to *finite-size effects* derived in various theoretical frameworks of quantum thermodynamics. Our systems are small, and therefore can be heavily influenced by fluctuations in energy. In the various frameworks of quantum thermodynamics, this has typically been captured by additional “thermodynamic laws” which are distinct from the standard laws that are valid in the thermodynamic limit. Such “laws” are essentially constraints which have been phrased in terms of (i) generalized free energies in the context of a resource-theoretic language of quantum thermodynamics [130], (ii) fine-grained Jarzynski equalities [133] or (iii) other measures specifically tailored for Gaussian systems [134]. These are intricate and important theoretical descriptions. But make-or-break questions for the significance of such pictures presumably are the following ones: Can we observe their predictions? Specifically, how relevant are they to characterize the potentials and limits of practical thermodynamic protocols such as the cooling scheme proposed in this work? Much remains to be explored in this direction for quantum many-body systems in contrast to other physical settings where specific ideas have been proposed [135].

5. Fundamental limits of cooling

Another exciting direction is to explore experimentally the *fundamental limits of cooling*, as they are usually captured in readings of the third law(s) of (quantum) thermodynamics. Adapting the terminology from recent works [136, 137], the QTP toolbox can be seen as *coherent* building blocks for a thermal machine, whereas resource-theoretic operations are energy-incoherent. Nevertheless, coherent operations (i.e. time-dependent Hamiltonian control operations) and incoherent operations (i.e. resource-theoretic operations), if both given the same amount of complexity, can achieve similar performance (final energy) in terms of cooling of qubit systems [136]. Therefore, the fundamental bounds obtained from resource-theoretic frameworks in machine performance [99, 130, 138], especially such as the third law derivations [138, 139], may be a valuable reference frame, provided that a fully-rigorous quantification of work cost for these primitives is done.

VII. CONCLUSIONS

In this work, we have set out to devise a blueprint for a genuine quantum thermal machine in one-dimensional ultra-cold atomic gases, a platform that we propose to realize complex thermodynamic tasks. We have proposed a quantum field machine (QFM) involving phononic degrees of freedom described by an effective quantum field theory. When devising this blueprint, resorting to a quantum mechanical description has been crucial to reduce the physical description of the system to a point where the functioning of the machine can be easily grasped. In order to provide guidance towards constructing thermal field machines, we characterize a toolbox of thermodynamic primitives which are macroscopic operations over quasi-condensates, reminiscent of operations acting on bulk systems in conventional thermodynamics. Our proposal puts forward a scheme for a refrigeration QFM that involves a system featuring quantum effects, a cold atomic gas, and the machine performs a useful task – *cooling of phononic quantum fields*. In contrast to previous realizations of quantum engines this cannot be practically achieved by controlling every single degree of freedom of the system as there are just too many. It goes without saying that this task is useful and we hence fully accommodated the three requirements that we have set in the outset of this work for a thermal machine to be a *genuine* quantum machine. We found that quantum effects present in our QFM are currently detrimental to its cause: Operating the valve of the QFM induces inevitable excitations adding thermal noise of reservoirs. This is rooted in the quantum effect of phase diffusion of phase zero-modes and in the dynamical Casimir effect and features a detailed temporal structure thus far ignored. Remarkably, even after accounting for realistic “imperfections” expected in the experiment we predict notable cooling. As detailed, exploring further quantum features is possible, including (i) at sufficiently low temperatures entanglement or zero-point fluctuations leading to sub-Poissonian noise when operating the valve [32, 55], (ii) non-Gaussian

QFMs [35], (iii) non-Markovian QFMs [25], (iv) parallel machines amenable to measurements using matter-wave interferometry [25, 27, 32, 35, 56], (v) quantum phase diffusion and phase-locking via Josephson oscillations [27] (vi) few phonon regime similar to quantum optics in the few photon regime where the quantized nature of the energy spectrum becomes manifest and individual runs of the QFM will unavoidably fluctuate.

It is clear that this work constitutes only a commencing study of a research program of a larger scope. We perform classically efficient numerical simulations but calculations for a non-Gaussian QFM are expected to hit the computational complexity barrier. Even though our operational principles and cycles are reminiscent of those of classical heat engines, i.e., canonical thermodynamical transformations, we highlighted some interesting issues obstructing understanding the functioning of our QFM using resource theories. We encountered quantum features which in the future should, to the contrary of our current observations, be seen not as a burden but as a potential advantage: They should be used to improve the performance of the thermal machine in the deep quantum regime.

Our theoretical model for a Gaussian QFM is expected to largely capture the qualitative operation of the QFM. The quantitative features may change and there is a rich number of entry points for non-Gaussian behavior to set in. We expect their effect to be small and to not overhaul our predictions. Ultimately, whether this will play out to be true in reality can only be decided by performing an experiment.

We firmly believe that such a machine can and should be built which will deepen our understanding of thermodynamics in the quantum regime. Further progress in the research field of quantum thermodynamics necessitates the development of

useful quantum machines to drive, motivate and guide the theoretical development of the corresponding laws, just as the advent of steam engines propelled the development of thermodynamics in the 19th century. It is our hope that the roadmap laid out in this work will serve this cause well.

ACKNOWLEDGEMENTS

We are grateful to Fred Jendrzejewski and Spyros Sotiriadis for useful discussions. M. H. and G. V. acknowledge funding from the Austrian Science Fund (FWF) through the START project Y879-N27 and the Lise-Meitner project M 2462-N 27, M. H. and J. Sch. acknowledge the ESQ Discovery Grant “*Emergence of physical laws: From mathematical foundations to applications in many body physics*”. J. Sab. acknowledges funding from the Austrian Science Fund (FWF) through the DK CoQuS. J. E. acknowledges funding from the DFG CRC 183 (Project A03), the European Unions Horizon2020 research and innovation programme under grant agreement No. 817482 (PASQuanS). Importantly, J. E. and J. Schm. are supported by the DFG Research Unit FOR 2724 on “Thermal machines in the thermal world”. J. Sch., J. E., and M. H. have also received funds from the FQXi (FQXi-IAF19-03-S2) within the project “Fueling quantum field machines with information”, for which the present effort is key. I. M. acknowledges the support by the Wiener Wissenschafts- und Technologiefonds (WWTF) via Grant No. MA16-066 (SEQUEX). J.S., M.P., and Y.O. thank the support from Fundação para a Ciência e a Tecnologia (Portugal), namely through project UIDB/EEA/50008/2020. J.S. acknowledges the support from the DP-PMI and FCT (Portugal).

-
- [1] J. Goold, M. Huber, A. Riera, L. del Rio, and P. Skrzypczyk, *J. Phys. A* **49**, 143001 (2016).
 - [2] G. Kurizki, E. Shahmoon, and A. Zwick, *Phys. Scr.* **90**, 128002 (2015).
 - [3] C. Gogolin and J. Eisert, *Rep. Prog. Phys.* **79**, 56001 (2016).
 - [4] R. Kosloff, *Entropy* **15**, 2100 (2013).
 - [5] J. Millen and A. Xuereb, *New J. Phys.* **18**, 011002 (2016).
 - [6] S. Vinjanampathy and J. Anders, *Contemp. Phys.* **57**, 545 (2016).
 - [7] W. Niedenzu, I. Mazets, G. Kurizki, and F. Jendrzejewski, *Quantum* **3**, 155 (2019).
 - [8] J. Roßnagel, S. Dawkins, N. Tolazzi, O. Abah, E. Lutz, F. Schmidt-Kaler, and K. Singer, *Science* **352**, 325 (2016).
 - [9] D. von Lindenfels, O. Gräß, C. T. Schmiegelow, V. Kaushal, J. Schulz, M. T. Mitchison, J. Goold, F. Schmidt-Kaler, and U. G. Poschinger, *Phys. Rev. Lett.* **123**, 080602 (2019).
 - [10] J. P. Pekola, *Nature Phys.* **11**, 118 (2015).
 - [11] J. Schmiedmayer, in *Thermodynamics in the Quantum Regime*, edited by F. Binder, L. A. Correa, C. Gogolin, J. Anders, and G. Adesso (Springer Nature, 2018) Chap. 34, pp. 823–851, arXiv:1805.11539.
 - [12] M. A. Cazalilla, *J. Phys. B* **37**, S1 (2004).
 - [13] T. Giamarchi, *Quantum physics in one dimension* (Clarendon Press, Oxford, 2004).
 - [14] R. Folman, P. Krüger, D. Cassettari, B. Hessmo, T. Maier, and J. Schmiedmayer, *Phys. Rev. Lett.* **84**, 4749 (2000).
 - [15] R. Folman, P. Krüger, J. Schmiedmayer, J. Denschlag, and C. Henkel (Academic Press, 2002) pp. 263 – 356.
 - [16] J. Reichel and V. Vuletic, *Atom chips* (John Wiley & Sons, 2011).
 - [17] M. Tajik, B. Rauer, T. Schweigler, F. Cataldini, J. ao Sabino, F. S. Møller, S.-C. Ji, I. E. Mazets, and J. Schmiedmayer, *Opt. Express* **27**, 33474 (2019).
 - [18] C. Mora and Y. Castin, *Phys. Rev. A* **67**, 053615 (2003).
 - [19] V. N. Popov, *Functional integrals in quantum field theory and statistical physics*, Vol. 8 (Springer Science & Business Media, 2001).
 - [20] D. S. Petrov, G. V. Shlyapnikov, and J. T. M. Walraven, *Phys. Rev. Lett.* **85**, 3745 (2000).
 - [21] M. Lewenstein and L. You, *Phys. Rev. Lett.* **77**, 3489 (1996).
 - [22] J. Javanainen and M. Wilkens, *Phys. Rev. Lett.* **78**, 4675 (1997).
 - [23] A. J. Leggett and F. Sols, *Phys. Rev. Lett.* **81**, 1344 (1998).
 - [24] J. Javanainen and M. Wilkens, *Phys. Rev. Lett.* **81**, 1345 (1998).

- [25] B. Rauer, S. Erne, T. Schweigler, F. Cataldini, M. Tajik, and J. Schmiedmayer, *Science* **359**, on (2018).
- [26] T. Schweigler, *Correlations and dynamics of tunnel-coupled one-dimensional Bose gases*, Ph.D. thesis (2019).
- [27] M. Pigneur, T. Berrada, M. Bonneau, T. Schumm, E. Demler, and J. Schmiedmayer, *Phys. Rev. Lett.* **120**, 173601 (2018).
- [28] M. Pigneur and J. Schmiedmayer, *Phys. Rev. A* **98**, 063632 (2018).
- [29] Y. Kagan, D. L. Kovrizhin, and L. A. Maksimov, *Phys. Rev. Lett.* **90**, 130402 (2003).
- [30] V. Gritsev, A. Polkovnikov, and E. Demler, *Phys. Rev. B* **75**, 174511 (2007).
- [31] C. Menotti, J. R. Anglin, J. I. Cirac, and P. Zoller, *Phys. Rev. A* **63**, 023601 (2001).
- [32] M. Gring, M. Kuhnert, T. Langen, T. Kitagawa, B. Rauer, M. Schreitl, I. E. Mazets, D. A. Smith, E. Demler, and J. Schmiedmayer, *Science* **337**, 1318 (2012).
- [33] I. Carusotto, R. Balbinot, A. Fabbri, and A. Recati, *The European Physical Journal D* **56**, 391 (2010).
- [34] M. H. Michael, J. Schmiedmayer, and E. Demler, *Phys. Rev. A* **99**, 053615 (2019).
- [35] T. Schweigler, V. Kasper, S. Erne, I. E. Mazets, B. Rauer, F. Cataldini, T. Langen, T. Gasenzer, J. Berges, and J. Schmiedmayer, *Nature* **545**, 323 (2017).
- [36] M. Gluza, T. Schweigler, B. Rauer, C. Krumnow, J. Schmiedmayer, and J. Eisert, *Comm. Phys.* **3**, 12 (2020).
- [37] F. D. M. Haldane, *J. Phys. C* **14**, 2585 (1981).
- [38] T. Giamarchi, *Quantum physics in one dimension* (Clarendon Press, Oxford, 2004).
- [39] J. I. Cirac and P. Zoller, *Nature Phys.* **8**, 264 (2012).
- [40] I. Bloch, J. Dalibard, and S. Nascimbene, *Nature Phys.* **8**, 267 (2012).
- [41] J. Eisert, M. Friesdorf, and C. Gogolin, *Nature Phys.* **11**, 124 (2015).
- [42] T. Langen, R. Geiger, M. Kuhnert, B. Rauer, and J. Schmiedmayer, *Nature Phys.* **9**, 640 (2013).
- [43] W. Rohringer, D. Fischer, F. Steiner, I. E. Mazets, J. Schmiedmayer, and M. Trupke, *Scientific Rep.* **5**, 9820 (2015).
- [44] V. Gritsev, P. Barmettler, and E. Demler, *New Journal of Physics* **12**, 113005 (2010).
- [45] M. Schemmer, A. Johnson, and I. Bouchoule, *Phys. Rev. A* **98**, 043604 (2018).
- [46] B. Fang, A. Johnson, T. Roscilde, and I. Bouchoule, *Phys. Rev. Lett.* **116**, 050402 (2016).
- [47] J. Armijo, T. Jacqmin, K. V. Kheruntsyan, and I. Bouchoule, *Phys. Rev. Lett.* **105**, 230402 (2010).
- [48] J. Esteve, J.-B. Trebbia, T. Schumm, A. Aspect, C. I. Westbrook, and I. Bouchoule, *Phys. Rev. Lett.* **96**, 130403 (2006).
- [49] T. Jacqmin, J. Armijo, T. Berrada, K. V. Kheruntsyan, and I. Bouchoule, *Phys. Rev. Lett.* **106**, 230405 (2011).
- [50] A. Imambekov, I. E. Mazets, D. S. Petrov, V. Gritsev, S. Manz, S. Hofferberth, T. Schumm, E. Demler, and J. Schmiedmayer, *Phys. Rev. A* **80**, 033604 (2009).
- [51] S. Manz, *Density correlations of expanding one-dimensional Bose gases*, Ph.D. thesis, Vienna University of Technology (2011).
- [52] T. Schumm, S. Hofferberth, L. M. Andersson, S. Wildermuth, S. Groth, I. Bar-Joseph, J. Schmiedmayer, and P. Krüger, *Nature Phys.* **1**, 57 (2005).
- [53] Y. D. van Nieuwkerk, J. Schmiedmayer, and F. H. L. Essler, *Scipost Phys.* **5**, 046 (2018).
- [54] S. Hofferberth, I. Lesanovsky, T. Schumm, A. Imambekov, V. Gritsev, E. Demler, and J. Schmiedmayer, *Nature Phys.* **4**, 489 (2008).
- [55] T. Langen, R. Geiger, M. Kuhnert, B. Rauer, and J. Schmiedmayer, *Nature Physics* **9**, 640 (2013).
- [56] T. Langen, S. Erne, R. Geiger, B. Rauer, T. Schweigler, M. Kuhnert, W. Rohringer, I. E. Mazets, T. Gasenzer, and J. Schmiedmayer, *Science* **348**, 207 (2015).
- [57] T. Schweigler, *Correlations and dynamics of tunnel-coupled one-dimensional Bose gases*, Ph.D. thesis (2019).
- [58] M. Aidelsburger, J. L. Ville, R. Saint-Jalm, S. Nascimbène, J. Dalibard, and J. Beugnon, *Phys. Rev. Lett.* **119**, 190403 (2017).
- [59] C. Menotti, J. R. Anglin, J. I. Cirac, and P. Zoller, *Phys. Rev. A* **63**, 023601 (2001).
- [60] We have chosen the peak density to reflect typical experiments realized in a box trap of size $L = 50 \mu\text{m}$ with $N_{\text{atoms}} = 5000$ atoms. The fall-off at the edges according to the erf-function was chosen purely phenomenologically and was not motivated by a specific trapping field V that would realize it - any trap that is not infinitely strong will lead to a smoothed fall-off at the edges.
- [61] B. Rauer, P. Grišins, I. E. Mazets, T. Schweigler, W. Rohringer, R. Geiger, T. Langen, and J. Schmiedmayer, *Phys. Rev. Lett.* **116**, 030402 (2016).
- [62] I. Kukuljan, S. Sotiriadis, and G. Takacs, *Phys. Rev. Lett.* **121**, 110402 (2018).
- [63] V. Narasimhachar, S. Assad, F. C. Binder, J. Thompson, B. Yadin, and M. Gu, *arXiv preprint arXiv:1909.07364* (2019).
- [64] S. Coleman, *Phys. Rev. D* **11**, 2088 (1975).
- [65] S. Mandelstam, *Phys. Rev. D* **11**, 3026 (1975).
- [66] W. E. Thirring, *Ann. Phys.* **3**, 91 (1958).
- [67] L. D. Faddeev and V. E. Korepin, *Phys. Rep.* **42**, 1 (1978).
- [68] V. Gritsev, A. Polkovnikov, and E. Demler, *Phys. Rev. B* **75**, 174511 (2007).
- [69] These fields are obtained by considering the difference of the respective fields of each of the condensates, see, e.g., Ref. [25] for a detailed discussion in relation to a recent experiment.
- [70] T. V. Zache, T. Schweigler, S. Erne, J. Schmiedmayer, and J. Berges, *Phys. Rev. X* **10**, 11020 (2020).
- [71] A. D. Cronin, J. Schmiedmayer, and D. E. Pritchard, *Reviews of Modern Physics* **81**, 1051 (2009).
- [72] J.-F. Schaff, T. Langen, and J. Schmiedmayer, *Rivista del Nuovo Cimento della Societa Italiana di Fisica* **37**, 509 (2014).
- [73] T. Langen, M. Gring, M. Kuhnert, B. Rauer, R. Geiger, D. Adu Smith, I. E. Mazets, and J. Schmiedmayer, *Eur. Phys. J. Special Topics* **217**, 43 (2013).
- [74] T. Schweigler, M. Gluza, M. Tajik, S. Sotiriadis, F. Cataldini, S.-C. Ji, F. S. Møller, J. Sabino, B. Rauer, J. Eisert, and S. J., *arXiv:2003.01808* (2020).
- [75] T. Berrada, S. V. Frank, R. Bückner, T. Schumm, J.-F. Schaff, and J. Schmiedmayer, *Nature Comm.* **4**, 2077 (2013).
- [76] J. Grond, J. Schmiedmayer, and U. Hohenester, *Phys. Rev. A* **79**, 021603 (2009).
- [77] J. Werschnik and E. Gross, *Journal of Physics B: Atomic, Molecular and Optical Physics* **40**, R175 (2007).
- [78] T. Caneva, M. Murphy, T. Calarco, R. Fazio, S. Montangero, V. Giovannetti, and G. E. Santoro, *Phys. Rev. Lett.* **103**, 240501 (2009).
- [79] P. Doria, T. Calarco, and S. Montangero, *Phys. Rev. Lett.* **106**, 190501 (2011).
- [80] C. P. Koch, *Journal of Physics: Condensed Matter* **28**, 213001 (2016).
- [81] S. van Frank, M. Bonneau, J. Schmiedmayer, S. Hild, C. Gross, M. Cheneau, I. Bloch, T. Pichler, A. Negretti, T. Calarco, and S. Montangero, *Scientific Rep.* **6**, 34187

- (2016).
- [82] P. Hauke, M. Lewenstein, and A. Eckardt, *Phys. Rev. Lett.* **113**, 045303 (2014).
 - [83] J. Eisert, D. Hangleiter, N. Walk, I. Roth, D. Markham, R. Parekh, U. Chabaud, and E. Kashefi, (2019), arXiv:1910.06343.
 - [84] D. A. Smith, S. Aigner, S. Hofferberth, M. Gring, M. Andersson, S. Wildermuth, P. Krüger, S. Schneider, T. Schumm, and J. Schmiedmayer, *Optics express* **19**, 8471 (2011).
 - [85] S. Wildermuth, S. Hofferberth, I. Lesanovsky, E. Haller, L. M. Andersson, S. Groth, I. Bar-Joseph, P. Krüger, and J. Schmiedmayer, *Nature* **435**, 440 (2005).
 - [86] S. Aigner, L. Della Pietra, Y. Japha, O. Entin-Wohlman, T. David, R. Salem, R. Folman, and J. Schmiedmayer, *Science* **319**, 1226 (2008).
 - [87] M. Andrews, M.-O. Mewes, N. Van Druten, D. Durfee, D. Kurn, and W. Ketterle, *Science* **273**, 84 (1996).
 - [88] M. Saba, T. Pasquini, C. Sanner, Y. Shin, W. Ketterle, and D. Pritchard, *Science* **307**, 1945 (2005).
 - [89] D. Freilich, D. Bianchi, A. Kaufman, T. Langin, and D. Hall, *Science* **329**, 1182 (2010).
 - [90] M. J. H. Ku, B. Mukherjee, T. Yefsah, and M. W. Zwierlein, *Phys. Rev. Lett.* **116**, 045304 (2016).
 - [91] S. Serafini, L. Galantucci, E. Iseni, T. Bienaimé, R. N. Bisset, C. F. Barengi, F. Dalfovo, G. Lamporesi, and G. Ferrari, *Phys. Rev. X* **7**, 021031 (2017).
 - [92] E. M. Seroka, A. V. Curiel, D. Trypogeorgos, N. Lundblad, and I. B. Spielman, *Opt. Express* **27**, 36611 (ts , url = <http://www.opticsexpress.org/abstract.cfm?URI=oe-27-25-36611>, doi = 10.1364/OE.27.036611,).
 - [93] R. Bücker, A. Perrin, S. Manz, T. Betz, C. Koller, T. Plisson, J. Rottmann, T. Schumm, and J. Schmiedmayer, *New Journal of Physics* **11**, 103039 (2009).
 - [94] A. Bergschneider, V. M. Klinkhamer, J. H. Becher, R. Klemt, G. Zürn, P. M. Preiss, and S. Jochim, *Phys. Rev. A* **97**, 063613 (2018).
 - [95] R. Gallego, J. Eisert, and H. Wilming, *New J. Phys.* **18**, 103017 (2016).
 - [96] L. del Rio, L. Kraemer, and R. Renner, (2015), arXiv:1511.08818.
 - [97] M. Perarnau-Llobet, K. V. Hovhannisyanyan, M. Huber, P. Skrzypczyk, N. Brunner, and A. Acin, *Phys. Rev. X* **5**, 041011 (2015).
 - [98] N. Brunner, M. Huber, N. Linden, S. Popescu, R. Silva, and P. Skrzypczyk, *Phys. Rev. E* **89**, 032115 (2014).
 - [99] M. P. Woods, N. H. Y. Ng, and S. Wehner, *Quantum* **3**, 177 (2019).
 - [100] N. H. Y. Ng, M. P. Woods, and S. Wehner, *New J. Phys.* **19**, 113005 (2017).
 - [101] G.-B. Jo, Y. Shin, S. Will, T. A. Pasquini, M. Saba, W. Ketterle, D. E. Pritchard, M. Vengalattore, and M. Prentiss, *Phys. Rev. Lett.* **98**, 030407 (2007).
 - [102] J. Estève, C. Gross, a. Weller, S. Giovanazzi, and M. K. Oberthaler, *Nature* **455**, 1216 (2008).
 - [103] L. del Rio, J. Aberg, R. Renner, O. Dahlsten, and V. Vedral, *Nature* **474**, 61 (2011).
 - [104] D. Jennings and T. Rudolph, *Phys. Rev. E* **81**, 061130 (2010).
 - [105] K. Micadei, J. P. Peterson, A. M. Souza, R. S. Sarthour, I. S. Oliveira, G. T. Landi, T. B. Batalhão, R. M. Serra, and E. Lutz, *Nature Comm.* **10**, 2456 (2019).
 - [106] D. Jennings and T. Rudolph, *Phys. Rev. E* **81**, 061130 (2010).
 - [107] S. Jevtic, D. Jennings, and T. Rudolph, *Phys. Rev. Lett.* **108**, 110403 (2012).
 - [108] L. del Rio, A. Hutter, R. Renner, and S. Wehner, *Phys. Rev. E* **94**, 022104 (2016).
 - [109] P. Boes, R. Gallego, N. H. Ng, J. Eisert, and H. Wilming, *Quantum* **4**, 231 (2020).
 - [110] J. Anders and A. Winter, arXiv preprint arXiv:0705.3026 (2007).
 - [111] J. Anders, *Phys. Rev. A* **77**, 062102 (2008).
 - [112] P. Calabrese and J. Cardy, *Journal of Statistical Mechanics: Theory and Experiment* **2004**, P06002 (2004).
 - [113] M. M. Wolf, J. Eisert, T. S. Cubitt, and J. I. Cirac, *Phys. Rev. Lett.* **101**, 150402 (2008).
 - [114] A. Rivas, S. F. Huelga, and M. B. Plenio, *Phys. Rev. Lett.* **105**, 050403 (2010).
 - [115] H.-P. Breuer, E.-M. Laine, J. Piilo, and B. Vacchini, *Rev. Mod. Phys.* **88**, 021002 (2016).
 - [116] A. Rivas, S. F. Huelga, and M. B. Plenio, *Rep. Prog. Phys.* **77**, 094001 (2014).
 - [117] G. Gour, M. P. Müller, V. Narasimhachar, R. W. Spekkens, and N. Y. Halpern, *Physics Reports* **583**, 1 (2015).
 - [118] S. Vinjanampathy and J. Anders, *Contemporary Physics* **57**, 545 (2016).
 - [119] R. Bistritzer and E. Altman, *Proc. Natl. Ac. Sc.* **104**, 9955 (2007).
 - [120] T. Kitagawa, A. Imambekov, J. Schmiedmayer, and E. Demler, *New J. Phys.* **13**, 073018 (2011).
 - [121] R. Geiger, T. Langen, I. E. Mazets, and J. Schmiedmayer, *New J. Phys.* **16**, 053034 (2014).
 - [122] D. S. Petrov, G. V. Shlyapnikov, and J. T. M. Walraven, *Phys. Rev. Lett.* **85**, 3745 (2000).
 - [123] M. Pezzutto, M. Paternostro, and Y. Omar, *New J. Phys.* **18**, 123018 (2016).
 - [124] P. P. Hofer, M. Perarnau-Llobet, L. D. M. Miranda, G. Haack, R. Silva, J. B. Brask, and N. Brunner, *New J. Phys.* **19**, 123037 (2017).
 - [125] J. O. González, L. A. Correa, G. Nocerino, J. P. Palao, D. Alonso, and G. Adesso, *Open Systems & Information Dynamics* **24**, 1740010 (2017).
 - [126] R. Uzdin, A. Levy, and R. Kosloff, *Entropy* **18**, 124 (2016).
 - [127] S. Groeblacher, A. Trubarov, N. Prigge, M. Aspelmeyer, and J. Eisert, *Nature Comm.* **6**, 7606 (2015).
 - [128] C. Jarzynski, *Phys. Rev. Lett.* **78**, 2690 (1997).
 - [129] M. Horodecki and J. Oppenheim, *Nature Comm.* **4**, 2059 (2013).
 - [130] F. Brandao, M. Horodecki, N. Ng, J. Oppenheim, and S. Wehner, *Proc. Natl. Ac. Sc.* **112**, 3275 (2015).
 - [131] F. G. S. L. Brandao, M. Horodecki, J. Oppenheim, J. M. Renes, and R. W. Spekkens, *Phys. Rev. Lett.* **111**, 250404 (2013).
 - [132] C. T. Chubb, M. Tomamichel, and K. Korzekwa, *Quantum* **2**, 108 (2018).
 - [133] Á. M. Alhambra, L. Masanes, J. Oppenheim, and C. Perry, *Phys. Rev. X* **6**, 041017 (2016).
 - [134] A. Serafini, M. Lostaglio, S. Longden, U. Shackerley-Bennett, C.-Y. Hsieh, and G. Adesso, arXiv:1909.06123 (2019).
 - [135] N. Y. Halpern and D. T. Limmer, arXiv:1811.06551 (2018).
 - [136] F. Clivaz, R. Silva, G. Haack, J. B. Brask, N. Brunner, and M. Huber, *Phys. Rev. Lett.* **123**, 170605 (2019).
 - [137] F. Clivaz, R. Silva, G. Haack, J. B. Brask, N. Brunner, and M. Huber, *Phys. Rev. E* **100**, 042130 (2019).
 - [138] H. Wilming and R. Gallego, *Phys. Rev. X* **7**, 041033 (2017).
 - [139] L. Masanes and J. Oppenheim, *Nature Comm.* **8**, 14538 (2017).
 - [140] C. Weedbrook, S. Pirandola, R. Garcia-Patron, N. J. Cerf, T. C. Ralph, J. H. Shapiro, and S. Lloyd, *Rev. Mod. Phys.* **84**, 621

- (2012).
- [141] J. Eisert and M. B. Plenio, *Int. J. Quant. Inf.* **1**, 479 (2003).
- [142] This means that the density matrix has no zero eigenvalue.
- [143] C. Mora and Y. Castin, *Phys. Rev. A* **67**, 053615 (2003).
- [144] J. Javanainen, *Phys. Rev. A* **60**, 4902 (1999).
- [145] L. Salasnich, A. Parola, and L. Reatto, *Phys. Rev. A* **65**, 043614 (2002).
- [146] M. Gluza, J. Eisert, and T. Farrelly, *SciPost Phys.* **7**, 38 (2019).
- [147] N. K. Whitlock and I. Bouchoule, *Phys. Rev. A* **68**, 053609 (2003).
- [148] F. Dalfovo, S. Giorgini, L. P. Pitaevskii, and S. Stringari, *Rev. Mod. Phys.* **71**, 463 (1999).
-

SUPPLEMENTARY MATERIAL

The supplementary material provides sections accompanying the discussion presented in the main text as follows. We begin by giving in App. A more details about the precise quantities that can be measured in experiments on the Atom Chip and discuss how to connect these to thermodynamical quantities. Next, in App. B we summarize the essential ingredients of the bosonic Gaussian formalism which is the analytical base for the numerical code that produced our results. Finally, App. C provides an extended discussion on simulation details, including precise formulation of the lattice approximation employed in the code, extended description of the valve QTP (including how to compute the energy density or compare to the continuum limit in the scenario of sudden (quench) merging), of the piston QTP (including additional discussion of the model, compression dynamics and details of coupling inhomogenous QFTs after compression) and finally we discuss different relaxations of parameter constraints that have yielded almost 30% cooling ratio.

Appendix A: Experimentally monitoring thermodynamic transformations in phononic quantum simulators

Let us begin by discussing which quantities, if measured experimentally, would reveal insights about the thermodynamic transformations in the system. We then proceed by explaining what are the direct experimental observables and how to connect to the desirable thermodynamical observables. In experiments, one should distinguish the cases of having a single quasi-condensates and two which are adjacent. First let us discuss the former case where we have access to measurements of the atom numbers locally by transversal density absorption imaging (from the side). These numbers will be ultimately binned together due to finite resolution. The recovered atom number per bin $N_i(z_j, t)$ will fluctuate randomly between realizations i and will give spatially resolved data where z_j can be measured in steps of about $\Delta z_{\text{res}} = 2 \mu\text{m}$ on the Atom Chip. The quantities obtained for this lattice can be compared to theory by convoluting the continuum quantities by a Gaussian function with $\sigma_{\text{res}} = 3 \mu\text{m}$ and evaluating [26, 36]. After taking this data at a given time t one can obtain the density fluctuations as follows. The empirical mean of the observable random variable $N_i(z_j, t)$ gives access to the GP profile

$$\rho_0(z_j, t) \approx \frac{1}{M} \sum_{i=1}^M N_i(z_j, t). \quad (\text{A1})$$

After subtracting these values from the individual realizations and squaring the shifted random variable we obtain the estimator

$$\Gamma^{\rho\rho}(z_j, z_{j'}, t_i) \approx \frac{1}{M} \sum_{i=1}^M (N_i(z_j, t_i) - \rho_0(z)) (N_i(z_{j'}, t_i) - \rho_0(z)) . \quad (\text{A2})$$

Indeed, what we obtain by this is nothing else than the estimate the second moments of density fluctuations away from the mean density of the quasi-condensates. The on-site correlation gives information about the energy of phonons. The total energy in the system can be obtained by considering the formal expression for expectation value of the TLL Hamiltonian

$$\langle \hat{H}[\rho_0] \rangle = \int dz \left[\frac{\hbar^2 \rho_0(z)}{2m} \langle (\partial_z \hat{\varphi}(z))^2 \rangle + \frac{g}{2} \langle \delta \hat{\varrho}(z)^2 \rangle \right]. \quad (\text{A3})$$

Of course in the experiment one can only measure at discrete positions but what we can do is try to obtain this quantity via a finite Riemann sum, specifically in the density sector we find

$$E_\rho(t) = \frac{g}{2} \int dz \langle \delta \hat{\varrho}(z)^2 \rangle \approx \frac{g}{2} \sum_j C^{\rho\rho}(z_j, z_j, t_i) \Delta z_{\text{res}} . \quad (\text{A4})$$

By considering the summand in this expression we get access to the energy density for the density fluctuations. Studying how it changes in time between different pixel positions z_j will then give information about the dynamics of the energy of density fluctuations in the system.

For the single quasi-condensate, as explained in the main text, it is not possible to measure directly the phase fluctuations. This is important, however, in order to assess the energy contribution coming from the gradient of the phase operator. This information can be obtained via a tomographic approach by studying the velocities of wave-packets going through the system, as demonstrated recently [36]. The basic idea is that the TLL Hamiltonian can be put to a normal form

$$\hat{H} = \sum_{k>0} \frac{\hbar \omega_k}{2} (\hat{\varphi}_k^2 + \delta \hat{\varrho}_k^2) + \frac{g}{2} \delta \hat{\varrho}_0^2 \quad (\text{A5})$$

using the eigenmode operators $\hat{\varphi}_k, \delta\hat{\varrho}_k$ that depend on the GP profile arising from cosine eigenfunctions in the homogeneous case. We then find that the dynamics of the density fluctuation operator reveals information about the phase operator by means of the relation

$$\delta\hat{\varrho}_k(t) = \cos(\omega_k t)\delta\hat{\varrho}_k + \sin(\omega_k t)\hat{\varphi}_k. \quad (\text{A6})$$

Exploiting this expression to relate observables at different times and using the analysis and reconstruction methods developed in Ref. [36] should then give access to the second moments of the phase fluctuations. Specifically, one would reconstruct the second moments $C_{k,k'}^{\phi\phi} = \langle \hat{\varphi}_k \hat{\varphi}_{k'} \rangle$ of eigenmodes k, k' and we can obtain the total energy contained in the phase sector by simply summing

$$E_\phi(t) = \frac{1}{2} \sum_{k>0} \hbar\omega_k C_{k,k}^{\phi\phi}(t). \quad (\text{A7})$$

Additionally, one can translate the second moments of the eigenmodes to real space after performing the derivative on the eigenfunctions which should give the local information about the energy. When considering two condensates one has access to interferometric measurements of the relative phase fluctuations $\hat{\varphi}_{\text{rel}} = \hat{\varphi}_1 - \hat{\varphi}_2$ between two quasi-condensates and based on non-equilibrium variations of that observable, relative density fluctuations $\delta\hat{\varrho}_{\text{rel}} = \delta\hat{\varrho}_1 - \delta\hat{\varrho}_2$ were reconstructed in Ref. [36]. Density absorption is still available to measure density fluctuations of the common degrees of freedom $\delta\hat{\varrho}_{\text{com}} = \delta\hat{\varrho}_1 + \delta\hat{\varrho}_2$ but is usually less revealing.

Appendix B: Gaussian models in the simulations of QTPs

The continuous Hamiltonian given in Eq. (2) can be appropriately discretized, which we explain in Section C 1. The system can then be described in terms of quadrature operators, in particular, one can describe the quantum states and dynamics with the Gaussian framework of covariance matrices and symplectic transformations. In this section, we present a short summary of the formalism of Gaussian quantum information, see, e.g., Refs. [140, 141] for more complete reviews on the subject.

We consider bosonic systems of N bosonic modes, associated with quadratures

$$\hat{\mathbf{X}} := (\hat{q}_1, \hat{q}_2, \dots, \hat{q}_N, \hat{p}_1, \hat{p}_2, \dots, \hat{p}_N)^T \quad (\text{B1})$$

that can be seen as the N position and momentum operators, respectively. The canonical commutation relations can be captured as $[\hat{X}_l, \hat{X}_m] = i\Omega_{l,m}$ for $l, m = 1, \dots, N$, giving rise to the symplectic form

$$\Omega = \begin{pmatrix} 0 & \mathbb{1} \\ -\mathbb{1} & 0 \end{pmatrix}. \quad (\text{B2})$$

Given a density matrix $\hat{\gamma}$, we define the *vector of mean values* $\bar{\mathbf{X}} := \langle \hat{\mathbf{X}} \rangle_{\hat{\gamma}} = \text{Tr}(\hat{\gamma}\hat{\mathbf{X}})$: these are the first moments of the set of quadrature operators \hat{X} corresponding to the quantum state. The second moments can be collected in the *covariance matrix* with entries

$$\Gamma_{i,j} := \langle \hat{X}_i \hat{X}_j + \hat{X}_j \hat{X}_i \rangle_{\hat{\gamma}} - 2\langle \hat{X}_i \rangle_{\hat{\gamma}} \langle \hat{X}_j \rangle_{\hat{\gamma}}. \quad (\text{B3})$$

For a single mode, namely $N = 1$, the diagonal elements of Γ are simply the two variances $\Gamma_{1,1} = 2(\Delta\hat{q}_1)_{\hat{\gamma}}^2$ and $\Gamma_{2,2} = 2(\Delta\hat{p}_1)_{\hat{\gamma}}^2$. The single constraint for the real-valued matrix to correspond to a physical state is given by the *Heisenberg uncertainty relation*, which can be concisely written as a semi-definite constraint as

$$\Gamma + i\Omega \geq 0. \quad (\text{B4})$$

Of key importance in this work are bosonic Gaussian states. A general Gaussian state of N modes is fully described by the vector of mean values and the covariance matrix corresponding to all modes. Gaussian states are ubiquitous in physical systems. For example, thermal states $\hat{\gamma}_\beta[\hat{H}] = \exp(-\beta\hat{H})/\text{Tr}(\exp(-\beta\hat{H}))$ are Gaussian whenever the Hamiltonian \hat{H} is quadratic in the field operators, which again is a very common situation in many physical settings. In condensed matter physics and in quantum field theory, such a situation would be referred to as being *non-interacting*. Generally, every Gaussian state with full support

[142] can be written in a form resembling thermal states of quadratic Hamiltonians, namely there exists a H such that

$$\hat{\gamma}[H] = \frac{1}{Z} \exp \left(-\frac{1}{2} (\hat{\mathbf{X}} - \bar{\mathbf{X}})^T H (\hat{\mathbf{X}} - \bar{\mathbf{X}}) \right), \quad H = \begin{pmatrix} H_{qq} & H_{qp} \\ H_{pq} & H_{pp} \end{pmatrix}, \quad (\text{B5})$$

where H is a real positive semi-definite $2N \times 2N$ matrix written in block form for clarity and

$$Z = \text{Tr} \left[\exp \left(-\frac{1}{2} (\hat{\mathbf{X}} - \bar{\mathbf{X}})^T H (\hat{\mathbf{X}} - \bar{\mathbf{X}}) \right) \right] = \sqrt{\det((\Gamma + i\Omega)/2)} \quad (\text{B6})$$

is the normalization, which can be fully determined by the covariance matrix of the Gaussian state Γ . The relation between Γ and the matrix H appearing in the expression above is

$$H = 2i\Omega \operatorname{arccoth}(i\Gamma\Omega), \quad \Gamma = i\Omega \coth(i\Omega H/2). \quad (\text{B7})$$

In turn, any generic quadratic (Hermitian) Hamiltonian can be written similarly as above, i.e., with H being a real positive-semi-definite $2N \times 2N$ matrix. Thus, as a difference with respect to the above matrix appearing in the expression for faithful Gaussian states, a generic quadratic Hamiltonian can also contain zero eigenvalues (and need not to be diagonalizable).

The (Gaussian) unitary evolution corresponding to the time-independent quadratic Hamiltonian translates into the symplectic transformation acting on the covariance matrix, given by

$$G(t) = \exp(\Omega H t), \quad (\text{B8})$$

such that the evolved covariance matrix is $\Gamma(t) = G(t)\Gamma(0)G(t)^T$. A similar relation holds for the evolution with time-dependent Hamiltonians, see for example the discussion on the QTP primitives in Sec. C. Thus, in the framework of Gaussian states and operations one can work directly with just the mean vector and the covariance matrix, since they jointly contain all the information that characterizes the Gaussian state. In particular, given a quadratic Hamiltonian $\hat{H} = \sum_{k,l} H_{k,l} \hat{X}_k \hat{X}_l$, the average energy of a state $\hat{\gamma}$ can be easily computed as

$$E_\rho = \text{Tr}(\hat{H}\hat{\gamma}) = \sum_{k,l} H_{k,l} \text{Tr}(\hat{\gamma} \hat{X}_k \hat{X}_l) = \sum_{k,l} H_{k,l} \left(\frac{1}{2} \Gamma_{k,l} + \langle X_l \rangle_\rho \langle X_k \rangle_\rho \right). \quad (\text{B9})$$

The covariance matrix and the Hamiltonian matrix can be put into normal form by symplectic transformations, which read

$$\Gamma = M \left(\bigoplus_k \gamma_k \mathbb{1}_2 \right) M^T, \quad H = M \left(\bigoplus_k \omega_k \mathbb{1}_2 \right) M^T, \quad (\text{B10})$$

where M is a symplectic matrix and the $\{\gamma_k\}$ (respectively $\{\omega_k\}$) are the *symplectic eigenvalues* and are the eigenvalues of $|i\Omega\Gamma|$ (respectively $|i\Omega H|$). Clearly, the symplectic eigenvalues of Γ and H are related to each other in the same relation as Eq. (B7), e.g., for a thermal covariance matrix at inverse temperature $\beta^{-1} = k_B T$, we have

$$d_k = \coth(\beta\omega_k/2), \quad (\text{B11})$$

which is the usual relation between the normal mode frequencies ω_k of a harmonic oscillator Hamiltonian and the normal covariances of its thermal state. Note that by identifying $\gamma_k = 2\langle n_k \rangle + 1$, this agrees with the Bose-Einstein number distribution formula

$$\langle \hat{n}_k \rangle = e^{-\beta\omega_k} / (1 - e^{-\beta\omega_k}). \quad (\text{B12})$$

The von Neumann entropy of a quantum state ρ can be also directly computed from its covariance matrix Γ , and in particular just from its symplectic eigenvalues (as is true for every unitarily invariant quantity). In fact, recall the definition

$$S(\hat{\gamma}) := -\text{Tr}(\hat{\gamma} \log \hat{\gamma}), \quad (\text{B13})$$

and that it is invariant under unitaries. By considering the density matrix expressed as in Eq. (B5), we notice that we can first apply local unitaries (namely displacement operators) so to put $\bar{\mathbf{X}}_\rho = 0$. Then, by taking the matrix logarithm, we find the expression for the von Neumann entropy of a (faithful) Gaussian state to be

$$S(\hat{\gamma}[H]) = \frac{1}{2} \log \det \left(\frac{\Gamma + i\Omega}{2} \right) + \frac{1}{2} \sum_{k,l} \operatorname{arccoth}(i\Gamma\Omega)_{k,l} (i\Omega\Gamma)_{l,k}, \quad (\text{B14})$$

and in terms the symplectic eigenvalues of the covariance matrix it reads

$$S(\hat{\gamma}[H]) = \sum_{k=1}^N \left[\left(\frac{d_k + 1}{2} \right) \log \left(\frac{d_k + 1}{2} \right) - \left(\frac{d_k - 1}{2} \right) \log \left(\frac{d_k - 1}{2} \right) \right]. \quad (\text{B15})$$

For a thermal covariance matrix with $\beta > 0$, we can rewrite this expression in terms of normal mode frequencies:

$$S(\beta) = \sum_k \left[\frac{\beta \omega_k e^{-\beta \omega_k}}{1 - e^{-\beta \omega_k}} - \log(1 - e^{-\beta \omega_k}) \right]. \quad (\text{B16})$$

Recall that $F(\cdot) = \text{Tr}(H \cdot) - S(\cdot)/\beta$ is the *non-equilibrium free energy* of the state relative to its surrounding ambient temperature β^{-1} and its corresponding Hamiltonian H . In the case of thermal states, the free energy is given as

$$F(\beta) = \text{Tr}(\hat{H} \hat{\gamma}_\beta[\hat{H}]) - \beta^{-1} S(\beta) = \beta^{-1} \sum_k \log(1 - e^{-\beta \omega_k}). \quad (\text{B17})$$

Given two faithful Gaussian states $\hat{\gamma}$ and $\hat{\sigma}$, each on N bosonic modes, described by covariance matrices Γ and Υ respectively, it is also easy to compute their relative entropy according to

$$S(\hat{\gamma} \parallel \hat{\sigma}) = -S(\hat{\gamma}) - \text{Tr}(\hat{\gamma} \log \hat{\sigma}) = \text{Tr}(\hat{\gamma} (\log \hat{\gamma} - \log \hat{\sigma})), \quad (\text{B18})$$

essentially because again it is easy to compute the logarithm of such states. Since the first term is nothing but the negative von Neumann entropy that can be computed according to Eq. (B15), we can see this by just considering the second term. By considering the form (B5) of faithful Gaussian states, we obtain

$$\text{Tr}(\hat{\gamma} \log \hat{\sigma}) = -\log Z_\sigma + \text{Tr} \left[\hat{\gamma} \left(-\frac{1}{2} (\hat{\mathbf{X}} - \bar{\mathbf{X}}_\sigma)^T H_\sigma (\hat{\mathbf{X}} - \bar{\mathbf{X}}_\sigma) \right) \right], \quad (\text{B19})$$

where we have simply used the fact that logarithm and exponential of a matrix are inverse functions. We can also simplify further the above expression and write it just in terms of (combinations of) covariance matrices elements as

$$-\text{Tr}(\hat{\gamma} \log \hat{\sigma}) = \frac{1}{2} \log \det((\Upsilon + i\Omega)/2) + \frac{1}{4} \sum_{k,l} \Upsilon_{k,l} (H_\sigma)_{k,l} + \frac{1}{2} (\bar{\mathbf{X}}_\sigma - \bar{\mathbf{X}}_\rho)^T H_\sigma (\bar{\mathbf{X}}_\sigma - \bar{\mathbf{X}}_\rho), \quad (\text{B20})$$

which leads to

$$S(\hat{\gamma} \parallel \hat{\sigma}) = \frac{1}{2} \left[\log \left(\frac{\det((\Upsilon + i\Omega)/2)}{\det((\Gamma + i\Omega)/2)} \right) + \frac{1}{2} \sum_{k,l} \Gamma_{k,l} (H_\sigma - H_\rho)_{k,l} + (\bar{\mathbf{X}}_\sigma - \bar{\mathbf{X}}_\rho)^T H_\sigma (\bar{\mathbf{X}}_\sigma - \bar{\mathbf{X}}_\rho) \right], \quad (\text{B21})$$

where we also used the expression (B14) for the von Neumann entropy. Note once more that the matrices H_ρ and H_σ can be also directly obtained from Γ and Υ respectively through Eq. (B7). Another useful expression can be written down, containing explicitly the symplectic eigenvalues of the two covariance matrices. For that we notice that the logarithm of the partition function Z_σ can be also expressed as

$$\log Z_\sigma = \frac{1}{2} \sum_k \log((v_k^2 - 1)/2), \quad (\text{B22})$$

where $\{v_k\}$ are the symplectic eigenvalues of Υ . Thus, we can write

$$S(\hat{\gamma} \parallel \hat{\sigma}) = -S(\hat{\gamma}) + \sum_k \log((v_k^2 - 1)/2) + \frac{1}{4} \sum_{k,l} \Gamma_{k,l} (H_\sigma)_{k,l} + \frac{1}{2} (\bar{\mathbf{X}}_\sigma - \bar{\mathbf{X}}_\rho)^T H_\sigma (\bar{\mathbf{X}}_\sigma - \bar{\mathbf{X}}_\rho), \quad (\text{B23})$$

where we can also use the expression (B15) for $S(\rho)$. Finally, note that if σ is a true thermal state of a Hamiltonian H at inverse temperature $\beta > 0$, then for any state ρ , we have

$$S(\hat{\gamma} \parallel \hat{\sigma}) = \beta(F(\hat{\gamma}) - F(\hat{\sigma})). \quad (\text{B24})$$

Appendix C: Details of the QTP simulations

1. Lattice discretization scheme

Here we define a lattice version of the TLL Hamiltonian, obtained by discretising the interval $[-L, L]$ into N pixels, each of size $\Delta z = 2L/N$ [143, 144]. This is particularly important to make numerical calculations, especially for the case of non-homogeneous external potentials. Fixing N , for $i = 1, \dots, N+1$ the coordinates of the discretization lattice read $z_i = -L + 2L \frac{i-1}{N}$, and we define discretization pixels which are the closed intervals $p_i = [z_i, z_{i+1}]$ for $i = 1, \dots, N$. We then introduce the discretized version of density and phase operators as the integration of the field operators via

$$\hat{\varphi}_i^{(N)} = \frac{1}{\Delta z} \int_{p_i} dz \hat{\varphi}(z), \quad \delta \hat{\varrho}_i^{(N)} = \frac{1}{\Delta z} \int_{p_i} dz \delta \hat{\varrho}(z), \quad (C1)$$

with $|p_i| = \Delta z = 2L/N$. These discretized operators yields a vector of canonical coordinates

$$\hat{\mathbf{X}} = \left(\delta \hat{\varrho}_1^{(N)} \dots \delta \hat{\varrho}_N^{(N)}, \hat{\varphi}_1^{(N)}, \dots, \hat{\varphi}_N^{(N)} \right)^T, \quad (C2)$$

satisfying (re-scaled) bosonic canonical commutation relations

$$[\hat{X}_j, \hat{X}_k] = i\Omega_{j,k}/\Delta z, \quad (C3)$$

where Ω is defined in Eq. (B2). As explained in Ref. [36], in the continuum limit $N \rightarrow \infty$, the right-hand side will yield a Dirac delta because $1/\Delta z$.

To discretise the model, we follow Ref. [143] and consider the geometric mean

$$\eta_i = \sqrt{\rho_0(z_i)\rho_0(z_{i+1})} \quad (C4)$$

for $i = 1, \dots, N$. The discretization of the effective model will be a quadratic operator in the discretised modes $\hat{\varphi}_i^{(N)}$ and $\delta \hat{\varrho}_i^{(N)}$. At the lowest order approximation, one obtains

$$\hat{H} \approx \Delta z \sum_{i=1}^{N-1} \frac{\hbar^2 \eta_i}{2m} \left[\frac{\hat{\varphi}_i^{(N)} - \hat{\varphi}_{i+1}^{(N)}}{\Delta z} \right]^2 + \Delta z \sum_{i=1}^N \frac{g(z_i)}{2} \left(\delta \hat{\varrho}_i^{(N)} \right)^2 =: \hat{H}_N. \quad (C5)$$

Note that so far in the main text, we have suppressed for simplicity the possible spatial dependence of the coupling constant g , which is true for a homogeneous quasi-condensate and in general has little influence. In general g depends on the GP profile,

$$g(z) = \hbar \omega_{\perp} a_s (2 + 3a_s \rho_0(z)) / (1 + 2a_s \rho_0(z))^{3/2} \quad (C6)$$

where ω_{\perp} is the radial trapping frequency and a_s is the scattering length [25, 145]. This dependency on the spatial coordinate z has been included in our numerical simulations. From this, we obtain the matrix representation of the above Hamiltonian

$$H = \frac{1}{2} \cdot \hat{\mathbf{X}}^{\top} (H_{\rho\rho}[g, \Delta z] \oplus H_{\phi\phi}[\rho_0, \Delta z]) \hat{\mathbf{X}}, \quad (C7)$$

$$H_{\rho\rho}[\Delta z] = \Delta z \cdot \text{diag}(g(z_1), g(z_2), \dots, g(z_{N_c})) , \quad (C8)$$

$$H_{\phi\phi}[\rho_0, \Delta z] = \frac{\hbar^2}{m\Delta z} \begin{pmatrix} \eta_1 & -\eta_1 & & \\ -\eta_1 & \eta_1 + \eta_2 & -\eta_2 & \\ & & \ddots & \\ & & -\eta_{N-2} & \eta_{N-2} + \eta_{N-1} & -\eta_{N-1} \\ & & & -\eta_{N-1} & \eta_{N-1} \end{pmatrix} + 2\hbar \text{diag}(J(z_1)\eta(z_1), \dots, J(z_N)\eta(z_N)), \quad (C9)$$

where we have used the functional notation $H_{\phi\phi}[\rho_0, \Delta z]$ to emphasize that these couplings depend on the mean-field density profile and the size of the pixels. We additionally added a small term $\propto J$ which is meant to regularize the zero-mode. This way, all computations are made with fully-supported Gaussian states so that numerical instabilities do not occur. Physically, it can be interpreted as adding a small mass term of the type $\hat{H}_J = \hbar J \int dz \rho_0(z) \hat{\varphi}(z)^2$ and we have checked that, as long as the coupling is chosen to be around $J \approx 0.01$ the dynamics is not affected in the times scales of 300 ms that we have in mind. See also Sec. C 3 below for a more extended discussion.

Starting from a set of canonical coordinates $\hat{\mathbf{X}}$, then for a symplectic $M \in \mathbb{R}^{2N \times 2N}$ i.e. fulfilling

$$M \Omega M^T = \Omega, \quad (\text{C10})$$

we have that $\hat{\mathbf{r}} = M\hat{\mathbf{X}}$ will again denote a vector of canonically commuting operators if which can be seen by explicitly checking that \hat{r} again fulfills $[\hat{r}_j, \hat{r}_k] = i\Omega_{j,k}/\Delta z$.

We can then diagonalize our Hamiltonian as follows: First, we use the symplectic matrix

$$M_1 = \begin{pmatrix} \sqrt{H_{\rho\rho}^{-1}} & 0 \\ 0 & \sqrt{H_{\rho\rho}} \end{pmatrix} = M_1^T, \quad (\text{C11})$$

since $H_{\rho\rho}$ is diagonal. Then, we have

$$M_1^T H M_1 = \mathbb{1}_N \oplus \left(\sqrt{H_{\rho\rho}^{-1}} H_{\phi\phi} \sqrt{H_{\rho\rho}} \right) =: \mathbb{1}_N \oplus \tilde{H}_{\phi\phi}, \quad (\text{C12})$$

where $\tilde{H}_{\phi\phi}$ is the matrix of the phase couplings in the new coordinates, which is real and symmetric, and therefore can be diagonalized by an orthogonal transformation O with $\tilde{H}_{\phi\phi} = O\Sigma O^T$. Here, Σ is diagonal and we assume that all zero eigenvalues are sorted to the first $N^0 \geq 0$ positions, i.e., $\Sigma = 0_{N^0} \oplus \tilde{\Sigma}$ with $\tilde{\Sigma} > 0$ diagonal and we define the eigenfrequencies ω via $\tilde{\Sigma}^{1/2} = \text{diag}(\omega_{N^0+1}, \dots, \omega_N)$. With the diagonal matrix $\Sigma_{\phi} = \mathbb{1}_{N^0} \oplus \tilde{\Sigma}$ and the transformation

$$M_2 = \begin{pmatrix} O\Sigma_{\phi}^{1/4} & 0 \\ 0 & O\Sigma_{\phi}^{-1/4} \end{pmatrix} \quad (\text{C13})$$

we obtain

$$M_2^T M_1^T H M_1 M_2 = (\mathbb{1}_{N^0} \oplus \tilde{\Sigma}^{1/2}) \oplus (0_{N^0} \oplus \tilde{\Sigma}^{1/2}). \quad (\text{C14})$$

That is, in the canonical coordinates $\hat{\mathbf{r}} = (\hat{Q}_1, \dots, \hat{Q}_N, \hat{P}_1, \dots, \hat{P}_N) = \sqrt{\Delta z} (M_1 M_2)^{-1} \hat{\mathbf{X}}$ we have that the Hamiltonian in Eq. (C7) takes the form

$$\hat{H} = \frac{1}{2} \sum_{j=1}^{N^0} \hat{Q}_j^2 + \frac{1}{2} \sum_{j=N^0+1}^N \omega_j (\hat{P}_j^2 + \hat{Q}_j^2). \quad (\text{C15})$$

Finally, we can define creation/annihilation operators $(\hat{c}_j^\dagger, \hat{c}_j)$ for each normal mode from the relation

$$\hat{P}_j^2 + \hat{Q}_j^2 = 2\hat{c}_j^\dagger \hat{c}_j + \mathbb{1}. \quad (\text{C16})$$

Note that the new coordinates satisfy true canonical commutation relations $[\hat{Q}_k, \hat{P}_l] = i\delta_{k,l}$ and consequently we also have

$$[\hat{c}_k, \hat{c}_l^\dagger] = \delta_{k,l}, \quad (\text{C17})$$

for all k, l . However, our original discretized field operators satisfy re-scaled commutation relations. This means that the symplectic matrix corresponding to the evolution with \hat{H}_N in the original coordinates is given by Eq. (B8), where the symplectic form is re-scaled, namely $\Omega \mapsto (\Delta z)^{-1}\Omega$.

Thermal states of the above Hamiltonian have covariance matrices of the form $\Gamma = \Gamma_{\rho\rho} \oplus \Gamma_{\phi\phi}$, and can be also explicitly computed from the normal modes and the corresponding symplectic transformation, namely Eqns. (B10) and (B11). The expression is somewhat complicated for the general case, but for the special case of homogeneous systems (which we will be interested in) $H_{\rho\rho} = \kappa \mathbb{1}$ with $\kappa := \Delta z g$, we get

$$\Gamma_{\beta} = \frac{1}{\sqrt{\kappa}} H_{\phi\phi}^{1/2} \oplus \sqrt{\kappa} H_{\phi\phi}^{-1/2} + \frac{1}{\sqrt{\kappa}} (H_{\phi\phi}^{1/2} T) \oplus \sqrt{\kappa} (H_{\phi\phi}^{-1/2} T), \quad (\text{C18})$$

where

$$T := 2 \left(\exp(2\beta \sqrt{\kappa} H_{\phi\phi}^{1/2}) - \mathbb{1} \right)^{-1}. \quad (\text{C19})$$

As discussed in the previous Sec. B, diagonalizing the Hamiltonian in terms of normal modes, the covariance matrix becomes also diagonal with symplectic eigenvalues given by Eq. (B11). From these symplectic eigenvalues one can also write down the (von Neumann) entropy and the free energy as in Eqs. (B16, B17).

2. Details of merging and splitting

In this section, we provide an extended discussion of the merge/split primitive. This is a three-step process, involving two condensates A and B with lengths L_A and L_B and densities ρ_0^A and ρ_0^B , and consisting in

- (a) merging the two initially independent condensates during a time t_{merge} ,
- (b) letting them evolve with the fully merged Hamiltonian for a time t_{evolve} , and
- (c) splitting the joint condensate back into two parts A and B , with the same lengths as the initials, during a time t_{split} .

a. Merging

For the merging process, we encounter a time dependent Hamiltonian $\hat{H}_{A-B}(t)$ such that

$$\hat{H}_{A-B}(0) = \hat{H}_{NA}[\rho_0^A] + \hat{H}_{NB}[\rho_0^B], \quad (\text{C20})$$

where our Hamiltonians are given by the lattice model in Eq. (C5) and (keeping constant the small distance cutoff Δz) are functionals of the initial mean-field density profiles of the two condensates. Note that since we want to couple the two systems, we want them to have a consistent momentum cutoff $(\Delta z)^A = (\Delta z)^B = \Delta z$ (so that waves traveling across quasi-condensates with same atom density in the simulation should not change in speed due to the different discretization), and consequently their number of pixels will be in the same proportion as their lengths, i.e.,

$$N^A = L_A \Delta z = N^B L_B / L_A. \quad (\text{C21})$$

The coupling matrix of the uncoupled Hamiltonian in Eq. (C20) is by

$$H_{\rho\rho, A|B} = H_{\rho\rho, A} \oplus H_{\rho\rho, B}, \quad H_{\phi\phi, A|B} = H_{\phi\phi, A} \oplus H_{\phi\phi, B}. \quad (\text{C22})$$

To merge the condensates, an interaction Hamiltonian is switched on, so that the joint Hamiltonian as in Eq. (C7) has a matrix representation given by

$$H_{\rho\rho, AB} = H_{\rho\rho, A} \oplus H_{\rho\rho, B}, \quad H_{\phi\phi, AB} = H_{\phi\phi, A} \oplus H_{\phi\phi, B} + \frac{t}{t_{\text{merge}}} H_{\text{int}}, \quad (\text{C23})$$

where the interaction matrix is given by

$$(H_{\text{int}})_{i,j} = \frac{\hbar^2}{2m\Delta z} \eta_{NA} (\delta_{NA,i} \delta_{NA,j} + \delta_{NA+1,i} \delta_{NA+1,j} - \delta_{NA,i} \delta_{NA+1,j} - \delta_{NA+1,i} \delta_{NA,j}). \quad (\text{C24})$$

with $\eta_{NA} := \sqrt{\rho^A(N^A) \cdot \rho^B(1)}$. Note that this interaction contains also the local terms in the boundary region $[N^A, N^A + 1]$. We hence see that the couplings during the merging are given by

$$H_{A-B}(t) = (1 - \frac{t}{t_{\text{merge}}}) H_{A|B} + \frac{t}{t_{\text{merge}}} H_{AB}. \quad (\text{C25})$$

For the numerical implementation, we also discretize the time evolution so that we divide the $[0, t_{\text{merge}}]$ time interval into N_t steps of duration $\Delta t = t_{\text{merge}}/N_t$. Then, the symplectic evolution matrix reads

$$G_{\text{merge}}(t_{\text{merge}}) = \prod_{j=1}^{N_t} \exp(\Omega H_{A-B}(t_j)/\Delta z), \quad (\text{C26})$$

where $H_{A-B}(t) = H_{NA} + H_{NB} + \frac{j}{N_t} H_{\text{int}}$. Examples of eigenmodes for the time-dependent Hamiltonian are plotted in Figs. 7, 8 for a homogeneous GP profile with or without a trapeze-like buffer region. We find that mode functions that are odd in z hybridize via a jump which gets smoothened during the merging while, mode functions which are even in z get glued

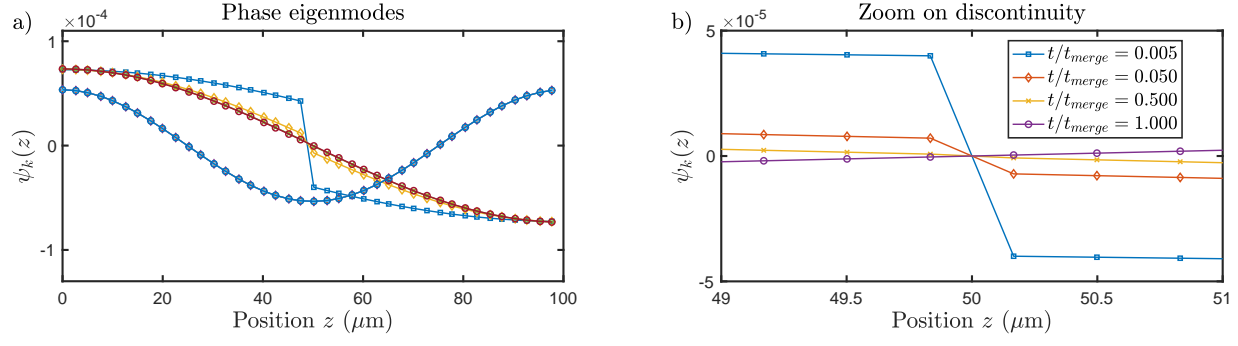


FIG. 7. Snapshots of the phase and density eigenmode functions for the first and second lowest modes, taken at different Trotter steps t/t_{merge} during merging for a fully homogeneous profile.

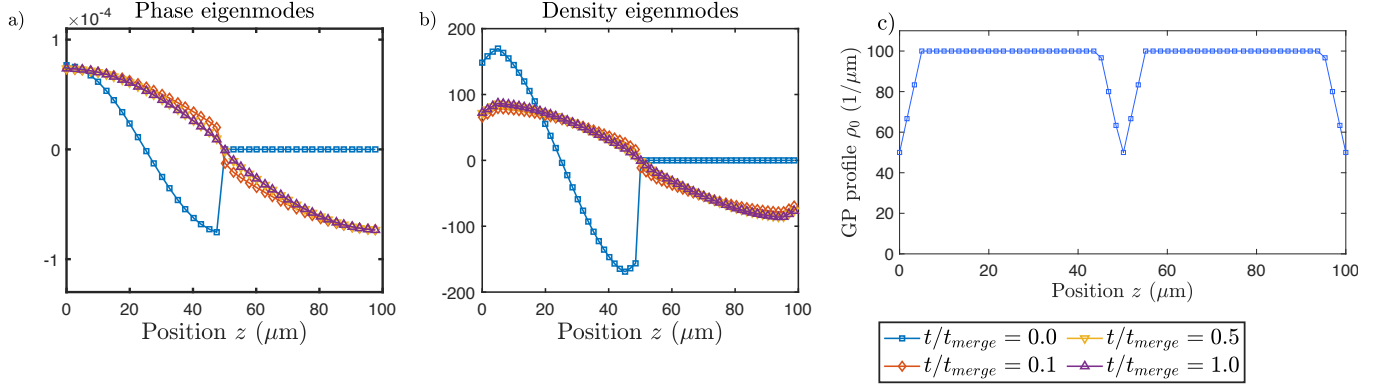


FIG. 8. Snapshots of the phase and density eigenmode functions for the two lowest lying modes taken at different Trotter steps t/t_{merge} during merging for a homogeneous profile with a trapeze-like buffer region. (a) The odd modes during the coupling have a discontinuity of varying strength which diminishes as the merging proceeds. In contrast there is little influence of the merging on the even modes as they can be obtained by connecting the odd modes of the individual uncoupled systems. (b) The discontinuity is sharp, changing suddenly from one pixel to another.

automatically. We see also that all modes have a local extremum at the boundary which means we have Neumann boundary conditions.

In the main text we have shown the results for a model of the quasi-condensates where the GP profile falls off smoothly from its peak value in the bulk to a lower value on the edges. In principle, it is possible to consider the effective model to be constant everywhere, whereas the edge of the condensate (where excitations get reflected) can be modelled by the boundary conditions. However, this abstraction turns out to be too simplistic. Fig. 9 provides a demonstration of what occurs in such a scenario. Since the process is simulated via the merging of the boundary conditions of the two condensates, in particular occurring at a *single* pixel, it is hence *independent of the momentum cut-off*. As a result, momenta at all scales are populated, however, this does not faithfully capture the physics of the continuum model, since the dispersion relation is not linear. In order to avoid this, it is therefore necessary for the model to resolve details of the coupling zone.

b. Idle evolution

In-between merging and splitting, one can allow some idle evolution time t_{evolve} in which the joint system evolves with the fully coupled Hamiltonian. This can be applied with a single symplectic matrix, since the Hamiltonian is time-independent. Wavepackets injected during the previous merging process will travel ballistically through the entire joint system (as long as we taken care to remain in the regime where high-momentum modes are negligible and the linear dispersive relation holds).

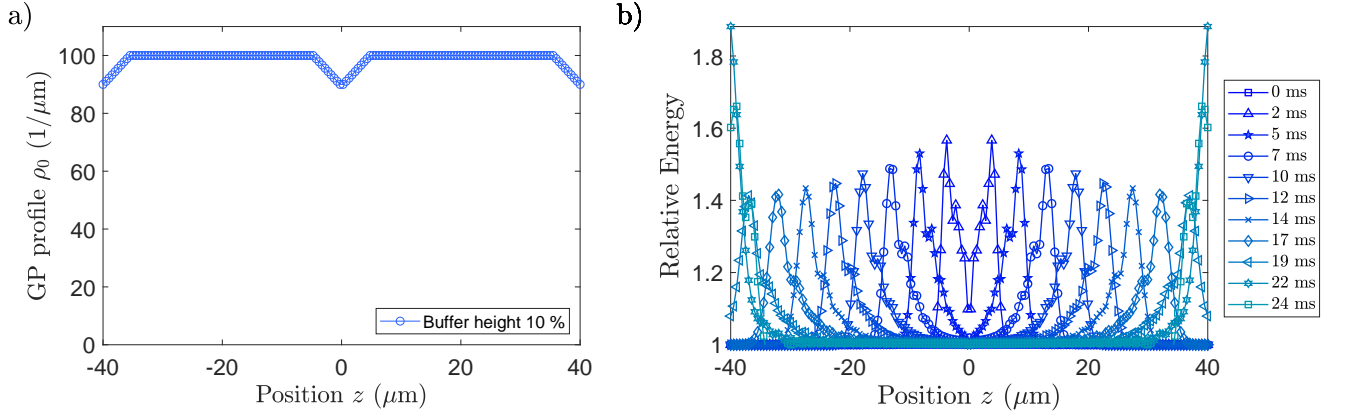


FIG. 9. **The presence of high momentum modes in a merging model with non-extensive buffer region between condensates.** *a)* We show the merging scenario similar to the figure in the main text with the difference that the coupling zone is much smaller and ends abruptly at 90% of the peak value. *b)* We now find that the transport of the excitations is *dispersive* which can be seen by the peaks of wave-packets falling down as their propagation. As the dynamics is modeled to be unitary and the Hamiltonian doesn't change in the bulk this means that the energy the wave-packets carry stays constant while being broadened. In lattice theories, dispersion can be proven analytically if short wavelengths are present in the state [146].

c. Splitting

Finally, we implement the splitting procedure by a time-dependent Hamiltonian reversing the linear interpolation that was discussed for merging. In the numerical simulation the covariance matrix of the A and B quasi-condensates after merging, idle evolution and splitting would have the form

$$\Gamma_{A-B}(t_{\text{tot}}) = G_{\text{split}} G_{\text{evolve}} G_{\text{merge}} \Gamma_{A-B}(0) G_{\text{merge}}^T G_{\text{evolve}}^T G_{\text{split}}^T. \quad (\text{C27})$$

For reasons discussed in the main text, whenever we simulate the Otto cycle, we neglect the correlations between the two parts of the split condensate at the end of the process. In other words, we project the final covariance matrix into the direct sum of the two local covariance matrices for systems A and B , i.e., at the end of the full protocol, $t = t_{\text{tot}} = t_{\text{merge}} + t_{\text{evolve}} + t_{\text{split}}$, by setting

$$\Gamma_{A-B}^{\text{fin}}(t_{\text{tot}}) = \Gamma_A(t_{\text{tot}}) \oplus \Gamma_B(t_{\text{tot}}), \quad (\text{C28})$$

where $\Gamma_A(t_{\text{tot}})$ is the submatrix of $\Gamma_{A-B}(t_{\text{tot}})$ corresponding to the subsystem A and $\Gamma_B(t_{\text{tot}})$ corresponds to B .

d. Energy density injected during merging QTP

Given the quadratic Hamiltonian over time $\hat{H}_{A-B}(t)$ we would like to study also the spatial distribution of the energy. In the discretized models, it is natural to study the energy per pixel z , namely

$$E(z, t) = E_z(t) \Delta z = \frac{1}{2} (H_{A-B}(t) \Gamma_{A-B}(t))_{z,z} \Delta z, \quad (\text{C29})$$

where the notation $(\cdot)_{z,z}$ refers to the diagonal matrix element at pixel z . Note that if Δz is constant, this amounts to just computing the quantities $E_z(t)$. Plotting E_z over pixel positions is then a way of visualizing which regions in space have more energy than others. Doing this over varying times can show us how energy flows over time from one part of the system to the other. For example, in Fig. 9, we observe that merging the two systems amounts to inserting energy at their boundary continuously over the merging time (or in discrete bits at each Trotter time step). This energy then flows through the system at speed of sound velocity (which is $c = \sqrt{g\rho_0/m} \propto \sqrt{\rho_0}$), reaching the external boundaries and then bouncing back toward the center. Thus, in particular, if the ratio between the coupling time t_{merge} and the length of a system (say A) is chosen such that

$$c = L_A/t_{\text{merge}}, \quad (\text{C30})$$

then the energy perturbation precisely reaches the external boundary of system A . Similarly for system B . Clearly, then, when the two lengths L_A and L_B are not equal the energy flow cannot be synchronized so that the perturbation wave bounces back to the interface from both external walls at the same time. During the idle evolution time t_{evolve} no additional energy is injected, but the energy flow continues. Finally, during the splitting process some energy is taken away from the system, again continuously over the splitting time and at the interface between the two parts. However, the total amount of energy taken back during the splitting is in general lower than the one inserted during merging. Hence, the total energy inserted during the entire protocol is always non-negative, and the amount is smaller given a protocol with longer time.

As a last comment, we note that the fact that our simulations use discretized space and time also implies that, besides the fact that energy is injected and ejected at the interface in discretized bits over t_{merge} and t_{split} , the energy flow also takes places in pixels over time steps. In particular, all of this imposes us once more for consistency to make sure that the two coupled systems have the same small distance cut-off Δz , which also ensures that the lengths in the two systems are in the same ratios between their number of pixels. This issue becomes particularly important when a compression/expansion QTP takes place before merging since in that case, as we are going to discuss in detail in the next subsection, the cut-off Δz changes in time.

3. Regularization of the zero-mode: Phase locking via excitation tunneling

Here we discuss more in detail the additional complications arising from the zero-modes of the TLL model and how to regularize them, in order to avoid instabilities during coupling. The mode expansion of Eq. (2) reads

$$\hat{H}_{\text{TLL}}[\rho_0] = \sum_{k>0} \hbar \frac{\omega_k}{2} (\hat{\varphi}_k^2 + \delta \hat{\varrho}_k^2) + \frac{g}{2} \delta \hat{\varrho}_{\text{ZM}}^2, \quad (\text{C31})$$

where ω_k are the eigen-frequencies of the phase and momentum eigenmodes $\hat{\varphi}_k, \delta \hat{\varrho}_k$ and there is a special mode, called the zero-mode, $\delta \hat{\varrho}_{\text{ZM}} \propto \int dz \delta \hat{\varrho}(z)$ which is different from $k > 0$ eigenmodes as the canonically conjugate quantity $\hat{\varphi}_{\text{ZM}} \propto \int dz \hat{\varphi}(z)$ does not appear in the Hamiltonian, i.e., it does not cost energy. The zero mode has the interpretation of total momentum frame of the excitations [21–24].

This mode expansion can be found in the continuum limit by solving the set of partial differential equation associated to the Heisenberg equations of motion, namely

$$\begin{cases} \partial_t \delta \varrho(z, t) = \frac{\hbar}{m} \partial_z (\rho_0(z) \partial_z \varphi(z, t)) \\ \partial_t \varphi(z, t) = -\frac{g}{\hbar} \delta \varrho(z, t) \end{cases} \Rightarrow \partial_t^2 \varphi_k(z, t) = -\frac{g}{m} \partial_z (\rho_0(z) \partial_z \varphi_k(z)), \quad (\text{C32})$$

and, as usual, for the $k > 0$ modes we can look for solutions of the type $\varphi_k(z, t) = \varphi_k(z) e^{i\omega_k t}$, so that Eq. (C32) becomes a Sturm-Liouville problem

$$\omega_k^2 \varphi_k(z) = -\frac{g}{m} \partial_z (\rho_0(z) \partial_z \varphi_k(z)), \quad (\text{C33})$$

and similarly for $\delta \varrho(z, t)$. We can then find solutions which form an orthonormal basis with respect to the scalar product

$$\langle f, g \rangle := \int dz f(z) g(z), \quad (\text{C34})$$

i.e., we have $\langle \varphi_k(z), \varphi_l(z) \rangle = \langle \delta \varrho_k(z), \delta \varrho_l(z) \rangle = \delta_{k,l}$, where $\delta_{k,l}$ is the Kronecker delta.

However, besides those one can also find a solution with $\omega_k = 0$, which gives rise to the zero mode with quadrature operators denoted by $(\delta \hat{\varrho}_{\text{ZM}}$ and $\hat{\varphi}_{\text{ZM}}$). These are necessary for the set of eigenmode functions to be complete and we can expand the field operators as

$$\begin{aligned} \delta \hat{\varrho}(z, t) &= \delta \hat{\varrho}_{\text{ZM}} + \sum_{k>0} \sqrt{\frac{\hbar \omega_k}{g}} \delta \varrho_k(z) (e^{i\omega_k t} \hat{a}_k^\dagger + e^{-i\omega_k t} \hat{a}_k), \\ \hat{\varphi}(z, t) &= \hat{\varphi}_{\text{ZM}} - \frac{g}{\hbar} t \delta \hat{\varrho}_{\text{ZM}} - i \sum_{k>0} \sqrt{\frac{g}{\hbar \omega_k}} \varphi_k(z) (e^{i\omega_k t} \hat{a}_k^\dagger - e^{-i\omega_k t} \hat{a}_k), \end{aligned} \quad (\text{C35})$$

and we define eigenmode operators at $t = 0$ (with $k > 0$) from the relations

$$\delta \hat{\varrho}_k = \sqrt{\frac{\hbar \omega_k}{g}} (\hat{a}_k^\dagger + \hat{a}_k), \quad \hat{\varphi}_k = -i \sqrt{\frac{g}{\hbar \omega_k}} (\hat{a}_k^\dagger - \hat{a}_k), \quad (\text{C36})$$

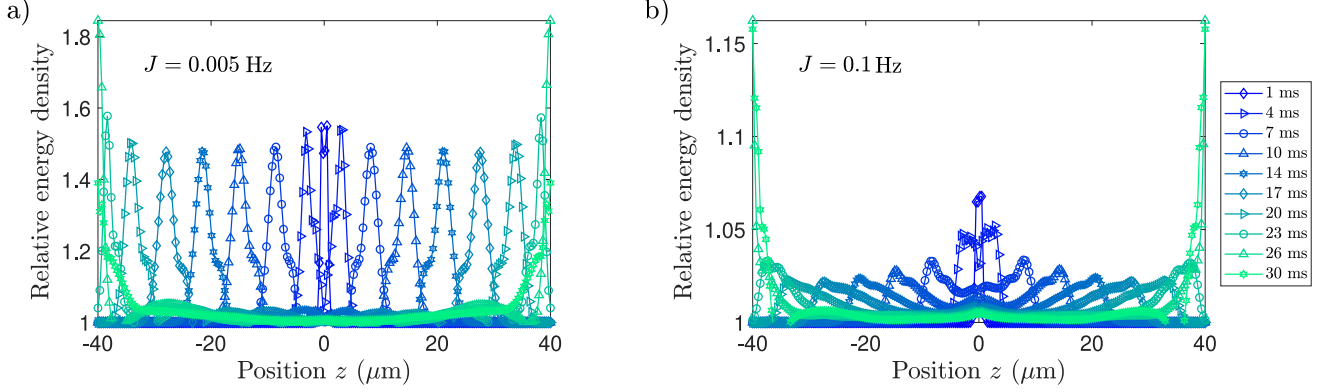


FIG. 10. **Coupling of two quasi-condensates for different initial phase-locking.** Similarly to the main text we consider the phase locking to act with constant strength along each of the condensates and show the influence of other values of J on the outcome of merging. (a): For a low value of $J = 0.005$ Hz there is substantially more excitations compared to the value $J = 0.01$ Hz used for all plots presented in the main text. (b): On the other hand for larger values of phase-locking such as $J = 0.1$ Hz the excitations become suppressed as the phase zero-mode acquires a larger energetic penalty and its initial thermal second moments are smaller. Note, that when increasing the tunnel coupling J further, one expects a non-Gaussian regime due to non-negligible interactions stemming from the full cosine potential [35].

such that they obey canonical commutation relations $[\delta\hat{\varphi}_k, \hat{\varphi}_l] = i\delta_{k,l}$ for all k, l .

Let us now consider the time evolution when coupling two systems governed by the Hamiltonian

$$\hat{H}_{A-B}(t) = \left(1 - \frac{t}{t_{\text{merge}}}\right) \hat{H}_{A|B} + \frac{t}{t_{\text{merge}}} \hat{H}_{AB} \quad (\text{C37})$$

for $t \in [0, t_{\text{merge}}]$. Note that now at each instant t this Hamiltonian has implicitly different boundary conditions at the interface $z = 0$. See also Figs. 7,8 where the eigenmode functions of this time-dependent Hamiltonian are shown at different times t/t_{merge} for the discretized model.

Thus, we see that when two TLLs, each with their own zero-mode, will become coupled the two zero-modes will hybridize to form the joint zero-mode and one mode that costs energy. However, this energy cost will cause the coupled system to have enormous energy if the original phase zero-modes were non-trivially populated, which leads to an unstable time-evolution. In this situation the TLL model is not anymore a good approximation to the Lieb-Liniger model (1) as the density fluctuations may no longer be small.

Nevertheless, one can refine the model considered here to reflect more accurately the corresponding physical process: energy will change continuously, since when we couple the systems by ramping down the separation barrier, there will be an additional term in the Hamiltonian, representing tunneling between the condensates. The density phase expansion of this term will additionally give rise to a term of the type $\hbar J \cos(\Delta\hat{\varphi})$ penalizing phase fluctuations $\Delta\hat{\varphi} = \hat{\varphi}_L - \hat{\varphi}_R$ ranging over the interface. The action of this term is to induce *phase-locking* between the two condensates being merged together, see Refs. [25–28] for experimental discussions and references therein for the theoretical overview. The large coupling expansion of this term motivates the effective model we used in the numerical simulations

$$\hat{H}[\rho_0] = \hat{H}_{\text{TLL}}[\rho_0] + \int dz \hbar J(z) \rho_0(z) \hat{\varphi}(z)^2. \quad (\text{C38})$$

a. Analytical derivation of gapping-out the zero-mode in the homogeneous phase-locking model

In the experiment the phase-locking term will be acting around the interface. For the case of large extension of this coupling (or two side-ways coupled systems [25, 147]) it is instructive to consider $J \equiv \text{const}$ throughout the condensates. In this case additionally taking $\rho_0 \equiv \text{const}$ we can analytically see that this term effectively gaps out the phase zero-mode. One way to see this by noticing that this term amounts to add a (small) “mass” term to Eq. (C32), leading to the modified Sturm-Liouville problem

$$\omega_k^2 \varphi_k(z) = -\frac{g}{m} \partial_z (\rho_0(z) \partial_z \varphi_k(z)) + 2J \rho(z) \varphi_k(z), \quad (\text{C39})$$

which effectively removes the zero-mode.

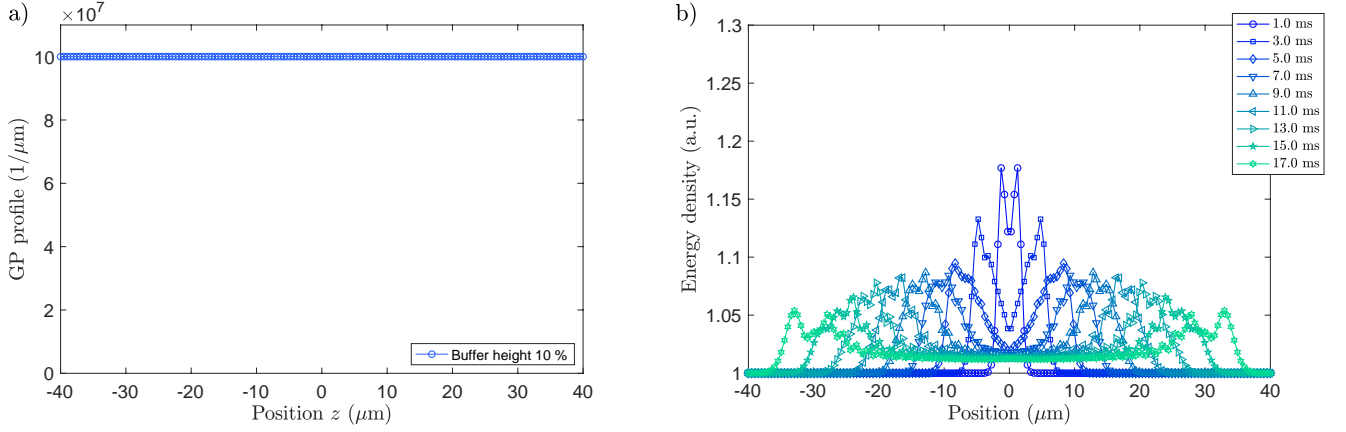


FIG. 11. **Merging of homogeneous systems where the zero mode is artificially removed from the evolution.** Using the eigenmode decomposition for $J = 0$ we set $\delta\hat{\varrho}_0 = \hat{\varphi}_0 = 0$ in the Hamiltonian that governs the merging and compute the initial state using a pseudo-inverse disregarding the zero-mode. We see a behavior, both qualitative and quantitative, similar to merging with a regularization coupling chosen as $J = 0.01$ Hz.

Let us show this specifically in the case when all coupling constants do not vary over the condensate of length L , i.e. $g(z) = g$, $\rho_0(z) = \rho_0$ and $J(z) = J$. The Hamiltonian then reads

$$\hat{H}_J = \int_0^L dz \left[\frac{\hbar^2 \rho_0}{2m} (\partial_z \hat{\varphi}(z))^2 + \frac{g}{2} \delta\hat{\varrho}(z)^2 + \hbar J \rho_0 \hat{\varphi}(z)^2 \right], \quad (\text{C40})$$

and has no zero-modes unless $J = 0$. In this case the eigenfrequencies read as

$$\omega_k = \frac{\pi c k}{L} \quad (\text{C41})$$

with the speed of sound given by $\sqrt{g\rho_0/m}$. To bring the Hamiltonian to the normal form, we define the squeezing constants

$$\alpha_k = \sqrt{\frac{\hbar\omega_k}{g}} + \delta_{k,0} \quad (\text{C42})$$

from which we define for $k > 0$

$$\delta\hat{\varrho}_k = \alpha_k \sqrt{\frac{2}{L}} \int_0^L dz \cos(\pi k z/L) \delta\hat{\varrho}(z) \quad \text{and} \quad \hat{\varphi}_k = \alpha_k^{-1} \sqrt{\frac{2}{L}} \int_0^L dz \cos(\pi k z/L) \hat{\varphi}(z) \quad (\text{C43})$$

and

$$\delta\hat{\varrho}_0 = \sqrt{\frac{1}{2L}} \int_0^L dz \delta\hat{\varrho}(z) \quad \text{and} \quad \hat{\varphi}_0 \equiv \sqrt{\frac{1}{2L}} \int_0^L dz \hat{\varphi}(z) \quad (\text{C44})$$

which stand out by having different normalization constants and would be the zero-mode operators for $J = 0$. Using standard trigonometric integrals we find

$$\int_0^L dz \delta\hat{\varrho}(z)^2 = \sum_{k=0}^{\infty} \alpha_k^2 \delta\hat{\varrho}_k^2 \quad \text{and} \quad \int_0^L dz (\partial_z \hat{\varphi}(z))^2 = \sum_{k>0} \frac{\pi^2 k^2}{L^2 \alpha_k^2} \hat{\varphi}_k^2 \quad \text{and} \quad \int_0^L dz \hat{\varphi}(z)^2 = \sum_{k=0}^{\infty} \alpha_k^{-2} \hat{\varphi}_k^2. \quad (\text{C45})$$

Therefore,

$$\hat{H}_J = \sum_{k=1}^{\infty} \frac{\hbar\omega_k}{2} [\delta\hat{\varrho}_k^2 + \hat{\varphi}_k^2] + \frac{g}{2} \delta\hat{\varrho}_0^2 + \hbar J \rho_0 \sum_{k=1}^{\infty} \alpha_k^{-2} \hat{\varphi}_k^2 + \hbar J \rho_0 \hat{\varphi}_0^2. \quad (\text{C46})$$

Further defining $\zeta_k = \frac{4gJ\rho_0}{\hbar^2\omega_k^2}$ for $k > 0$ we obtain the form

$$\hat{H}_J = \sum_{k=1}^{\infty} \frac{\hbar\omega_k}{2} [\delta\hat{\varrho}_k^2 + (1 + \zeta_k)\hat{\varphi}_k^2] + \frac{g}{2}\delta\hat{\varrho}_0^2 + \hbar J\rho_0\hat{\varphi}_0^2. \quad (\text{C47})$$

Thus, the $k = 0$ eigenmode of \hat{H}_J has the eigenfrequency $\omega_{k=0} = \hbar\sqrt{gJ\rho_0}$ and is not a zero-mode when $J \neq 0$. We also see that there is additionally a squeezing interaction which decays for $k \rightarrow \infty$. Fig. 10 shows plots of merging for different values of J when assuming that the phase-locking term acts homogeneously in space. Fig. 11 show merging obtained by artificially removing the zero-mode, in order to highlight its contribution to the excitations present during the merging.

b. Justification of the phase-locking model

Finally we provide a justification for the phenomenological model above. The argument will be based on the theoretical observation from Ref. [29] that a potential barrier is effectively transparent for low-frequency excitations. This hints that we can phase-lock systems in order to reduce the impact of excitations coming from zero-mode coupling and once this is done one can reduce the barrier further to increase heat transmission.

We consider a quasi-condensate of mean-density ρ_0 in a box of length $2L \gg 2a$ (below we set $L \rightarrow \infty$ for simplicity) with a barrier extending from $z = -a$ to $z = a$ and having a finite height which exceeds the chemical potential by U_B . Moreover, we assume that tunnel coupling between zero modes of the left and right quasi-condensates is negligible. This means that the background density and low-energy excitations feel a hard wall at $z = -a$ for the left quasi-condensate and at $z = a$ for the right quasi-condensate. For concreteness, let us focus on the left quasi-condensate, and it is clear that similar considerations apply also for the right one. The background solution in the bulk (far from the leftmost end) is $\Psi_{0,L}(z) = \sqrt{\rho_0} \tanh[-(z+a)/\xi_h]$, $z < -a$, where $\xi_h = \hbar/(mc)$ is the healing length. Considering the first order in matter field fluctuation $\hat{\Psi}_L = \Psi_{0,L}\hat{1} + \delta\hat{\Psi}_L$ around the full stationary solution the Hamiltonian term corresponding to atom scattering becomes (neglecting a constant term)

$$\hat{V}_L = 2g \int_{-\infty}^{-a} dz |\Psi_{0,L}|^2 \delta\hat{\Psi}_L^\dagger(z) \delta\hat{\Psi}_L(z). \quad (\text{C48})$$

This term, because of the large gradient of $\Psi_{0,L}$ in the two bulks, couples low-energy excitations to high-energy ones. The former can be represented as $\delta\hat{\Psi}_L(z, t) \tanh[-(z+a)/\xi_h]$, where $\delta\hat{\Psi}_L(z, t)$ is subject to Neumann boundary conditions at $z = -a$. The factor $\tanh[-(z+a)/\xi_h]$ follows from considering the adiabatic solution of the time-dependent GPE for excitations with a frequency much less than $g\rho_0/\hbar$ and makes the fluctuation vanishing at the wall. Let us now consider the propagation of high-energy excitations. The high-energy, particle-like excitations propagating from the left ($>$) or from the right ($<$) are parametrized with the following set of orthogonal functions:

$$\psi_k^>(z) \sim \begin{cases} e^{ikz} + i \sin \beta_k e^{i\alpha_k} e^{-ikz}, & z < -a \\ \cos \beta_k e^{i\alpha_k} e^{ikz}, & z > a \end{cases}, \quad \psi_k^<(z) \sim \begin{cases} \cos \beta_k e^{i\alpha_k} e^{-ikz}, & z < -a \\ e^{-ikz} + i \sin \beta_k e^{i\alpha_k} e^{ikz}, & z > a \end{cases}. \quad (\text{C49})$$

Here α_k, β_k parametrize the transmission and reflection amplitudes ($k > 0$) and we also have $\langle \psi_k^\zeta | \psi_{k'}^{\zeta'} \rangle = \delta_{\zeta'\zeta} \delta(k' - k)$, $\zeta', \zeta = >, <$.

We can expect that $\cos \beta_k$ rapidly increases from almost 0 to almost 1, when k approaches $q_B = \sqrt{2mU_B}/\hbar$. We apply a perturbative approach, with the Hamiltonian with hard walls at $z = \pm a$ being the unperturbed Hamiltonian and the Hamiltonian with the barrier of a finite height being the perturbed one. The second-order approximation yields the following term coupling low-energy excitation fields in the left and right quasicondensates:

$$\hat{H}_{LR} = - \int_{-\infty}^{-a} dz \int_a^{\infty} dz' \mathcal{J}(z, z') [\delta\hat{\Psi}_L^\dagger(z) \delta\hat{\Psi}_R(z') + \text{H.c.}], \quad (\text{C50})$$

where the effective coupling coefficient is

$$\mathcal{J}(z, z') = \frac{4(g\rho_0)^2}{U_B} \tanh^3\left(-\frac{z+a}{\xi_h}\right) \tanh^3\left(\frac{z'-a}{\xi_h}\right) \int_{q_B}^{\infty} \frac{dk}{\pi} \frac{q_B^2}{k^2} \{\cos[k(z+z')] + \cos[k(z-z') - \alpha_k - \beta_k]\}. \quad (\text{C51})$$

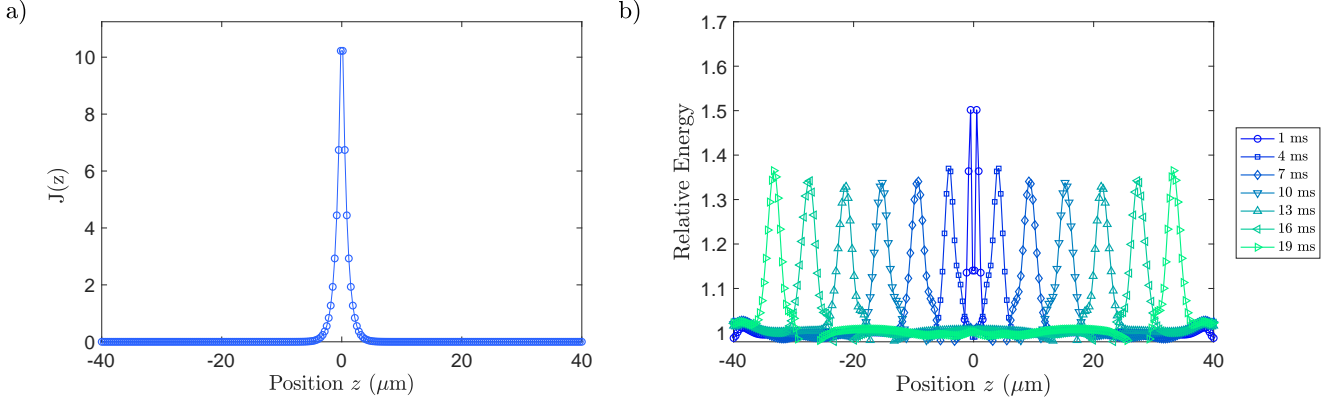


FIG. 12. **The contribution of zero-mode phase diffusion to energy excitations during merging.** Two systems are prepared in thermal, phase-locked states according to the localized coupling J shown in panel (a) with overall strength similar to the value used in the main text $\bar{J} = \frac{1}{L} \int dz J(z) \approx 0.25$ Hz. The magnitude of J at the interface can be tuned in experiments by the barrier parameters. After the preparation phase, J is then quenched to 0, signifying a decoupling of the two systems into independent, gapless Luttinger liquids, where the zero phase mode has no contribution to energy and diffuses according to Eq. (C54) for a total time of 25 ms. When the systems are again merged, as shown in panel (b), we see that large excitations can potentially be induced due to the diffusion of the zero mode. In order to minimize the energy of excitations one should choose a large J in the beginning (meaning a stronger phase-locking during preparation), and design the cycle times to be shorter. The amount of excitations here is an over-estimate as we did not include in the modeling the possibility of phase-locking the condensates before merging, this process could involve strong correlations via the Josephson junction and could counter-act phase diffusion.

In the harmonic approximation, we replace $\delta\hat{\Psi}_R^\dagger \delta\hat{\Psi}_L \approx \frac{1}{2}\rho_0(\hat{\varphi}_L - \hat{\varphi}_R)^2$ (after neglecting density fluctuations [19]) obtaining

$$\hat{H}_{LR} \approx \text{const} + \frac{1}{2} \int_{-\infty}^{-a} dz \int_a^{\infty} dz' \mathcal{J}(z, z') \rho_0(\hat{\varphi}(z) - \hat{\varphi}(z'))^2 \quad (\text{C52})$$

$$\approx \frac{1}{2} \int_{-\infty}^{-a} dz \tilde{\mathcal{J}}(z) \rho_0 \hat{\varphi}(z)^2 + \frac{1}{2} \int_a^{\infty} dz \tilde{\mathcal{J}}(z) \rho_0 \hat{\varphi}(z)^2 - \int_{-\infty}^{-a} dz \int_a^{\infty} dz' \mathcal{J}(z, z') \rho_0 \hat{\varphi}(z) \hat{\varphi}(z'), \quad (\text{C53})$$

that motivates the phenomenological model (C38). Note that in (C38) we further neglect the last interaction term $-\int_{-\infty}^{-a} dz \int_a^{\infty} dz' \mathcal{J}(z, z') \rho_0 \hat{\varphi}(z) \hat{\varphi}(z')$.

c. Phase diffusion after removing the phase-locking interaction

We consider a thermal state with $J \neq 0$ with full support and finite energy penalty on the $k = 0$ eigen-mode (for $J = 0$ it is the phase zero-mode). We thus have $\langle \hat{\varphi}_0^2 \rangle \propto k_B T$ and $\langle \delta \hat{\varphi}_0^2 \rangle \propto k_B T$ similar to the ordinary $k > 0$ modes. We then perform a quench to $J = 0$, which means $\hat{\varphi}_0 \rightarrow \hat{\varphi}_{\text{ZM}}$ and $\delta \hat{\varphi}_0 \rightarrow \delta \hat{\varphi}_{\text{ZM}}$, and observe how the phase zero-mode grows given by the equation

$$\langle \hat{\varphi}_{\text{ZM}}^2(t) \rangle = \langle \hat{\varphi}_0^2 \rangle + \frac{g^2 t^2}{\hbar^2} \langle \delta \hat{\varphi}_0^2 \rangle. \quad (\text{C54})$$

Fig. 12 demonstrates the effect of taking into account zero-mode phase diffusion during the merging process.

4. Sudden merging in the continuous QFT limit and additional checks of the numerical simulation

Let us also briefly discuss here how do our simulations compare with the continuum limit $\Delta z \rightarrow 0$. Essentially, besides the fact that the field operators themselves have the appropriate continuum limit, in the static case we are also interested in recovering the spectrum and the eigenfunctions of the Hamiltonian (2) to some extent. In particular, let us consider two types of density profiles $\rho_0(z)$ that are piece-wise constant functions: (1) two disconnected parts of lengths L_A and L_B on intervals $[-L_A, 0]$ and $(0, L_B]$, where the interface is at $z = 0$, which corresponds to the Hamiltonian $\hat{H}_{A|B}$ and (2) a single system with length $L_{AB} = L_A + L_B$ where the high wall at the interface has been removed, which corresponds to the Hamiltonian \hat{H}_{AB} . We further impose Neumann (open) boundary conditions at all boundary points, i.e., $\partial_z \varphi_k|_{-L_A} = \partial_z \varphi_k|_{-L_A} = \partial_z \varphi_k|_{L_B} = \partial_z \varphi_k|_{L_B} = 0$, and similarly

for the point $z = 0$ in case (1). In such cases, solutions to Eq. (C32) can be easily found on each interval and are given by usual oscillatory functions with a linear dispersion relation

$$\omega_k(L) = \pi ck/L, \quad (\text{C55})$$

where $c = \sqrt{\rho_0 g/m}$ is the speed of sound, k is an integer number and it also depends on the length of the corresponding interval $L \in \{L_A, L_B, L_{AB}\}$. In case (1) we have the two solutions for $k > 0$

$$\delta \varrho_{2k-1}^{A|B}(z) = \varphi_{2k-1}^{A|B}(z) = \begin{cases} \sqrt{\frac{2}{L_A}} \cos(\pi k(z + L_A)/L_A) & \text{for } z \in [-L_A, 0], \\ 0 & \text{for } z \in (0, L_B] \end{cases} \quad (\text{C56})$$

$$\delta \varrho_{2k}^{A|B}(z) = \varphi_{2k}^{A|B}(z) = \begin{cases} 0 & \text{for } z \in [-L_A, 0] \\ \sqrt{\frac{2}{L_B}} \cos(\pi k(z - L_B)/L_B) & \text{for } z \in (0, L_B] \end{cases}, \quad (\text{C57})$$

with corresponding dispersion relations respectively $\omega_{2k-1} = \pi ck/L_A$ and $\omega_{2k} = \pi ck/L_B$. Note that in the case $L_A = L_B$ there is a degeneracy between even and odd modes.

For case (2), instead, we have the solutions

$$\delta \varrho_k^{AB}(z) = \varphi_k^{AB}(z) = \sqrt{\frac{2}{L_{AB}}} \cos(\pi k(z + L_A)/L_{AB}), \quad (\text{C58})$$

with dispersion relation $\omega_k^{AB} = \pi ck/L_{AB}$. The agreement of the dispersion relation and the profile of the eigenmode functions in the static case can be observed in Figs. 13,14 where a comparison with the discretized homogeneous model with or without a trapeze-like buffer region is shown.

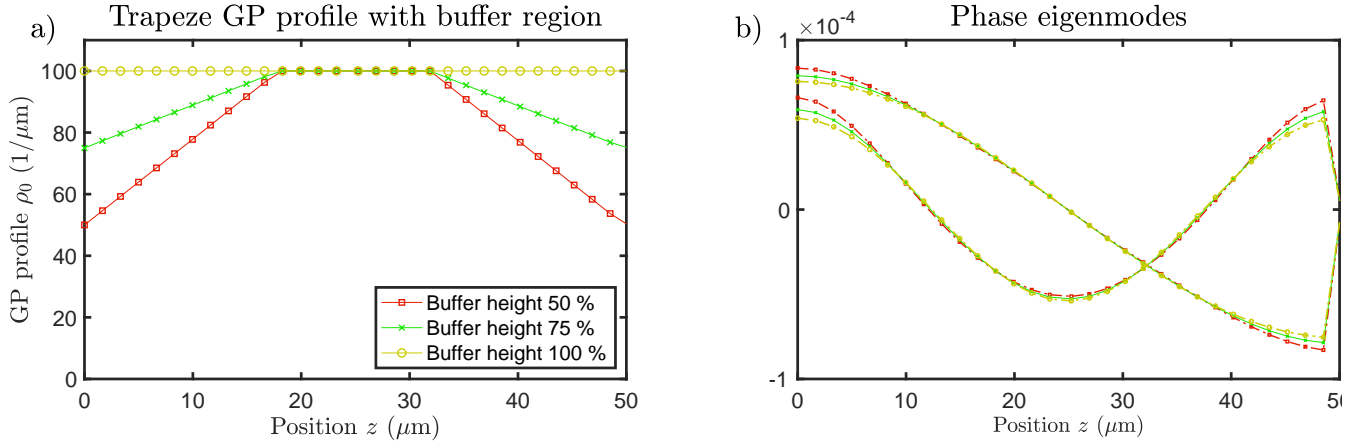


FIG. 13. **Influence of the buffer region on eigenmodes.** (a): Using the lattice discretization various inhomogenous GP profiles can be considered. (b): Phase eigenmodes for $k = 1$ and $k = 2$ of disjoint Hamiltonian $H_{A|B}$. Only the half system with nonzero eigenmode functions is shown as they vanish outside of the support of the GP profile. Qualitatively, all modes retain their oscillatory nature, though at the edges, where the inhomogeneity is the largest, there is a systematic change in the wave-functions.

Afterwards, let us try to compare the dynamics of the merging QTP with its continuous quantum field limit. First of all, we observe that the initial state in the continuous QFT, i.e., the thermal state of the QFT limit of the split Hamiltonian, would have the spectrum of the covariance matrix given by $\langle (\hat{\varphi}_k)^2 + (\delta \hat{\varrho}_k)^2 \rangle = 2\langle \hat{n}_k \rangle + 1$, where $\langle \hat{n}_k \rangle = 1/(\exp(\beta\omega_k) - 1)$ are the normal mode occupation numbers, given by the usual Bose-Einstein distribution. Then, from the fact that for our initial state we have $\langle \hat{a}_k^\dagger \hat{a}_l^\dagger + \hat{a}_k \hat{a}_l \rangle = 0$ and $\langle \hat{a}_k^\dagger \hat{a}_l + \hat{a}_k \hat{a}_l^\dagger \rangle = (2\langle \hat{n}_k \rangle + 1)\delta_{k,l}$, we obtain for the initial real space correlation matrix

$$C_{A-B}(z, z', t = 0) = C^{\rho\rho}(z, z') \oplus C^{\phi\phi}(z, z') = \sum_{k>0} \frac{\hbar\omega_k}{g} \delta \varrho_k(z) \delta \varrho_k(z') (2\langle \hat{n}_k \rangle + 1) \oplus \sum_{k>0} \frac{g}{\hbar\omega_k} \varphi_k(z) \varphi_k(z') (2\langle \hat{n}_k \rangle + 1), \quad (\text{C59})$$

where here and in the following discussion we discard the zero mode, since in the simulations we have regularized it as discussed in Sec.C 3.

Clearly, the result in Eq. (C59) is very similar to the discretized case, but contains small differences in the normal mode

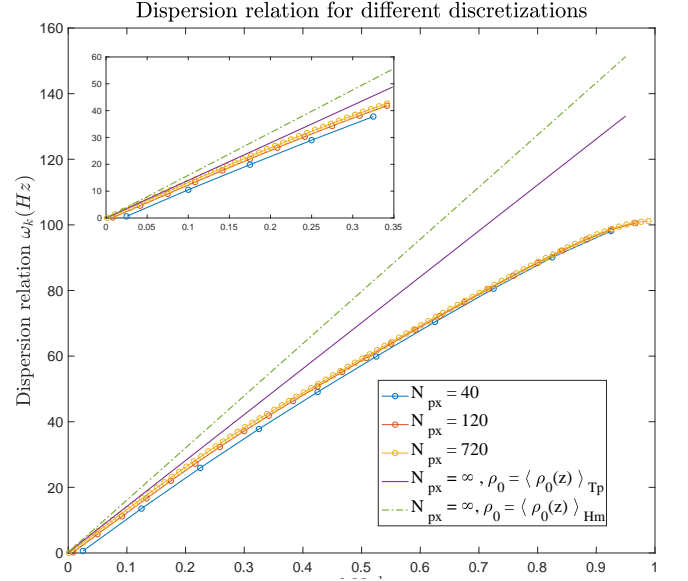
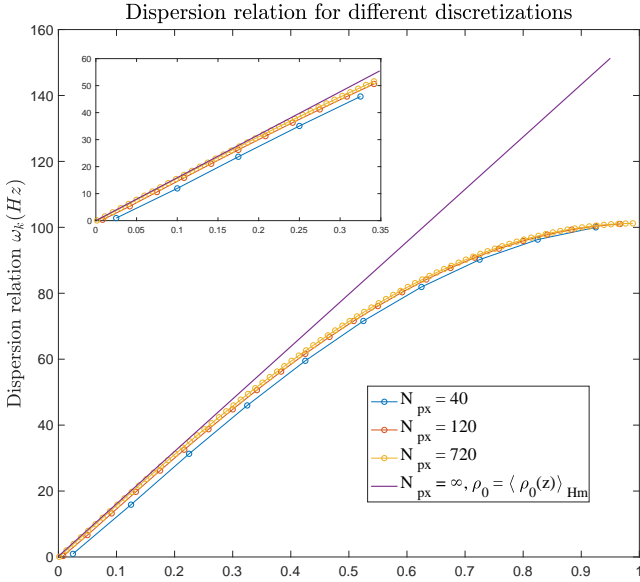
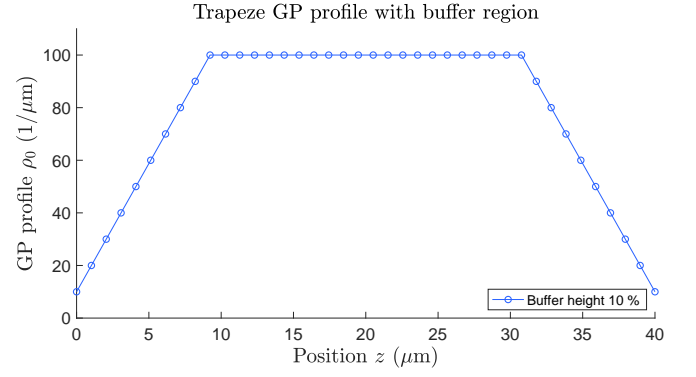
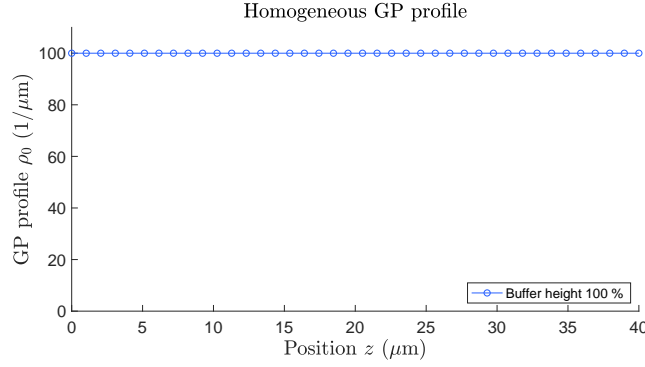


FIG. 14. **Dispersion relations for the homogeneous GP profile.** For a homogeneous profile (*top*) we find that for high momentum modes the dispersion relation is no longer approximately linear due to the lattice discretization. This leads to the dispersion of the wave packets during for example merging. The inset shows that approximately 30% of the low-energy modes already gives rise to a good approximation to the continuum limit, especially for discretizations above the order of ~ 100 pixels, which is the resolution at where our simulations were performed.

FIG. 15. **Dispersion relations for the trapeze GP profile.** When compared to Fig. 14, the dispersion relation for higher modes is closer to a linear curve, especially for high momentum modes. This is why when using such a trapeze GP model when putting condensates in heat contact, we observe wave packets undergoing significantly less dispersion. Since less atoms are considered in this condensate due to the trapeze-shaped profile, the low-lying energy modes are better approximated by the continuum limit assuming a *homogeneous* condensate with GP profile at $\rho_0 = \langle \rho_0(z) \rangle_{Tp} = \text{const.}$

frequencies and in the functional form of the normal modes with respect to the real space modes. For the energy density we thus obtain

$$\frac{dE(z, 0)}{dz} = \frac{\hbar^2 \rho_0(z)}{2m} \partial_{z_1} \partial_{z_2} C_{A-B}^{\phi\phi}(z_1, z_2, t=0) \Big|_{z_1=z_2=z} + \frac{g}{2} C_{A-B}^{\rho\rho}(z, z, t=0) \quad (C60)$$

$$= \hbar \sum_{k>0} \left(\frac{\rho_0}{2m} \frac{g}{\omega_k} (\partial_z \varphi_k(z))^2 + \frac{g}{2} \frac{\omega_k}{g} \delta \varphi_k^2(z) \right) (2\langle \hat{n}_k \rangle + 1) \quad (C61)$$

$$= \begin{cases} \frac{\hbar}{L_A} \sum_{k \text{ odd}} \omega_k (\langle \hat{n}_k \rangle + 1/2) & \text{for } z \in [-L_A, 0) \\ \frac{\hbar}{L_B} \sum_{k \text{ even}} \omega_k (\langle \hat{n}_k \rangle + 1/2) & \text{for } z \in (0, L_B], \end{cases} \quad (C62)$$

where in the first equality we have used $\langle \hat{a}_k^\dagger \hat{a}_l + \hat{a}_k \hat{a}_l^\dagger \rangle = (2\langle \hat{n}_k \rangle + 1)\delta_{k,l}$ and in the second equality we used that

$$\begin{aligned} \frac{\rho_0}{2m} \frac{g}{\omega_k} (\partial_z \varphi_k(z))^2 + \frac{g}{2} \frac{\omega_k}{g} \delta \varrho_k^2(z) &= \frac{1}{L_A} \frac{\omega_k}{2} & \text{for } k \text{ odd,} \\ \frac{\rho_0}{2m} \frac{g}{\omega_k} (\partial_z \varphi_k(z))^2 + \frac{g}{2} \frac{\omega_k}{g} \delta \varrho_k^2(z) &= \frac{1}{L_B} \frac{\omega_k}{2} & \text{for } k \text{ even} \end{aligned} \quad (\text{C63})$$

for all z respectively in $[-L_A, 0)$ and $(0, L_B]$, and we have that the functions are zero otherwise. Let us now consider the time-dependent interaction. The energy density at time $t > 0$ during this evolution is calculated as

$$\frac{dE(z, t)}{dz} = \frac{\hbar^2 \rho_0(z)}{2m} \partial_{z_1} \partial_{z_2} C_{A-B}^{\phi\phi}(z_1, z_2, t) \Big|_{z_1=z_2=z} + \frac{g}{2} C_{A-B}^{\rho\rho}(z, z, t), \quad (\text{C64})$$

where now we need the diagonal blocks of the correlation matrix at time t , namely $C_{A-B}^{\phi\phi}(z, z', t) = \langle \hat{\varphi}(z, t) \hat{\varphi}(z', t) \rangle$ and $C_{A-B}^{\rho\rho}(z, z', t) = \langle \delta \hat{\varrho}(z, t) \delta \hat{\varrho}(z', t) \rangle$, which, in turn, can be calculated from the instantaneous eigenmode functions at time t , that are given essentially by solving Eq. (C32), but now with different boundary conditions at the interface point $z = 0$. See Figs. 7,8 for a plot of the lowest lying eigenmode functions in the discretized model.

Specifically, given the eigenmode functions $\varphi_k^{(t)}(z)$ and $\delta \varrho_k^{(t)}(z)$ of the Hamiltonian at time t , together with the corresponding eigenmode frequencies $\omega_k^{(t)}$, we can find the time-evolved field operators at time t as

$$\hat{\varphi}(z, t) = -i \sum_k \sqrt{\frac{g}{\hbar \omega_k^{(t)}}} \varphi_k^{(t)}(z) \left(e^{i\omega_k^{(t)} t} \hat{t}_k^\dagger - e^{-i\omega_k^{(t)} t} \hat{t}_k \right), \quad (\text{C65})$$

where \hat{t}_k and \hat{t}_k^\dagger are the instantaneous creation/annihilation, obtained with a (real) Bogoliubov transformation

$$\hat{t}_k = \sum_l u_{k,l} \hat{a}_l + v_{k,l} \hat{a}_l^\dagger, \quad (\text{C66})$$

from those at $t = 0$. The Bogoliubov coefficients are obtained by imposing that the operators $\hat{\varphi}(z, t = 0)$ and $\delta \hat{\varrho}(z, t = 0)$ coincide with the initial ones, i.e.,

$$-i \sum_k \sqrt{\frac{g}{\hbar \omega_k^{(t)}}} \varphi_k^{(t)}(z) \sum_l (u_{k,l} - v_{k,l}) (\hat{a}_l^\dagger - \hat{a}_l) = -i \sum_k \sqrt{\frac{g}{\hbar \omega_k^{(0)}}} \varphi_k^{(0)}(z) (\hat{a}_k^\dagger - \hat{a}_k), \quad (\text{C67})$$

and can be extracted from the scalar products between the initial and the instantaneous eigenmode functions:

$$u_{k,l} - v_{k,l} = \sqrt{\frac{\omega_k^{(t)}}{\omega_l^{(0)}}} \langle \varphi_l^{(0)}(z), \varphi_k^{(t)}(z) \rangle \quad u_{k,l} + v_{k,l} = \sqrt{\frac{\omega_l^{(0)}}{\omega_k^{(t)}}} \langle \delta \varrho_l^{(0)}(z), \delta \varrho_k^{(t)}(z) \rangle, \quad (\text{C68})$$

where the relation on the right comes from a similar condition on the $\delta \varrho_k$ eigenfunctions. Thus, substituting all of the above relations, the evolved correlation matrices can be obtained through the formulas

$$\begin{aligned} C_{A-B}^{\phi\phi}(z, z', t) &= \sum_{k,l,r} (2\langle \hat{n}_k \rangle + 1) \frac{g}{\hbar \sqrt{\omega_l^{(t)} \omega_r^{(t)}}} \varphi_l^{(t)}(z) \varphi_r^{(t)}(z') 2 \left((u_{l,k} u_{r,k} + v_{l,k} v_{r,k}) \cos \left((\omega_r^{(t)} - \omega_l^{(t)}) t \right) \right. \\ &\quad \left. - (u_{l,k} v_{r,k} + v_{l,k} u_{r,k}) \cos \left((\omega_r^{(t)} + \omega_l^{(t)}) t \right) \right), \\ C_{A-B}^{\rho\rho}(z, z', t) &= \sum_{k,l,r} (2\langle \hat{n}_k \rangle + 1) \frac{\hbar \sqrt{\omega_l^{(t)} \omega_r^{(t)}}}{g} \delta \varrho_l^{(t)}(z) \delta \varrho_r^{(t)}(z') 2 \left((u_{l,k} u_{r,k} + v_{l,k} v_{r,k}) \cos \left((\omega_r^{(t)} - \omega_l^{(t)}) t \right) \right. \\ &\quad \left. + (u_{l,k} v_{r,k} + v_{l,k} u_{r,k}) \cos \left((\omega_r^{(t)} + \omega_l^{(t)}) t \right) \right), \end{aligned} \quad (\text{C69})$$

and finally we obtain the expression for the energy density by plugging all of this into Eq. (C64)

$$\begin{aligned} \frac{dE(z, t)}{dz} = \hbar \sum_{k, l, r} (\langle \hat{n}_k \rangle + \frac{1}{2}) & \left[S_{l, r}^{(t)}(z) \left(u_{l, k} u_{r, k} + v_{l, k} v_{r, k} \right) \cos \left((\omega_r^{(t)} - \omega_l^{(t)}) t \right) \right. \\ & \left. + D_{l, r}^{(t)}(z) \left(u_{l, k} v_{r, k} + v_{l, k} u_{r, k} \right) \cos \left((\omega_r^{(t)} + \omega_l^{(t)}) t \right) \right], \end{aligned} \quad (C70)$$

where, to shorten the notation, we have defined the quantities

$$\begin{aligned} S_{l, r}^{(t)}(z) &:= \left(\frac{\rho_0(z)g}{m\sqrt{\omega_l^{(t)}\omega_r^{(t)}}} (\partial_z \varphi_l^{(t)}(z)) (\partial_z \varphi_r^{(t)}(z)) + \sqrt{\omega_l^{(t)}\omega_r^{(t)}} \delta \varrho_l^{(t)}(z) \delta \varrho_r^{(t)}(z) \right), \\ D_{l, r}^{(t)}(z) &:= \left(\sqrt{\omega_l^{(t)}\omega_r^{(t)}} \delta \varrho_l^{(t)}(z) \delta \varrho_r^{(t)}(z) - \frac{\rho_0(z)g}{m\sqrt{\omega_l^{(t)}\omega_r^{(t)}}} (\partial_z \varphi_l^{(t)}(z)) (\partial_z \varphi_r^{(t)}(z)) \right), \end{aligned} \quad (C71)$$

that depend only on the instantaneous eigenfunctions and eigenfrequencies. Hence, to calculate the energy density at time t we just need the additional calculation of the Bogoliubov coefficients.

As an illustrative example, let us now consider the case $L_A = L_B = L$ and in which we quench directly to the full \hat{H}_{AB} at $t = 0$. In such case we have that the eigenmode functions at $t = 0^+$ are given by (C58) with $L_{AB} = 2L$ and the corresponding eigenfrequencies are $\omega_k^{(+)} = \pi c k / 2L$ with the same sound velocity c , which are just half of the corresponding odd frequencies at $t = 0^-$. Note, however, that at $t = 0^-$ there is a degeneracy, such that the ω_k with odd k have the same values as the even k . Thus, $\omega_k^{(+)}$ coincide with the even eigenfrequencies at $t = 0^-$. The quantities (C71) at time $t = 0^+$ read

$$\begin{aligned} S_{l, r}^{(+)}(z) &= \frac{\pi c}{2L} \sqrt{lr} \sin(\pi(l+r)(z+L)/2L), \\ D_{l, r}^{(+)}(z) &= \frac{\pi c}{2L} \sqrt{lr} \cos(\pi(l+r)(z+L)/2L). \end{aligned} \quad (C72)$$

Furthermore, the Bogoliubov coefficients satisfy

$$\begin{aligned} u_{2k-1, l} &= \frac{1}{2} \frac{\omega_l^{(+)} + \omega_k^{(0)}}{\sqrt{\omega_k^{(0)}\omega_l^{(+)}}}, \quad O_{k, l} = \frac{2k+l}{\sqrt{2kl}}, \quad O_{k, l} = u_{2k, l}, \\ v_{2k-1, l} &= \frac{1}{2} \frac{\omega_l^{(+)} - \omega_k^{(0)}}{\sqrt{\omega_k^{(0)}\omega_l^{(+)}}}, \quad O_{k, l} = \frac{2k-l}{\sqrt{2kl}}, \quad O_{k, l} = v_{2k, l}, \end{aligned} \quad (C73)$$

where

$$O_{k, l} = \frac{\sqrt{2}}{L} \int_0^L dz \cos(\pi k z / L) \cos(\pi l z / 2L) = \frac{\sqrt{2}}{\pi(k+l/2)} \left(\frac{k \sin((k-l/2)\pi)}{k-l/2} + (-1)^k \sin(l\pi/2) \right) \quad (C74)$$

are the scalar products between the eigenfunctions at $t = 0^-$ and $t = 0^+$. Plugging all of this into Eq. (C70) we finally obtain the energy density at time $t > 0$ as

$$\begin{aligned} \frac{dE(z, t)}{dz} = \hbar \sum_{k \text{ even}} \sum_{r, l} (\langle \hat{n}_k \rangle + \frac{1}{2}) & \frac{\pi c}{2kL} \left[(4k^2 + lr) \sin(\pi(l+r)(z+L)/2L) \cos(\pi c t(r-l)/2L) \right. \\ & \left. + (4k^2 - lr) \cos(\pi(l+r)(z+L)/2L) \cos(\pi c t(r+l)/2L) \right], \end{aligned} \quad (C75)$$

and we can see that this expression reflects a superposition of waves traveling at speed of sound c , and, in particular, there is no dispersion.

5. Details of compression and expansion

Here we give a more detailed discussion of the approximations that were involved in formulating the piston model in the maintext. We consider the Lieb-Liniger model for the gas trapped in a box of changing size from $L(0)$ to $L(t)$. After the standard phononic expansion $\hat{\Psi} = \sqrt{\hat{\rho}}e^{i\hat{\theta}}$ in the long wave-length limit the Hamiltonian can be approximated as

$$\hat{H}_{\text{LL}} \approx \int_0^L dz \left[\frac{\hbar^2}{2m} (\partial_z \hat{\theta}) \hat{\rho} (\partial_z \hat{\theta}) + \frac{g}{2} \hat{\rho}^2 \right]. \quad (\text{C76})$$

We next split the operators around the classical hydrodynamical solutions, specifically we introduce the density fluctuations $\hat{\rho} = \rho_0 + \delta\hat{\rho}$ and phase fluctuations $\hat{\theta} = \varphi + \hat{\varphi}$.

The classical phase can be interpreted as the velocity-potential by means of the equation $v = \hbar \partial_z \varphi / m$. In a simple case where only one wall is moving we have that the classical hydrodynamic equations

$$\frac{\partial \rho}{\partial t} + \frac{\partial}{\partial z}(\rho v) = 0, \quad (\text{C77})$$

$$\frac{\partial v}{\partial t} + v \frac{\partial v}{\partial z} = -\frac{g}{m} \frac{\partial \rho}{\partial z}, \quad (\text{C78})$$

have solution given by

$$\rho_0(t) = \frac{N}{L(t)}, \quad v(z, t) = z \frac{\dot{L}(t)}{L(t)}. \quad (\text{C79})$$

In this case we find that the velocity depends on the position and matches the velocity of the moving wall at the boundary, namely that $v(z=0) = 0$ and $v(z=L(t)) = \dot{L}(t)$. This solution is obtained in the long-wavelength limit and neglecting the acceleration of the walls [148]. A similar solution can be obtained also in the case of both walls moving, with Neumann boundary conditions at each wall.

By integrating the velocity we obtain the classical phase field φ which we next use to linearize the Hamiltonian (C76). We thus obtaining the model

$$\hat{H}(t) = \int_0^{L(t)} dz \left[\frac{\hbar^2 \rho_0(z, t)}{2m} (\partial_z \hat{\varphi})^2 + \frac{g}{2} \delta\hat{\rho}^2 + \frac{\hbar \dot{L}(t) z}{2L(t)} [\delta\hat{\rho} (\partial_z \hat{\varphi}) + (\partial_z \hat{\varphi}) \delta\hat{\rho}] \right]. \quad (\text{C80})$$

If the evolution is slow (adiabatic), a lattice model with the fixed number of sites can serve as a good approximation to the discrete-value representation of the continuous system. Thus, in the following we neglect the second cross-coupling term between phases and densities, so to model a quasi-static case where the GP profile gets compressed very slowly. Then, it is also illustrative to observe explicitly how this process works in an infinitesimal step-wise fashion. The infinitesimal length change is

$$L \rightarrow L_\epsilon = (1 + \epsilon)L, \quad (\text{C81})$$

and, correspondingly, a homogeneous GP profile ρ_0 changes to $\rho_0(\epsilon) = (1 + \epsilon)^{-1} \rho_0$. Then, the Hamiltonian after the size change reads

$$\hat{H}_\epsilon = \int_0^{L_\epsilon} dz \left[\frac{\hbar^2 \rho_0}{2m(1 + \epsilon)} (\partial_z \hat{\varphi})^2 + \frac{g}{2} \delta\hat{\rho}^2 \right], \quad (\text{C82})$$

which is Eq. (C80) without the last term. Thus we observe that if a GP profiles changes slowly in length then the phonons are described by a similar Hamiltonian, only with modified couplings.

In the lattice model, we perform a similar procedure, but work fully in real space, this time with the Hamiltonian as a functional of both mean-field density and the small-distance cutoff. Starting from the discretized Hamiltonian $\hat{H}_N[\rho_0, \Delta z]$ of a single condensate with N pixels, length $L = N\Delta z$, and density ρ_0 , we perform at each step a small length change $L \mapsto L_\epsilon = N\Delta\zeta$, corresponding to a renormalization

$$H_N[\rho_0, \Delta z] \mapsto H_N[\rho_0(\epsilon), \Delta\zeta] = H_{\rho\rho}(1 + \epsilon) \oplus H_{\phi\phi}/(1 + \epsilon)^2, \quad (\text{C83})$$

where we have used that $\rho_0(\epsilon) = \rho_0/(1 + \epsilon)$ and $\Delta\zeta = (1 + \epsilon)\Delta z$. Thus, we see that we are implementing a discretized version of the Hamiltonian (C82).

Then, in order to complete the full length change ΔL in a time $t_{\text{comp}} = N_t \Delta t$, where Δt is a small time interval and N_t is

the total number of Trotter steps, at each discrete time step we perform an infinitesimal length change, such that

$$\epsilon = \Delta L / N_t. \quad (\text{C84})$$

What we get is the state of the phonons after compressing by a finite amount. This assumes that the phonons always see a quasi-static background metric, that is their dynamical time-scales are much faster than how we compress the condensate. We observe that a sufficiently slow compression will not mix much between the modes and there will be thermal squeezing of the phonons. We also see that the energy will in fact change. This is expected, since we are performing work on the system by compressing it which means it should increase in energy. The compression protocol is therefore our main way to realize a piston, where one may actively perform/extract work on a condensate by changing its length, and therefore its energy density and effective temperature.

a. Renormalizing the cutoff during compression QTP

Let us now discuss a technical detail arising in the compression/expansion QTP. An implicit difference between the initial and final Hamiltonians of a compression/expansion step is that the continuous field theory should be defined in the time-dependent line $[0, L(t)]$. In principle, we can also make a change of the integration variable $z \mapsto \zeta = zL(0)/L(t)$, such that the theory is defined with a constant length. However, a subtle issue arises: the field commutation relations $[\delta\hat{\varphi}(z), \hat{\varphi}(z')] = i\delta(z - z')$ depend on the coordinate z ; thus a rescaling of the coordinate must be compensated by a corresponding rescaling of the density fluctuation field, in order to maintain the correct commutation relations. Then, calling $\lambda(t) = L(0)/L(t)$ we define the transformation

$$\begin{aligned} \zeta &= \lambda(t)z, \\ \delta\hat{\nu} &= \delta\hat{\varphi}/\lambda(t), \end{aligned} \quad (\text{C85})$$

such that the Hamiltonian (C80) becomes

$$\hat{H} = \int_0^{L(0)} d\zeta \left[\frac{\hbar^2 \rho_0(z, 0) \lambda^2(t)}{2m} (\partial_\zeta \hat{\varphi})^2 + \frac{g}{2} \lambda(t) \delta\hat{\nu}^2 \right], \quad (\text{C86})$$

which effectively amounts to a renormalization of the line differential as

$$dz \mapsto d\zeta = \lambda(t)dz, \quad (\text{C87})$$

at the same time ensuring that the fields satisfy the correct commutation relations:

$$[\delta\hat{\varphi}(\zeta), \hat{\varphi}(\zeta')] = i\delta(\zeta - \zeta')/\lambda(t) \Rightarrow [\delta\hat{\nu}(\zeta), \hat{\varphi}(\zeta')] = i\delta(\zeta - \zeta'). \quad (\text{C88})$$

Note that by making this field transformation, the full Hamiltonian (C80) is transformed in such a way that the time derivatives of its parameters disappear. Therefore, the Hamiltonian (C86) can be approximated by a lattice model without restrictions on the rate of change of parameters, i.e., no assumption about adiabaticity is required anymore. However, one has still to be careful with defining correctly the new rescaled density-fluctuation field in the discretized model.

A similar issue arises also working directly in the discretized version of (C82): By fixing the number of pixels and just rescale the cut-off Δz at each Trotter step we are changing its effective momentum cut-off. Concretely, if we keep the number of pixels we see that the discretization length $\Delta\zeta$ has changed according to

$$\Delta\zeta = \frac{L_\epsilon}{L} \Delta z. \quad (\text{C89})$$

It is important to stress once more that the covariance matrices satisfy the Heisenberg constraint that depends on Δz . Thus, we begin with a covariance matrix Γ that satisfies

$$\Gamma + \frac{1}{\Delta z} i\Omega \geq 0, \quad (\text{C90})$$

but after size change it should satisfy

$$\Gamma + \frac{1}{\Delta\zeta} i\Omega \geq 0. \quad (\text{C91})$$

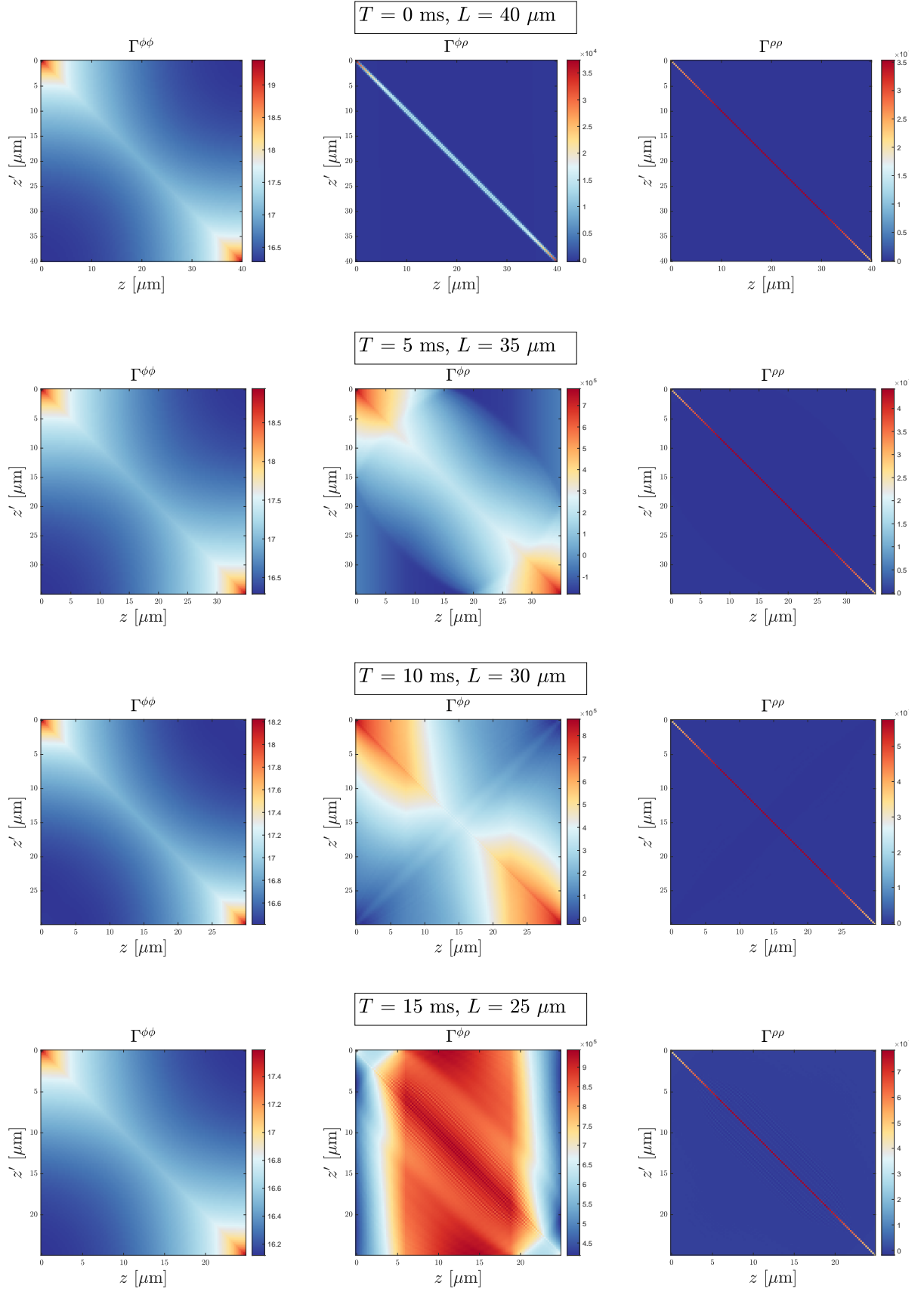


FIG. 16. Covariance matrix of the piston while being compressed over a period of 20 ms from $L(0) = 40 \text{ } \mu\text{m}$ to $L(t_{\text{comp}}) = 20 \text{ } \mu\text{m}$. The squeezing of eigenmodes can be also seen in real space as shown here: One finds that the overall magnitude of phase fluctuations decreases while for the density fluctuations it increases. The cross correlations do not contribute to the energy of the piston but their presence signifies that the system is not thermal during compression.

However, the natural way to implement the compression is, as we discussed above, to apply a symplectic transformation $G(\epsilon) = \exp(\Omega H_\epsilon / \Delta\zeta)$ that preserves the symplectic form and hence does not allow to switch between the Heisenberg cones with $\Delta z \mapsto \Delta\zeta$. The way to implement the latter switch is to multiply the condition of the second cone and find that

$$\Gamma + \frac{1}{\Delta z} i\Omega \geq 0 \Leftrightarrow \frac{\Delta z}{\Delta\zeta} \Gamma + \frac{1}{\Delta\zeta} i\Omega \geq 0. \quad (\text{C92})$$

Hence we can now do the compression by setting

$$\Gamma(t_{\text{comp}}) = \frac{\Delta z}{\Delta\zeta} G(t_{\text{comp}}) \Gamma(0) G^T(t_{\text{comp}}) \quad (\text{C93})$$

where $G(t_{\text{comp}})$ implements the Trotterized evolution from Eq. (C83). This covariance matrix will satisfy the Heisenberg relation at the target discretization length. This is not anymore just a symplectic transformation, but an affinely symplectic transformation which preserves the symplectic form up to an overall pre-factor.

6. Achieving larger cooling in the Otto cycle

In the main text, we have shown how to concatenate the QTPs introduced, in order to operate a refrigerator to cool down part of the system. The remaining question is then how can we optimize the transfer of energy from the system to the bath (via piston), by tuning the various parameters that we have, such as t_{merge} , t_{split} , t_{comp} , $L_{P(B,S)}$ etc. We discuss the effects and therefore the strategy of choice for some of the parameters below:

1. **Initial lengths (and length ratios) of system, piston and bath.** The lengths of each machine compartment determines their heat capacity. For example, a larger piston would be able to absorb (or lose) more heat when interacting with the system (bath). The size of the bath would largely determine how strong the non-Markovian effects are, especially since wave-packets are traveling ballistically in the condensate. For example, in our simulations the bath is only 3 times larger, which is a realistic figure when considering implementations. According to Fig. 6, the wave-packets induced in the bath at the piston-bath interface has already travelled to the other bath edge and returned to the interface during the second cycle of piston-bath interaction, effectively making the process non-Markovian. In Fig. 17, we see a simulation where one effectively simulates a Markovian bath (and piston) by reinitializing them before every new cycle.
2. **Compression ratio of piston.** It is clear that the more compression the piston undergoes, the more work is injected into the refrigerator. This causes a larger effective temperature difference between piston and bath, thereby inducing a larger amount of heat flow between them, which in turn increases the capability of the piston to later absorb heat while interacting with the system. While in classical scenarios the piston stays in equilibrium while gradually increasing in temperature, our model of compression as discussed in Section II is akin to squeezing, and therefore the higher the amount of compression, the further we expect the system goes out of equilibrium, which is seen in our simulations.
3. **Compression ratio of bath and system.** In the protocol we presented, for simplicity, the bath and system never undergo any change in length. However, if we imagine the three condensates on a chip, whenever we compress the piston, this leaves additional room for the bath to expand. Such an additional step, if undertaken, will further increase the temperature gradient and therefore facilitate heat flow.
4. **Total duration when merging and splitting two systems.** Suppose two systems are connected and heat flow occurs due to an effective temperature gradient. How would one design the protocol to allow a maximum amount of net heat flow? Naturally, one expects that in the long time limit, energy will be equally distributed throughout the joint system, i.e. they thermalize. However, we are interested mostly in finite time scales. Therefore, in practice, the most relevant parameters to set are the timings of merging, with respect to the lengths of the interacting systems. Moreover, the energy input during merging is non-negligible due to the relatively small sizes of each system. To overcome this, for example, one could time the protocol so that when we split the condensates again at the end, the wave-packets come back to the interface and then are taken out of the system due to the change in Hamiltonian. This can be done because we know the speed of sound in the condensate, concretely, it becomes natural to set $t_p = L_p/c$, where t_p is a relevant time scale of the piston process. This illustrates the role of information in such a process: although a lot of energy may be injected during merging, the information about this energy is preserved, and therefore it can be suitably retrieved (instead of being irreversibly lost into other degrees of freedom).
5. **Further refinements when considering the GP profile of condensates.** We have seen this in the case of putting two systems into heat contact. When a single condensate sits in the trap, the bulk region has a roughly uniform density, which is why one usually considers the fairly good approximation of a homogeneous ρ_0 . The situation becomes more complicated when two such systems are merged: ideally, we want the contact interface to have large atom density as well, so that heat

transport is maximized. However, we saw from the simulations that this induced extremely high momentum modes which may cause us to observe more dispersion, and furthermore the Luttinger liquid analysis may no longer be useful in such regimes. On the other hand, having a small contact interface such as shown in the trapeze profile would imply that heat flow occurs more slowly in finite time scales.

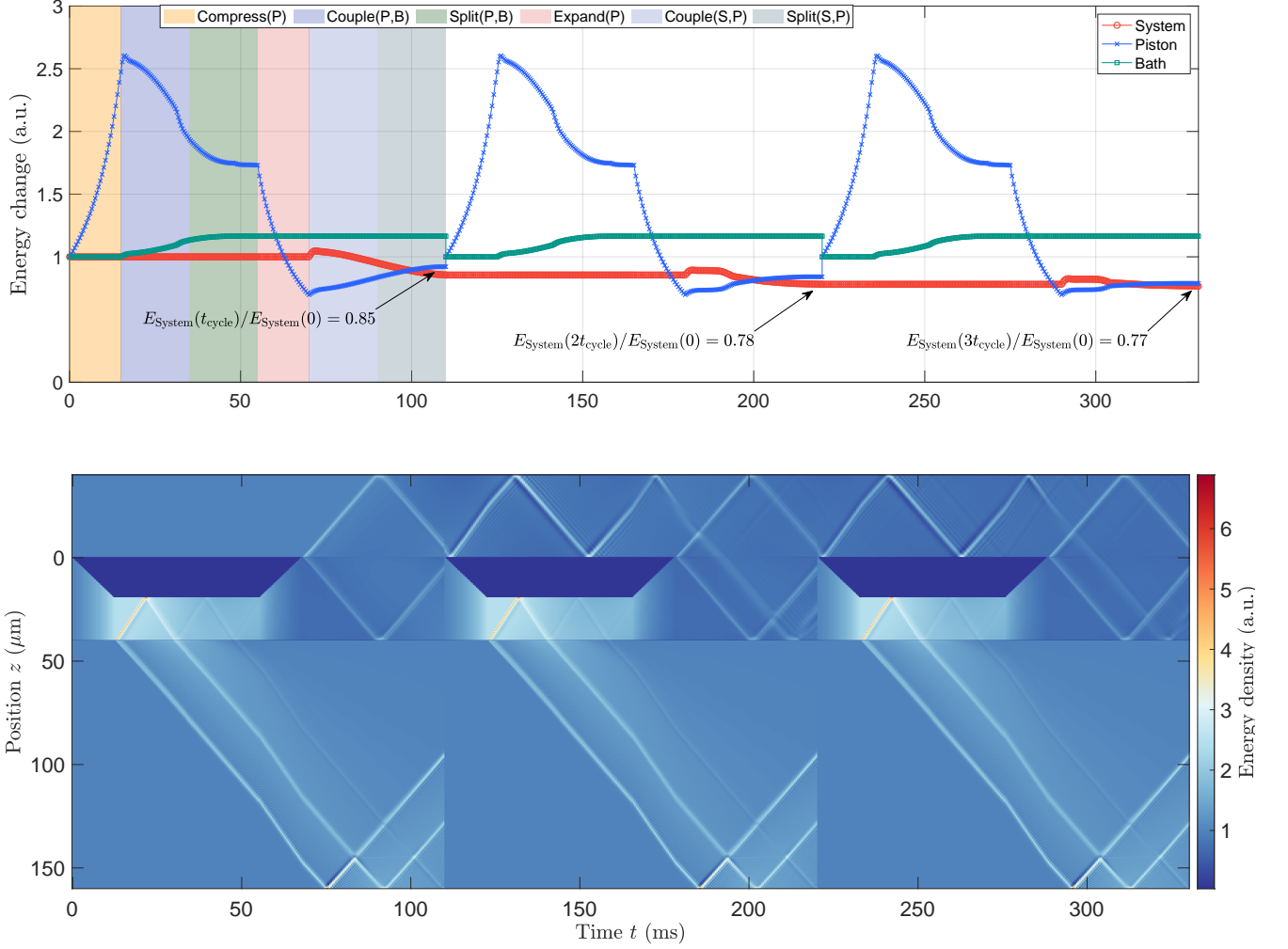


FIG. 17. Here we show the Otto cycle energy changes of system, piston and bath with a different setting: $t_{\text{couple}} = 20$ ms, $t_{\text{split}} = t_{\text{comp}} = 20$ ms, $L_{\text{piston}} = L_{\text{system}} = 40$ μm , and $L_{\text{bath}} = 120$ μm . On one hand, the GP profile of the condensates at the edge drop off only slightly to about 0.8 of the peak value, which allows for more heat flow to occur between condensates during finite time, with the cost of injecting higher momentum modes into the simulation. On the other hand, after each cycle we reset the piston and the bath to its original state. This reinitialization, while challenging to perform in experiments, allow fresh thermal resources to be brought into the quantum field machine and therefore allows us to achieve more cooling in subsequent cycles. Despite having a similar qualitative behaviour as in Fig. 6, it is evident that the various specific parameters governing each of the primitives will affect the final cooling efficiency of the engine.